Assessment of Propfan Propulsion Systems for Reduced Environmental Impact

by

Andreas Peters

Diplom-Ingenieur, RWTH Aachen University (2007)

Submitted to the Department of Aeronautics and Astronautics
in partial fulfillment of the requirements for the degree of

Master of Science in Aeronautics and Astronautics

at the

MASSACHUSETTS INSTITUTE OF TECHNOLOGY

January 2010

Author .....
Department of Aeronautics and Astronautics
January 29, 2010

Certified by .....
Zoltán S. Spakovszky
H. N. Slater Associate Professor
Thesis Supervisor

Accepted by .....
Eytan H. Modiano
Associate Professor of Aeronautics and Astronautics
Chair, Committee on Graduate Students

Assessment of Propfan Propulsion Systems for Reduced Environmental Impact

by

Andreas Peters

Submitted to the Department of Aeronautics and Astronautics
on January 29, 2010, in partial fulfillment of the requirements for the degree of
Master of Science in Aeronautics and Astronautics

Abstract

Current aircraft engine designs tend towards higher bypass ratio, low-speed fan designs for improved fuel burn, reduced emissions and noise. Alternative propulsion concepts include counter-rotating propfans (CRPs) which have been investigated intensively in the 1970s and 1980s and demonstrated significant reductions in fuel burn. Currently, propfans are being studied again due to their inherent noise challenge and the potential for reduced environmental impact. A newly developed, integrated noise and performance assessment methodology for advanced propfan powered aircraft configurations is introduced. The approach is based on first principles and combines a coupled aircraft and propulsion system performance analysis with 3-D unsteady, full-wheel CRP CFD computations and aero-acoustic simulations. Special emphasis is put on computing CRP interaction tones. The method is capable of dealing with parametric studies and exploring noise reduction technologies.

An aircraft performance and mission analysis was first conducted on a candidate CRP powered configuration. In addition, a comparable aircraft with advanced turbofan engines was defined for performance and noise comparisons. Guided by data available in the literature, a detailed aerodynamic design of a pusher CRP was carried out using vortex-lattice methods and 3-D steady RANS computations of the counter-rotating stage. Full-wheel unsteady 3-D RANS simulations were then used to determine the time varying blade surface pressures and unsteady flow features necessary to define the acoustic source terms. A frequency domain approach based on Goldstein's formulation of the acoustic analogy for moving media and Hanson's single rotor noise method was extended to counter-rotating configurations. The far field noise predictions were compared to experimental data and demonstrated good agreement between the computed and measured interaction tones. The underlying noise source mechanisms due to front-rotor wake interaction, aft-rotor upstream influence, hub-endwall secondary flows and front-rotor tip-vortices were dissected and quantified. Based on this investigation, the CRP was re-designed for reduced noise incorporating a clipped rear-rotor and an increased rotor-rotor spacing to reduce upstream influence, tip-vortex, and wake interaction effects. Maintaining the thrust and propulsive efficiency at takeoff conditions, the noise was calculated for both designs. At the interaction tone frequencies, the re-designed CRP exhibited an average reduction of 7.25 dB in mean SPL computed over the forward and aft polar angle arcs. On the engine/aircraft system level, the re-designed CRP demonstrated a reduction of 9.2 EPNdB and 8.6 EPNdB at the FAR 36 flyover and sideline observer locations, respectively. The results suggest that advanced open rotor designs can possibly meet Stage 4 noise requirements.

Thesis Supervisor: Zoltán S. Spakovszky
Title: H. N. Slater Associate Professor

Acknowledgments

First and most importantly, I would like to thank my advisor Professor Zoltán Spakovszky for giving me the opportunity to join the MIT Gas Turbine Laboratory. I am very grateful for his guidance, encouragement, and invaluable advice throughout my graduate studies at MIT and for making this project a great learning experience.

This thesis was made possible and supported by Pratt & Whitney under the supervision of Dr. Jayant Sabnis. At Pratt & Whitney, I wish to first thank Dr. Sabnis, Dr. Bruce Morin and Dr. Wes Lord for their support, insight, and the many very helpful discussions. The help of Robert Bengtson and Naushir Bala in aircraft and engine cycle assessment are gratefully acknowledged. At United Technologies Research Center, I am most thankful to Dr. Dan Shannon for his input and helpful feedback on the CRP acoustic assessment.

At MIT, I am greatly indebted to Professor Mark Drela for his help with the baseline CRP design and his patience in answering my questions about his vortex lattice codes RVL and RAXAN. At Numeca USA, I would like to thank Róque Lopez and Dr. Alain Demeulenaere for their patient assistance with FINE/Turbo.

I am most thankful to my fellow graduate student Andrew March for his help with low-speed aircraft performance calculations. A special thanks to my labmate Jeff Defoe for his extraordinary efforts in solving network and computer problems. In addition, I could always count on Jeff when I had questions about acoustics. I am particularly thankful to my officemate Jon Everitt for the frequent discussions about the subtleties of working with FINE/Turbo. I am greatly indebted to Björn, David, François, and Ryan in the "glass office" for their encouragement at all times. I would also like to thank Alex, Georg, George, Leo, Shinji, Sho, Stevan, and Tanya for their friendship and for making the GTL a great place to work.

Finally, I wish to thank my parents for their love, support, and advice throughout my education. All my love goes to Anneli. MIT would have been far more challenging without her continuous encouragement and understanding.

Contents

List of Figures

List of Tables

Nomenclature

Abbreviations

CFD	Computational Fluid Dynamics
CRP	Counter-Rotating Propfan
CRPNEC	Counter-Rotating Propfan Noise Estimation Code
EDET	Empirical Drag Estimation Technique
EPNL	Effective Perceived Noise Level (EPNdB)
ESDU	IHS ESDU Engineering Service
FAA	Federal Aviation Administration
FAR	Federal Aviation Regulations
FINE/Turbo	Flow INtegrated Environment for Turbomachinery Flows
FLOPS	Flight Optimization System
GasTurb	Gas Turbine Performance Simulation Software
HPT	High Pressure Turbine
ICAC	Initial Cruise Altitude Capability
ICAO	International Civil Aviation Organization
ISA	International Standard Atmosphere
LPC	Low-Pressure Compressor
LPT	Low-Pressure Turbine
MFW	Maximum Fuel Weight
MEW	Manufacturer's Empty Weight
MLW	Maximum Landing Weight
MTOW	Maximum Takeoff Weight

MTOGW	Maximum Takeoff Gross Weight
MZFW	Maximum Zero Fuel Weight
NASA	National Aeronautics and Space Administration
NLH	Non-Linear Harmonic Method
OASPL	OverAll Sound Pressure Level
OEW	Operating Empty Weight
PNLT	Tone-Corrected Perceived Noise Level (dB)
RANS	Reynolds Average Navier-Stokes
RAXAN	Rotor AXisymmetric ANalysis
ROC	Rate of Climb
RVL	Rotor Vortex Lattice
SAE	Society of Automotive Engineers
SFC	Specific Fuel Consumption
SL	Sea Level
SPL	Sound Pressure Level
SRP	Single-Rotating Propfan

Roman Symbols

A	blade area (m^2)
A	number of angular positions per revolution (-)
B	blade count (-)
BPF	blade passing frequency (Hz)
c	speed of sound (m/s)
c	blade chord (m)
c_l	sectional lift coefficient (-)
c_p	specific heat at constant pressure (J/kg)
C_D	drag coefficient (-)
C_L	lift coefficient (-)

C_P	power coefficient (-)
C_T	thrust coefficient (-)
D	diameter (m)
f	frequency (Hz)
F_i	force per unit area on blade surface normalized by ambient pressure (-)
$F_{i,\mu,\nu}$	discrete loading element in coordinate direction i, normalized by r_{tip}^2 (-)
h	altitude (m,ft)
h	enthalpy (J/kgK)
J	advance ratio (-)
k	loading harmonic order (-)
k_m	wavenumber (-)
m, n	harmonic of blade passing frequency (-)
$\dot{m}$	mass flow (kg/s)
M	Mach number (-)
M_N	Mach number normal to blade surface (-)
M_{tip}	tip Mach number (-)
N	rotational speed (1/s)
p	static pressure (Pa)
p'	acoustic pressure disturbance (Pa)
p_L	acoustic pressure disturbance due to dipole sources (Pa)
p_t	stagnation pressure (Pa)
p_T	acoustic pressure disturbance due to monopole sources (Pa)
P	power (W)
P_{Lm}	loading noise at harmonic m normalized by ambient pressure (-)
P_{Tm}	thickness noise at harmonic m normalized by ambient pressure (-)
Q	torque (Nm)
r	radius (m)
r_{hub}	hub radius (m)
r_{tip}	tip radius (m)
S	amplitude radius normalized by blade tip radius (-)

SF	scaling factor (-)
Δt_{output}	time step at which unsteady pressure data is recorded in CFD simulations (s)
t	time (s)
T	static temperature (K)
T	thrust (N)
T	time limit for acoustic analogy integrals (s)
T	period of rotor revolution (s)
T_t	stagnation temperature (K)
V_N	velocity normal to blade surface (m/s)
V_tip	rotor tip speed (m/s)
V_x	axial velocity (m/s)
$V_{\mu,\nu}$	discrete form of thickness source term, normalized by r_{tip}^2 (-)
V_θ	tangential velocity (m/s)
$\mathbf{x}$	observer coordinates, x, y, z, normalized by blade tip radius (-)
x/D_1	rotor-rotor axial spacing (-)
$\mathbf{y}$	source coordinates, x_0, y_0, z_0, normalized by blade tip radius (-)

Greek Symbols

β	blade angle setting at 75 % span, measured from tangential direction (°)
η_{ad}	adiabatic efficiency (-)
η_{prop}	propulsive efficiency (-)
φ	sweep (°)
ϕ_S	tangential source coordinate (rad)
ϕ_{ref}	blade position reference angle (rad)
ϕ_0	tangential blade element coordinate in source integration (rad)
γ	specific heat ratio (-)
π	stagnation pressure ratio (-)
θ	polar directivity angle (°)

Θ	torque split (-)
ρ	density (kg/m^3)
σ	phase radius normalized by blade tip radius (-)
τ	stagnation temperature ratio (-)
ω	angular velocity (rad/s)
Ψ	stage loading (-)

Subscripts

a	location upstream of front rotor in baseline CRP design
b	location between front and rear rotors in baseline CRP design
c	location downstream of rear rotor in baseline CRP design
e	exit condition in baseline CRP design control volume analysis
$cruise$	cruise operating condition
CRP	CRP engine
fan	turbofan engine
FS	full scale
LP	engine core component on low-pressure spool
max	maximum quantity
min	minimum quantity
MS	model scale
$steady$	steady quantity
TO	takeoff operating condition
0	free stream quantity
1	front rotor
2	rear rotor
μ	index for counting source elements in radial direction
ν	index for counting source elements in chordwise direction

Chapter 1

Introduction

1.1 Background and Previous Work

Advanced open rotor designs have the potential to extend the inherent fuel efficiency benefits of conventional turboprop engines to flight Mach numbers of up to 0.8. By recovering the residual swirl downstream of the front rotor, counter-rotating propfan (CRP) concepts can provide an increase of $6-8\%$ in propulsive efficiency compared to single rotor configurations [3] [4]. CRPs have been investigated intensively in the 1970s and 1980s. Two examples of full scale CRPs flight tested in the late 1980s are shown in Figure 1-1. The GE Unducted Fan (UDF) featured two 8-bladed rotors, 11.7 ft in diameter. The PW/HS/Alliston 578-DX had two 11.6 ft diameter 6-bladed rotors. Both model and full scale studies demonstrated significant reductions in fuel burn of up to 30% compared to high bypass engines of 1980 vintage which are currently deployed on most civil aircraft [5].

Currently, propfans are being extensively studied again due to their potential for reduced environmental impact and their inherent noise challenge. However, in the light of future design trends and noise regulations, the aerodynamic and acoustic competitiveness of prospective CRP designs needs to be evaluated relative to performance levels attained by advanced turbofan configurations. Thus, a credible advanced turbofan needs to be defined to establish a basis for comparison.

In order to explore the fuel burn benefits and acoustic performance of CRP air-

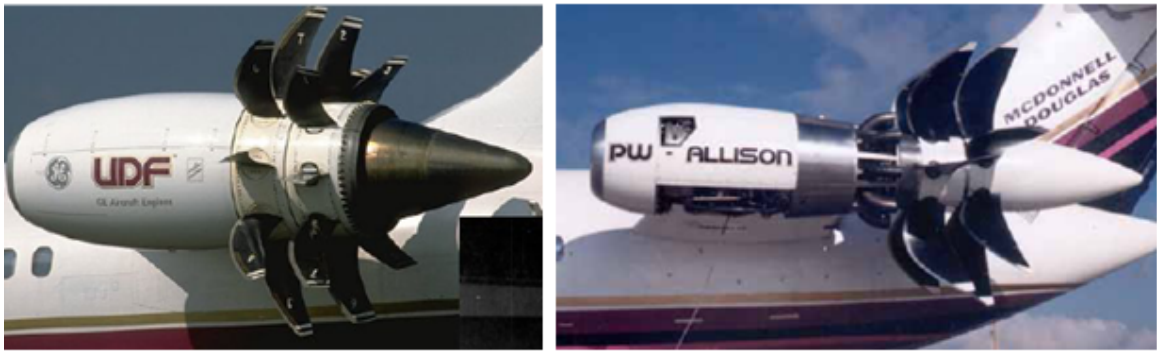

Figure 1-1: GE UDF flight test on MD-80 in 1988 (left) and PW/HS/Allison 578-DX flight test on MD-80 in 1989 (right)

craft configurations, an integrated noise and performance assessment methodology is required and developed in this thesis. Existing methods are used for aircraft mission and engine cycle analysis, noise prediction of engine core and airframe sources, and for the aerodynamic propfan design and performance assessment. A new approach to estimate CRP noise is developed based on Hanson's single rotor noise theory [6].

Various approaches have previously been undertaken to predict CRP noise and a summary can be found in [7]. Based on his helicoidal surface theory for propellers [8], Hanson developed one of the first analytical models for CRP noise prediction [9]. In this approach, the sources were placed on the propeller advance surface which made the precise treatment of blade geometric details and non-uniform inflow effects challenging [6].

With the recent advances in numerical methods for aerodynamic and aeroacoustic analyses, hybrid methods based on coupling CFD (Computational Fluid Dynamics) and CAA (Computational Aeroacoustics) have also been pursued [10] [11] [12]. However, CAA methods are expensive in CPU time and memory requirements due to the high mesh densities required to accurately resolve acoustic pressure disturbances. Therefore, carrying out parametric studies in the CRP design phase using coupled CFD/CAA approaches is generally not yet feasible.

Analytical frequency approaches for single rotor [6] and counter-rotating propfan noise [9] require the a priori determination of unsteady blade surface pressures to define the acoustic source terms. In the past, difficulties in obtaining the aerodynamic

data have led to inaccurate noise results [6] but the emergence of CFD now provides the capability to estimate the unsteady blade loading.

In the present work, a new frequency domain approach for CRP noise estimation is developed by extending Hanson's single rotor noise approach [6] to counter-rotating configurations. In contrast to the helicoidal surface theory, sources are placed on the blade surfaces assuming the source data (surface pressure data and geometry) is available from an external calculation. High-fidelity full-wheel 3-D RANS simulations using the commercially available CFD tool Numeca FINE/Turbo are demonstrated to successfully generate the required surface pressure information. One of the main advantages of the developed CRP noise approach is the low computation time requirement allowing the method to be used for detailed parametric studies.

One of the primary concerns in developing a viable CRP engine design is the noise impact of open rotors, in terms of both in-flight cabin noise and takeoff/approach community noise. At cruise, thickness and loading noise are the key noise sources and the rotor-alone tones dominate the CRP spectrum. At the low-speed FAR 36 noise certification conditions during takeoff and approach, rotor-rotor interaction noise due to aerodynamic interference effects tends to dominate the noise signature [13]. The current work focuses on the investigation of CRP interaction tones in order to explore what characteristics and attributes are needed in a CRP design to meet future noise regulations.

It is assumed in this thesis that the mechanisms responsible for the CRP interaction noise can be attributed to the following unsteady flow features: (1) rear-rotor upstream influence interacting with the front rotor, (2) tip-vortices shed from the front rotor interfering with the rear rotor, (3) front-rotor viscous wakes affecting the rear-rotor loading, and (4) front-rotor hub wake and hub boundary layer influencing the rear-rotor hub loading [14].

Several CRP noise reduction technologies such as variations in rotor-rotor spacing, rotor tip speed, or rotor blade count [15] [16], as well as reductions in rear-rotor diameter [17] and blade wake management [18] [19] have been explored in the past. In general, reductions in interaction tones were observed when the effects of a single

noise reduction technology were investigated. For example, Janardan et al. [15] reported a 10 dB reduction in the summed interaction tone levels at the takeoff condition over a large range of polar emission angles when increasing the rotor-rotor spacing of a model scale CRP with 9 front- and 8 clipped rear-rotor blades by 40 %. However, a detailed experimental or computational evaluation of the effectiveness of the different CRP noise reduction technologies starting with the dissection of the above noise source mechanisms has not been carried out to date. The CRP noise estimation method developed in this thesis is used to quantify the influence of the underlying CRP noise mechanisms on interaction noise. Based on the results, the acoustic benefits of selected CRP noise mitigation concepts are investigated.

1.2 Research Questions

For CRPs to be a viable alternative to advanced high bypass ratio, low fan pressure ratio turbofan engine designs, both their aerodynamic and acoustic performance must be improved. The research described in this thesis is focused on establishing an integrated performance and noise assessment methodology for advanced propfan powered aircraft configurations. The methodology is applied to carefully defined CRP aircraft arrangements to answer the following research questions:

1. Since the CRP acoustic signature is tone noise dominated, are open rotors a viable alternative to high bypass ratio turbofans given the stringent noise certification requirements?

2. Based on the insight gained by dissecting and quantifying the relative importance of the source noise mechanisms responsible for CRP interaction noise, what are the characteristics and enabling noise mitigation technologies required to design a quiet propfan propulsion system?

3. Implementing advanced CRP noise reduction concepts, what are the trade-offs between acoustic and aerodynamic performance? What level of noise reduction can be achieved by implementing advanced source noise mitigation concepts?

The goal of this work is to quantify the potential acoustic benefits which can be achieved by implementing CRP noise reduction technologies on a consistent aircraft mission basis relative to advanced turbofan aircraft configurations. The success criterion is to demonstrate that CRPs of advanced design can achieve significant noise reductions while maintaining or improving aerodynamic performance.

1.3 Technical Roadmap

The objectives are to dissect and quantify the impact of the aerodynamic mechanisms responsible for CRP interaction tone noise and to design an advanced CRP configuration for improved acoustic performance with no penalties in aerodynamic performance. The following conceptual were carried out to answer the research questions stated above.

The first step is to establish an integrated aerodynamic and acoustic performance analysis methodology. The methodology is not limited to CRP powered aircraft configurations but is capable of also dealing with turbofan arrangements such that CRP performance results can be compared to advanced turbofan performance levels on a consistent mission basis. The overall performance and noise assessment framework consists of four major modules: mission analysis, propulsion system analysis, low speed performance assessment, and noise estimation.

The second step is to define the concept aircraft configurations. First, given a $3,500$ nm mission, a baseline aircraft configuration powered by a datum high bypass ratio, low fan pressure ratio turbofan was defined and used to validate the methods incorporated in the overall methodology. Next, based on the datum turbofan powered airframe, a baseline CRP arrangement was designed[1].

The integration of the CRPs necessitated modifications of the turbofan powered baseline airframe including a rearward shift of main wing and landing gear due to stability constraints and fuselage weight penalties due to structural reinforcements and

[1]Certification challenges such as blade containment are acknowledged but not taken into account in the present analysis.

cabin noise insulation. The baseline CRP gas turbine cycle was based on the datum turbofan and the CRP was sized to meet the thrust requirement at takeoff/top-of-climb. The development of the baseline CRP geometry was guided by data available in the literature [2] and the detailed aerodynamic design was finalized to match reported takeoff performance characteristics using single and dual rotor vortex-lattice methods.

The major challenge in developing the overall aerodynamic and acoustic performance assessment methodology is the assessment of the noise generated by the propfan rotor blades. Coupled CFD/CAA methods are too computationally expensive to carry out parametric studies exploring the benefits of CRP noise reduction technologies thus a first-principles based approach is preferred. Since the accuracy of the proposed frequency domain method is controlled by the accuracy of computing the aerodynamic interaction, a high-fidelity CFD approach is required. To estimate the CRP noise, the third step of the technical roadmap is to establish a frequency domain approach based on Hanson's single rotor noise method. The derived CRP noise method was validated by comparing the baseline CRP noise results to measured data available for the same CRP configuration albeit with differences in the exact details of the blade profiles.

In order to accurately capture the aerodynamic interaction between the CRP blade rows and to determine the unsteady blade surface pressures necessary to define the acoustic source terms, the fourth step is to establish a high-fidelity CFD method. To this end, a full-wheel 3-D unsteady RANS approach was implemented. A meshing strategy was developed with the aim on minimizing computational costs. Detailed grid convergence and time step studies were carried out to ensure that underlying CRP flow features (front-rotor tip-vortices and viscous wakes, rear-rotor upstream influence, and hub wake and boundary layer) are adequately resolved.

The CRP noise method derived in this thesis allows to analyze the influence of the noise source mechanisms inherent to CRP applications. In order to determine the required characteristics and define necessary design features of a quiet CRP configuration, the noise source mechanisms were dissected and their respective impacts were

quantified for the baseline CRP definition. Based on the results of this noise source investigation, the baseline CRP was re-designed for reduced noise incorporating CRP source noise mitigation concepts. The aerodynamic performance was maintained in the re-design. The resulting advanced design CRP was again assessed for noise and the achieved interaction tone reductions were quantified.

Finally, noise results at the FAR 36 observer locations are presented on the aircraft system level for the baseline CRP and advanced design CRP aircraft configuration. The CRP noise levels were compared to the datum turbofan powered aircraft in order to evaluate the relative acoustic performance and determine what noise levels can be achieved with an advanced open rotor design.

1.4 Thesis Contributions

A multidisciplinary integrated noise and performance assessment capability was established to evaluate the acoustic and aerodynamic performance of advanced CRP designs on the aircraft/engine system level. A frequency domain method based on extending Hanson's single rotor noise approach to counter-rotating propfan configuration was implemented to assess the CRP noise levels. The approach was coupled with high-fidelity full-wheel 3-D unsteady RANS simulations to capture the underlying CRP noise source mechanisms and to determine the time-varying blade surface pressures necessary to define the acoustic source terms. The method is capable of exploring source mitigation concepts and conducting parametric studies

A detailed quantitative assessment of the underlying noise source mechanisms was conducted for a baseline CRP design guided by data available in the literature. The results indicate that although certain interaction tones are dominated by related mechanisms, in order to achieve significant interaction tone noise reductions, all noise source mechanisms need to be addressed. The acoustic performance assessment of a re-designed CRP incorporating advanced source mitigation concepts suggests that it is possible to meet Chapter 4 noise limits with advanced open rotor designs[2].

[2]Subsonic transport category large aircraft certified after January 1, 2006, must demonstrate

noise levels no greater than the Stage 4 noise limit prescribed in section B36.5 of the FAR 36 noise standards [20].

Chapter 2

Integrated Aircraft Performance and Noise Assessment Methodology

An overview of the integrated aircraft performance and noise assessment framework is depicted in Figure 2-1. The methodology consists of four major modules and is capable of assessing both turbofan and propfan powered aircraft configurations.

The overall framework begins with the mission analysis. After defining the mission to be studied, the aircraft planform and the propulsion system are selected. A weights and balance assessment is performed first. The mission and aircraft data are inputs to the second module of the overall framework, the analysis of the engine. The most important parameters fed into this module are the thrust and power requirements at takeoff/top-of-climb, and at the cruise design point. A suitable engine capable of meeting the required thrust values is defined and the engine cycle analysis is performed. The resulting engine definition is passed back to the mission assessment module to obtain updated weights, balance and performance results. This process is iterated until an aircraft/propulsion system is determined which meets the mission requirements. The performance data of the selected aircraft is input to the takeoff and approach performance analysis module, the third major part of the overall methodology. The low speed drag polars are computed and takeoff and approach

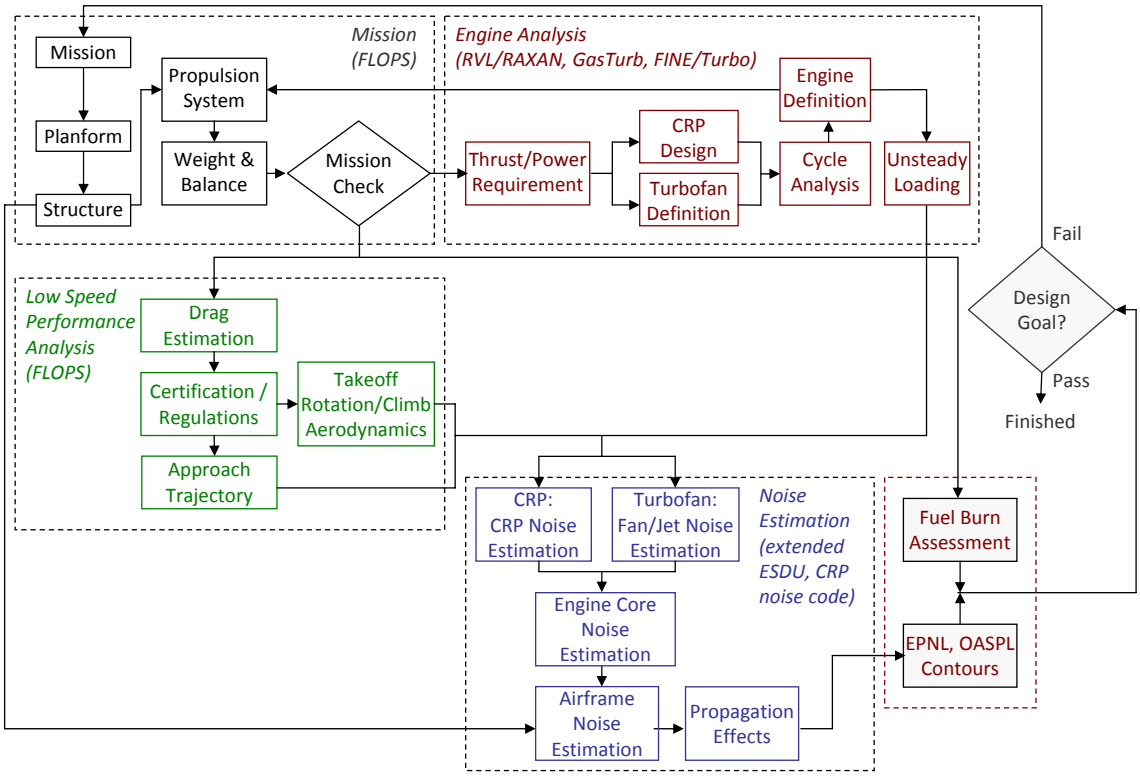

Figure 2-1: Integrated aircraft performance and noise assessment methodology for turbofan and propfan configurations

trajectories are obtained following the FAA regulations specified in [21].

The last module of the overall methodology is the aircraft/propulsion system noise estimation. The results of the analyses above are used as inputs: the aircraft structural definition is required for the airframe noise estimation, various engine cycle parameters and the unsteady blade loading in the case of a CRP powered aircraft are needed for the engine noise calculations, and the takeoff and approach trajectories are required to compute propagation effects. Finally, the overall framework provides fuel burn results in terms of SFC and noise results in terms of EPNL and OASPL contours.

The methodology developed in this thesis can be used to quantify the acoustic benefits of advanced CRP noise reduction technologies (e.g. increased rotor-rotor axial spacing, reduced rear rotor diameter, or differential tip speeds) on the propfan/aircraft system level. Moreover, the methodology allows to investigate the effects of noise reduction technologies on the aerodynamic performance of CRP powered aircraft. The following sections deal with the details of the aforementioned modules starting with the mission analysis.

2.1 Mission Analysis

In the mission analysis module, the airframe, engine type, and engine/airframe integration parameters are specified. The component weights are calculated and a detailed mission performance analysis is performed using NASA's Flight Optimization Software FLOPS [22]. FLOPS is a multidisciplinary system for the conceptual and preliminary design and evaluation of advanced aircraft concepts and is composed of nine primary modules: weights, aerodynamics, engine cycle analysis, propulsion data scaling and interpolation, mission performance, takeoff and landing, noise footprint, cost analysis, and program control.

The developed methodology depicted in Figure 2-1 primarily uses FLOPS' weights, aerodynamics, mission performance, and takeoff and landing modules. The engine cycle analysis and noise estimation approaches implemented in FLOPS are dated

1994 and 1981, respectively. The developed methodology is required to be capable of assessing high bypass ratio, low fan pressure ratio turbofan designs. However, the correlations included in the FLOPS methods are not always applicable to advanced turbofan configurations. Therefore, higher-fidelity methods were applied for engine analysis and noise assessment as outlined in Sections 2.2 and 2.4, respectively.

The weights module uses empirical relationships to predict the weight of each item. The input parameters consist of the airframe dimensions. The main wing geometry can be input in more detail in terms of the airfoil characteristics at several spanwise stations. The propulsion system weight is based on the engine thrust rating. The fidelity of the propulsion system weight prediction can be increased by specifying further engine parameters such as nacelle dimensions. In addition, any component weight estimation results from external assessments can be included in the calculations. The FLOPS weight module was validated using a datum turbofan aircraft configuration and the results are presented in Section 3.1.

A modified version of the Empirical Drag Estimation Technique (EDET) [23] is applied for the aerodynamic performance assessment. Modifications include smoothing of the drag polars and more representative Reynolds number calculations [22]. The aerodynamic performance calculations in FLOPS were also validated using an advanced turbofan aircraft configuration with the results described in detail in Chapter 3.1.

The calculated weight and aerodynamic data are used in the mission analysis module to compute the aircraft mission performance. As outlined in the next section, the required engine data is computed using the cycle analysis tool GasTurb, and vortex-lattice and 3-D RANS calculations in the case of a propfan powered aircraft configurations.

Takeoff, climb, cruise, and descent segments are included in the mission simulations. The mission fuel assessment includes calculations of fuel reserves to account for flight to an alternate airport and a specified hold segment as required by the FAA. Iteratively, FLOPS provides performance data for each specified segment including detailed fuel burn results.

2.2 Engine Analysis

For a given mission, the thrust requirements at takeoff/top-of-climb and cruise determined in FLOPS are input into the engine analysis module. The cycle analysis for the specified turbofan or CRP gas generator is performed in GasTurb 11 [24]. GasTurb allows to compute the cycle parameters at both design and off-design conditions. The design point cycle analysis is used to evaluate the fuel burn. At off-design conditions during takeoff and approach, the cycle analysis provides the engine parameters required for the noise assessment as described in Section 2.4.

In the case of a CRP powered aircraft, the aerodynamic design of the propfan is carried out at the low-speed takeoff condition using the single and dual rotor vortex-lattice methods, Rotor Vortex Lattice (RVL) and Rotor AXisymmetric ANalysis (RAXAN) [25] as outlined in Section 3.2. At both takeoff and approach, RVL/RAXAN calculations are performed to iteratively find the optimum operating conditions meeting the thrust requirements obtained in FLOPS. In addition, RVL/RAXAN simulations yield the shaft power to be provided by the CRP gas generator.

RVL/RAXAN does not account for compressibility effects and therefore cannot be used at cruise. 3-D steady RANS simulations are required to conduct CRP performance studies at cruise. However, in order to optimize the CRP at cruise for propulsive efficiency, parametric studies including tip speed and blade angle setting variations are necessary. Due to data processing and CPU time limitations, detailed parametric studies using 3-D RANS computations are challenging. Thus, the cruise optimization of the CRP configuration could not be performed within the scope of this research but can be carried out in the future.

The focus of the CFD simulations is on noise assessment. In order to determine the time varying blade surface pressures required for the CRP acoustic analysis, full wheel unsteady 3-D RANS simulations of the counter-rotating stage are performed using Numeca FINE/Turbo [26]. The CRP noise assessment and CFD simulations are described in detail in Chapter 4.

As illustrated in Figure 2-1, the engine parameters obtained in the engine cycle analysis are used as inputs to the mission performance assessment in FLOPS. Iteratively, the engine/aircraft configuration characteristics required to meet the mission constraints are determined.

2.3 Low Speed Performance Analysis

In the low speed performance analysis module, the takeoff and approach trajectories required for the noise audit are computed by combining an external low speed drag polar method with the low speed aerodynamics assessment method included in FLOPS. The low speed drag polar method is needed since FLOPS requires the input of detailed lift and drag coefficient data at takeoff and landing to generate the trajectories. The method implemented in this work was developed by March [27] and calibrated using a combination of Boeing flight test data, NASA wind tunnel results, and an empirically-tuned Lockheed method. The method is generally capable of predicting clean-configuration drag polars with about 1 % error while calculations including deployment of high-lift devices have about 3 % error.

In addition to the takeoff and landing trajectories, the low speed performance module in FLOPS computes the all-engine takeoff field length, the balanced field length including one-engine-out takeoff and aborted takeoff, and the landing field length. Moreover, the approach speed is calculated, and the second segment climb gradient and the missed approach climb gradient are evaluated [22]. It is ensured that all FAR 25 [21] requirements are met. If limited takeoff and landing field lengths are prescribed, the flap and slat deflection angles are iteratively varied in the low speed drag polar method until operating conditions are found such that the field length conditions are satisfied.

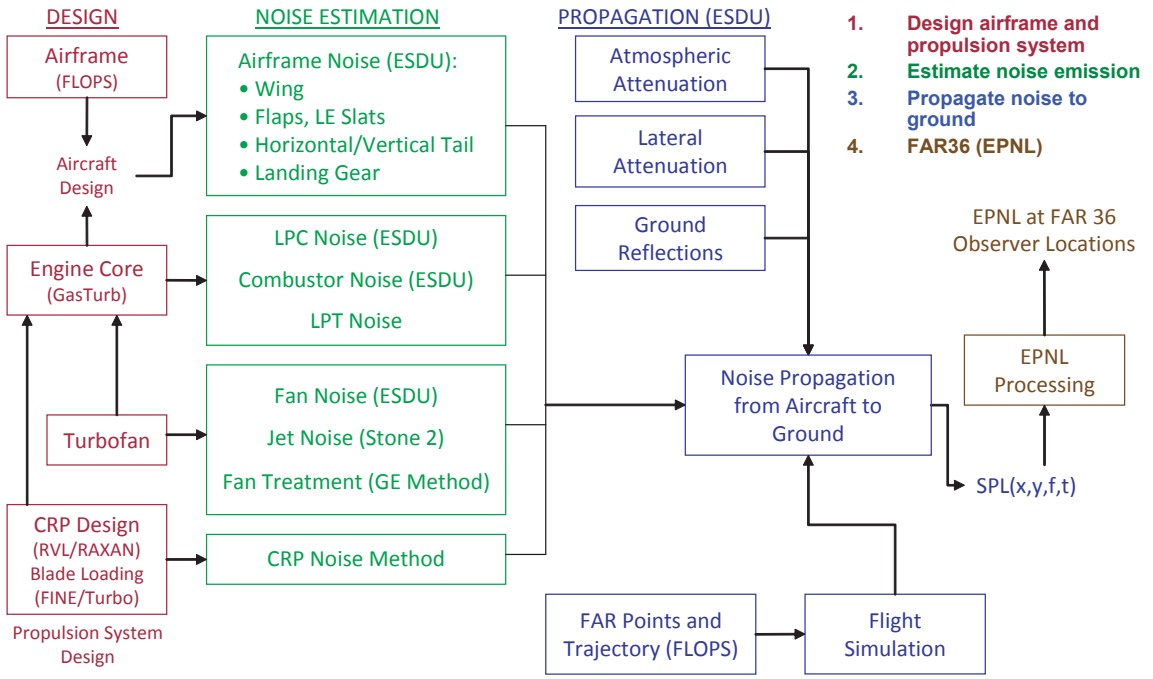

Figure 2-2: Noise assessment framework

2.4 Noise Audit

The takeoff and landing trajectories, airframe characteristics, engine cycle data, and unsteady blade surface pressures in the case of a CRP configuration are required for the noise assessment as shown in Figure 2-1. The main thrust of this thesis is focused on the estimation of the noise generated from the CRP rotors and the development of the CRP noise estimation approach is given in detail in Chapter 4. In addition, a combination of existing analytical and empirical methods is used to compute the noise from airframe, engine core sources, and fan in the case of a the acoustic assessment of a turbofan configuration and to account for noise propagation effects to the FAR 36 certification locations.

An overview of the noise assessment module is presented in Figure 2-2. Using data from FLOPS, GasTurb, and FINE/Turbo, the aircraft/propulsion system noise estimation is subdivided into the evaluation of airframe noise, engine core noise, fan and jet noise in the case of a turbofan powered aircraft, and rotor noise in the case of a CRP powered configuration.

All noise calculations are carried out at ISA +10 °C day, 70 % humidity, zero wind, and sea level conditions. The metric used for FAR 36 noise certification is the effective perceived noise level (EPNL) [20]. It is computed from the instantaneous sound pressure level in each of the 24 one-third octave bands for each 0.5 s increment along the aircraft takeoff or landing trajectory. The sound pressure levels are converted into perceived noise levels, based on noy, and corrected for tones and duration of the sound to capture the effective perceived noise, in EPNdB, generated from the aircraft/propulsion system configuration at each of the sideline, flyover, and approach observer locations. In addition to EPNL calculations, which are based on the one-third octave sound pressure levels, the method is capable of computing noise contours in A-weighted overall sound pressure level (OASPL) for a given aircraft position during takeoff or approach. The methods incorporated in the noise assessment module are briefly described below.

2.4.1 Airframe Noise

The noise generated by the airframe is computed with ESDU's airframe noise module which uses semi-empirical methods proposed by Fink [28] and Zorumski [29] with modifications to directivity and spectral functions based on recently available data [30]. The method can be used to estimate airframe noise from the following sources: main wing, flaps, leading edge slats, horizontal tail, vertical tail, and nose and main landing gear[1]. The spectral and directivity characteristics of the these airframe sources were derived analytically or empirically, or were assumed similar to sources of known characteristics [30]. Acoustic interaction between the components is not accounted for. Required inputs include span and area data for the main wing, tails, and flaps, as well as flap and slat deflection angles. Number and diameter of nose and main landing gear wheels are needed along with strut lengths to compute the landing gear noise.

[1]Most of the fluctuating lift and drag forces governing airframe noise are associated with the noise from the wing, tail, and landing gear. The noise contribution from the fuselage is considered negligible, even though the fuselage produces some lift.

2.4.2 Engine Core Noise

The engine core noise estimation is subdivided into noise generated from the low-pressure compressor (LPC), the combustor, and the low-pressure turbine (LPT). The noise from high pressure compressor and high pressure turbine is not accounted for, as their contribution is negligible compared to the low-pressure components.

1. **LPC Noise**

   The noise from the LPC is calculated using the fan/compressor noise module in ESDU [31] which is based on Heidmann's method [32] and is a modified version of the Boeing-Ames procedure given in [33]. The noise radiated from inlet and discharge duct is computed separately, in both cases broadband and tone noise components are accounted for. In addition, multiple-pure-tone noise or "buzz-saw" noise is calculated in the inlet duct when the relative tip speed is supersonic. For multi-stage compressors, the final spectrum is obtained by summing the sound energy from each stage. Blade row attenuation is included in the calculations based on empirical data depending on the number of rotor and stator blades in each stage. The method predicts the spectral shape, level and free-field directivity. Corrections applied to the basic spectrum levels depend on the presence or absence of inlet guide vanes, the rotor-rotor spacing, inlet flow distortions during low speed ground-roll operations, and tone cut-off where the fundamental tone is suppressed according to a criterion determined by the number of rotor and stator blades and the value of the rotor tip Mach number.

   The main input parameters required for the LPC noise estimation are the mass flow rate, the stagnation temperature rise for each compressor stage, both design and operating point values of the rotor tip relative inlet Mach number, and certain fan geometry data (rotor-stator spacing and number of rotor and stator blades for each blade). The required cycle parameters are computed in the engine analysis module using GasTurb.

2. **Combustor Noise**

   Combustor noise is computed using the combustor noise module in ESDU [34]

which was developed based on the semi-empirical method described in [35]. The method accounts for noise of the combustion itself, propagating out of the engine through the exhaust nozzle, and entropy noise, generated when the hot turbulent products of the combustion process pass through the pressure gradients in the turbine stages downstream of the combustor. The mass flow rate through the engine core, the stagnation pressure and temperature at the combustor inlet and exit, and the stagnation temperature drop across the turbine components are needed to assess the combustor noise.

3. **LPT Noise**

   ESDU does not include a turbine noise estimation capability, thus a semi-empirical method developed by Dunn and Peart [33] was implemented as presented in [36]. The input requirements consist of the mass flow rate, the static and stagnation temperatures at the turbine exit, the rotor tip speed, as well as the number of blades and the ratio of stator chord to stator-rotor spacing. Applying this method to the advanced turbofan engine outlined in Section 3.1, however, provided noise levels significantly higher than expected for an advanced LPT design. The discrepancies are suggested to be due to the method not being applicable to more recent turbine designs. In the light of these observations, corrections were applied to the calculated LPT noise based on discussions with the project industry partner.

2.4.3 Turbofan Powered Aircraft: Fan and Jet Noise

For a turbofan powered aircraft, fan and jet noise need to be estimated.

1. **Fan Noise**

   The compressor noise module in ESDU is also applicable to fan blade rows, thus the method described above was used for fan noise assessment with inputs calculated from the cycle analysis. Multiple-pure-tone noise caused by blade-to-blade variations is accounted for in the fan noise method.

   The attenuation spectra due to acoustic treatment in the turbofan inlet and

aft fan duct are determined using an empirical method developed by Kontos et al. [37]. Input requirements include the treatment length up- and downstream of the fan, as well as the fan inlet radius and the aft fan duct height. The computed attenuation spectra are then applied to the fan sound pressure levels obtained using ESDU's compressor noise module.

2. **Jet Noise**

   The jet noise module incorporated in the noise audit methodology is capable of dealing with single and coannular exhaust nozzles. A semi-empirical method developed by Stone et al. [38] was implemented. For a dual stream jet, the noise sources contributing to the overall jet noise are attributed to the following mechanisms: (1) inner stream mixing noise (mid to high frequency noise) generated by the shear layer between primary and secondary jet stream, (2) outer stream mixing noise (high frequency) due to small scale mixing near the nozzle exit, and (3) merged mixing noise (lowest frequency) generated by the mixing of coherent large scale turbulent jet structures with the ambient flow downstream of the nozzle exit. In addition, a plug separation noise component (high frequency) is present in nozzles with center plugs. The Stone jet noise method includes all of the above noise source mechanisms. The method requires the nozzle flow properties (core and bypass stream nozzle exit velocities, stagnation temperatures, and mass flow rates) computed in GasTurb and the geometric dimensions of the nozzle.

2.4.4 Propfan Powered Aircraft: CRP Noise

In the case of a CRP powered aircraft configuration, counter-rotating propfan noise is computed using the CRP noise estimation method described in Chapter 4. The frequency domain CRP noise method developed here requires the time-varying blade surface pressure data computed using 3-D unsteady RANS simulations. Additional required inputs are the CRP operating conditions during takeoff and approach. The low-speed off-design data is determined using vortex-lattice methods and the low-

speed performance assessment module in FLOPS as outlined in Chapters 2.2 and 2.3, respectively.

2.4.5 Propagation Effects

The above methods include spherical spreading effects. The sound pressure levels at the observer decrease in intensity with the square of the propagation distance from the source. However, sound pressure levels are further attenuated by atmospheric molecular absorption. Atmospheric absorption varies linearly with distance and the rate of attenuation depends on frequency and varies with ambient temperature, pressure, and humidity. The attenuation due to atmospheric absorption is estimated using atmospheric absorption method in ESDU [39]. In addition, the noise received by the observer is influenced by ground reflection effects. Sound waves directly from the source and sound waves reflected off the ground surface are simultaneously received at the observer location. The emitted and reflected waves cause local constructive and destructive interference. Ground reflection effects depend on frequency, the distance of the observer from the reflecting surface, and local ground impedance. The influence of ground reflection on the noise received at the observer is evaluated using the procedures described in [40] and [41].

2.4.6 Post-Processing for FAR 36 Noise Assessment

Using the airframe characteristics, engine cycle parameters, unsteady CRP blade loading, and takeoff and approach trajectories as input data, the noise results from the above sources are post-processed in Matlab and EPNL values are obtained at the FAR 36 observer locations. However, in order to reduce computational cost, only three off-design conditions are simulated to determine the required engine cycle properties for the flyover and sideline observer locations: (1) at Mach 0.1, (2) when the aircraft begins rotation, and (3) at cutback. The engine parameters are then assumed to be approximately constant between two off-design conditions. Similarly, the cycle properties are approximately constant during the final part of the approach trajectory

and the required engine parameters are computed only for the flight condition at $6,560$ ft ahead of the runway which corresponds to the aircraft being directly above the approach observer position.

2.4.7 Summary

In summary, an integrated framework for the aerodynamic and acoustic performance assessment of turbofan and propfan powered aircraft arrangements was established in this chapter. Existing analytical and empirical methods were implemented for the mission analysis, engine cycle assessment, low-speed performance calculations, and the noise prediction of airframe, engine core, and fan sources. Corrections based on trends observed in advanced engine designs were applied to the calculated turbine noise results as the available method is not applicable to advanced turbine configurations. The methods described in this chapter are necessary in order to assess aircraft noise at the FAR 36 observer locations and the methods were validated using a given turbofan powered aircraft definition as discussed in the next chapter. The overall focus of this thesis is on the development of a high-fidelity CRP noise estimation approach which is incorporated in the noise framework illustrated in Figure 2-2. The developed CRP noise method is described in detail in Chapter 4.

Chapter 3

Concept Aircraft Definitions

Advanced open rotor designs are regarded as potential propulsion systems mostly for future short- to medium-range narrow-body aircraft. A 737 size twin engine aircraft was defined as a representative baseline configuration. The selected aircraft seats 150 passengers and has a range capability of $3,500$ nm at cruise Mach number 0.78. An advanced high-bypass turbofan engine was chosen as the propulsion system. This datum turbofan aircraft configuration was used to validate the overall methodology and provides a basis for comparison for the CRP powered aircraft arrangements which are the focus of this research. The definition of the datum turbofan/baseline airframe configuration is described in detail in the first part of this chapter.

Powered by two aft fuselage pylon mounted pusher CRPs, a second aircraft based on the airframe of the turbofan powered aicraft and for the same mission was defined next and is denoted as the baseline CRP configuration throughout this thesis. The design of the CRP engine and the modifications to the baseline airframe due to the integration of the CRPs are outlined in the second part of this chapter.

3.1 Datum Turbofan Powered Aircraft

An overview of the mission and baseline airframe definitions is given first. Next, a description of the datum turbofan engine is presented, followed by a summary of the analysis of the datum turbofan aircraft aerodynamic and acoustic performance.

3.1.1 Mission and Airframe Definition

The baseline aircraft characteristics and mission requirements were defined in collaboration with the project industry partner. The mission specifications are summarized in Table 3.1. Based on the tabulated requirements, a datum turbofan powered aircraft configuration was defined and a detailed performance study and mission analysis was conducted using the tools included in the integrated performance framework shown in Figure 2-1.

Table 3.1: Overall baseline aircraft characteristics and mission requirements

Seating capacity	150
Range capability	$3,500$ nm
Design cruise Mach number	0.78
Thrust sizing ICAC	$35,000$ ft with 500 ft/min ROC
Takeoff field length requirement	$6,500$ ft MTOGW/SL/ISA+27 F

The baseline aircraft features two wing mounted advanced turbofan engines with a takeoff static thrust of $24,000$ lb. The primary characteristics of the aircraft include a maximum takeoff weight of $MTOW = 152,400$ lb, an overall length of 127 ft, and a span of 113 ft. The geometric dimensions of fuselage, main wing, and tails are presented in detail in Appendix A.

3.1.2 Definition of Datum Turbofan Engine

With future design trends and noise regulations in mind, potential propfan propulsion systems need to be assessed relative to the projected performance levels of advanced turbofans. Therefore, a high bypass ratio, low fan pressure ratio turbofan engine was selected to power the baseline aircraft. The engine is a two-spool unmixed flow configuration and the characteristic parameters are summarized in Table 3.2. The component efficiencies were agreed on in discussions with the industry partner.

In order to verify the calculations performed in GasTurb, cruise design point simulations were carried out for the CFM56-7B20. The CFM56-7B20 is used today powering the Boeing 737-700, which is similar in size to the baseline aircraft and therefore

the generated thrust levels are similar to the selected datum turbofan performance. The computed specific fuel consumption for the datum turbofan of advanced design shows a reduction of 11 % compared to CFM56-7B20 as indicated in Table 3.2. Both the computed datum turbofan and the calculated CFM56-7B20 performance and fuel burn results were carefully checked for consistency with the industry partner.

Table 3.2: Datum turbofan engine characteristics at cruise design point compared to CFM56-7B20 characteristics (extracted from [1])

	Datum Turbofan	CFM56-7B20
Bypass ratio	8.9	5.5
Fan pressure ratio	1.49	1.65
Overall pressure ratio	36.5	25.6
Turbine inlet temperature	2,770 R	2,700 R
Thrust	4,800 lb	4,640 lb
Specific fuel consumption	0.536 lb lbh	0.603 lb lbh

As described in Chapter 2, design and off-design computations are performed in GasTurb to determine the fuel burn and the cycle properties required for the noise assessment. These calculations take into account the details of the internal air system including the cooling air mass flows for the high pressure turbine (HPT), the nozzle guide vanes, and the LPT. In addition, the simulations include a pre-defined overboard bleed mass flow.

3.1.3 Datum Turbofan Aircraft Aerodynamic and Acoustic Performance

The turbofan powered aircraft configuration is sketched on the left in Figure 3-1. It should be noted that the dimensions are not drawn to scale. The results for the weight breakdown, aerodynamic performance, and noise assessment are summarized below.

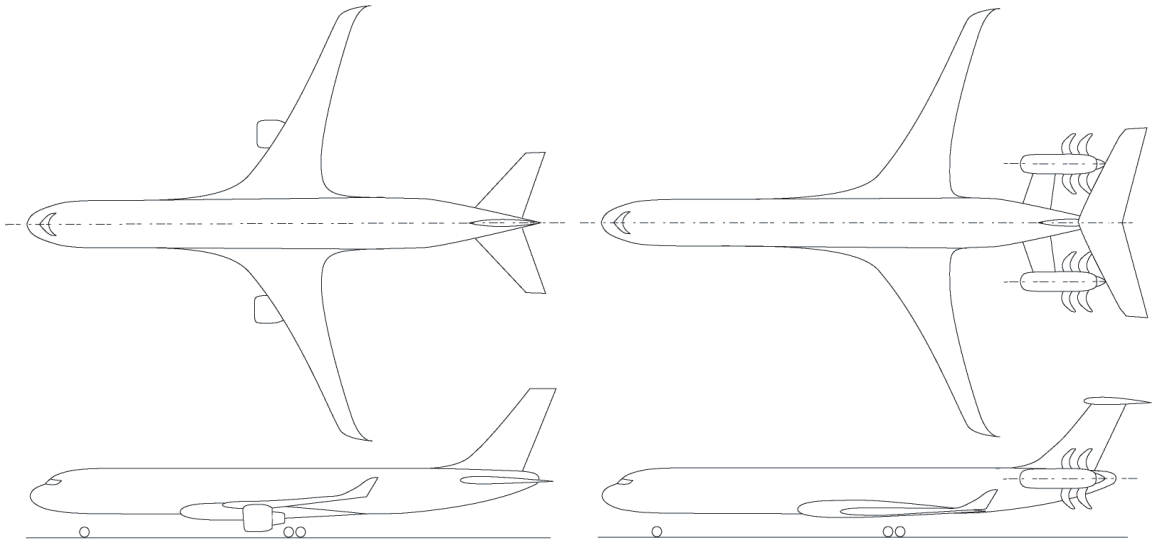

Figure 3-1: Concept aircraft definitions: Datum turbofan aircraft (left) and baseline CRP aircraft (right) configurations (sketches not to scale)

3.1.4 Weight Breakdown

The component weights computed in FLOPS are compared to the values provided by the industry partner in Table 3.3. It was assumed that 15 % composites are integrated in the wing structure. The fuselage weight was scaled down to 80 % of the value computed by FLOPS to account for composites used in the structural design. The engine weight results computed by FLOPS differed significantly from the data expected for advanced turbofans, mainly due to an unreasonably high thrust reverser weight. Based on the correlation given in [42], the weight of the thrust reversers included in the engine installation group was thus adjusted to 15 % of the primary engine weight. For the major component groups, the weight results computed in FLOPS agree to within 3 % with the data provided by the industry partner. The landing gear weight is the most notable exception. The discrepancies here are due to differences in the weight estimation methods. However, the overall weight data such as MTOW agree to within 2.5 %, thereby verifying the weight prediction module implemented in FLOPS.

Table 3.3: Datum turbofan aircraft weight breakdown: Component weights computed in FLOPS and relative error of calculated results to data provided by the industry partner

Component Breakdown	Computed Weight in lb	Relative Error to Industry Data in %
Airframe Structure	37,900	**2.75**
Wing	14,300	0.29
Fuselage	14,900	−0.15
Tails	3,100	−12.07
Landing gear	5,600	33.72
Aircraft Systems	8,100	**1.64**
Electronic Systems	2,700	**-4.50**
Electronics	2,200	−1.79
Instruments	500	−15.17
Engine Installation	8,200	**0.16**
Primary engine	7,200	0.42
Wing installation	1,000	−1.67
Furnishings and Equipment	11,900	**-0.76**
Manufacturer's Empty Weight (MEW)	77,000	**0.54**
Operating Empty Weight (OEW)	84,200	0.51
Maximum Zero Fuel Weight (MZFW))	123,800	0.49
Maximum Payload Weight	19,600	0.45
Maximum Takeoff Weight (MTOW)	155,500	**2.03**
Maximum Landing Weight (MLW)	133,800	**2.46**

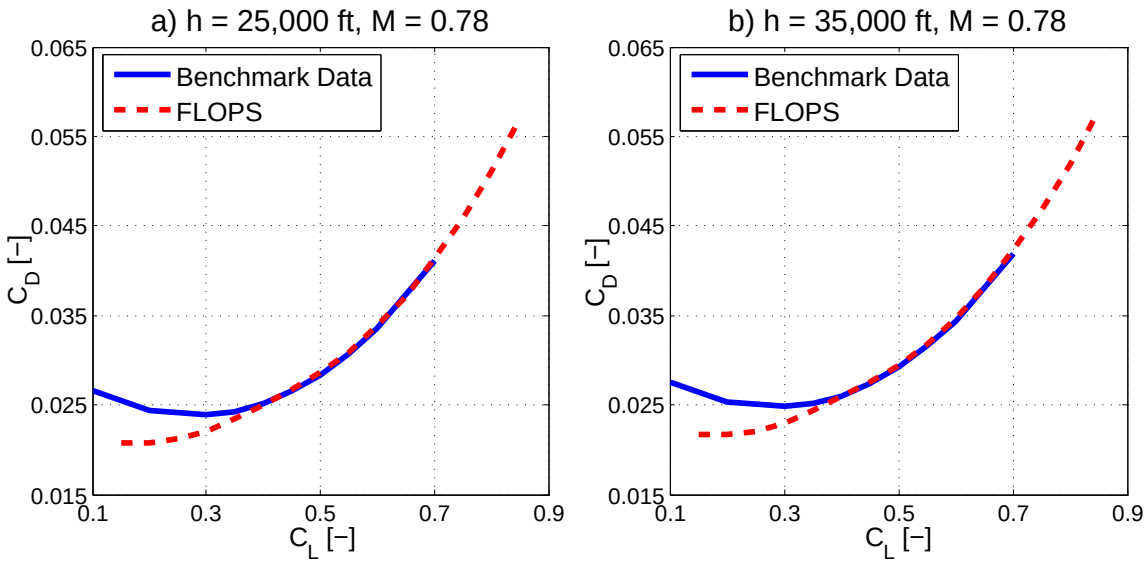

Figure 3-2: Analysis of the datum turbofan aircraft aerodynamic performance at a) $h = 25,000$ ft, $M = 0.78$ and b) $h = 35,000$ ft, $M = 0.78$

3.1.5 High Speed Aerodynamic Performance

To validate the aerodynamic performance analysis performed in FLOPS, high speed drag polar results were compared to data provided by the industry partner. The drag polars are presented for two flight conditions at cruise Mach number 0.78 in Figure 3-2 a) and b). Good agreement is observed for the lift coefficient range relevant for cruise conditions ($0.4 < C_L < 0.55$). The discrepancies for $C_L < 0.4$ are due to the drag estimation technique implemented in FLOPS not being applicable to flight at low lift coefficients [23]. Overall, drag polars were compared for altitudes in the range of $1,000$ ft$< h < 40,000$ ft and Mach numbers $0.4 < M < 0.8$. For all investigated flight conditions the results showed similar behavior to the trends observed in Figure 3-2.

3.1.6 Low Speed Aerodynamic Performance

Using the low speed drag polar method presented in Chapter 2.3, the low speed performance of the datum turbofan aircraft was analyzed. The takeoff and landing field lengths are mostly controlled by the flap and slat settings. The flap and slat

angles were iteratively varied until the mission requirements were met (maximum FAR 25 takeoff and landing field lengths $\leq 6,500$ ft). The final flap and slat settings and the resulting takeoff and landing field lengths for the datum turbofan aircraft configuration are tabulated in Table 3.4.

Table 3.4: Datum turbofan aircraft low speed performance assessment

	Takeoff	**Landing**
Flap setting	10°	35°
Slat setting	19°	35°
Field length	6,500 ft	6,470 ft

3.1.7 Noise Assessment

The overall methodology depicted in Figure 2-1 was executed to obtain the system level noise results for the datum turbofan aircraft configuration. Using the noise estimation methods outlined in Chapter 2.4, EPNL values were calculated at the three FAR 36 observer locations. The results are tabulated in Table 3.5. Compliant with the regulations stated in [20], the sideline EPNL was computed by iteratively varying the axial observer location until the maximum total noise level along the sides of the runway at a distance of 450 m is determined.

Table 3.5: Total datum turbofan aircraft EPNL in EPNdB

FAR 36 Observer Location	Datum Turbofan/ Baseline Aircraft
Flyover	87.6
Sideline	89.7
Approach	96.8

For aircraft powered by high-bypass ratio turbofan engines, the takeoff noise levels are dominated by fan and jet noise, while the fan and airframe sources govern the approach noise [43] [44]. The noise results computed for the datum turbofan aircraft configuration, presented in Figure 3-3, reflect these trends.

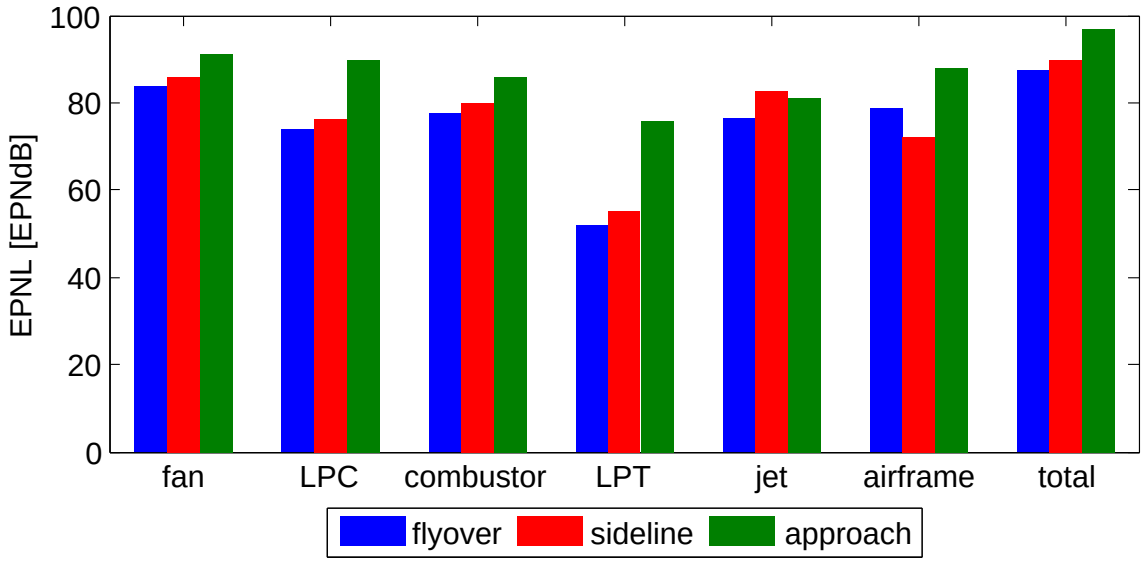

Figure 3-3: Total and component acoustic performance of datum turbofan aircraft at FAR 36 observer locations

The total and component EPNL results for the datum turbofan aircraft configuration were validated using data from an in-house noise assessment at the project industry partner. It was observed that the fan/LPC and fan treatment noise modules used in the developed noise assessment framework tend to overestimate the noise levels from the fan and LPC sources for an advanced turbofan configuration. The fan and fan treatment noise modules are based on correlations derived from experimental data for current turbofan configurations. Computing fan noise from an advanced fan design requires extrapolation of the measurement data potentially leading to significant inaccuracies. During the validation of the fan noise method carried out by ESDU, the RMS error between measured and one-third octave band sound pressure levels and estimated noise results was up to 5 dB [31].

However, given the overall goal of the present work to compare the noise from advanced CRP powered aircraft configurations on a relative basis, the methods were deemed adequate. More details on the noise results of the turbofan and propfan powered aircraft arrangements are given in Chapter 6.

In summary, a 150-seat advanced turbofan aircraft configuration with medium

range capability was developed. The overall aerodynamic and acoustic performance assessment methodology was executed for this datum turbofan aircraft and the results were used to validate the implemented methods.

3.2 Baseline CRP Powered Aircraft

The baseline CRP powered aircraft was defined based on the airframe of the datum turbofan aircraft and for the mission specified in Table 3.1. The CRPs are in aft fuselage pylon mounted pusher configuration as sketched on the right in Figure 3-1. The modifications due to the integration of the CRPs into the baseline airframe presented above are summarized first. Next, a detailed discussion of the baseline CRP aerodynamic design is given followed by the description of the engine.

3.2.1 Modifications to Baseline Airframe

The integration of the CRPs necessitated modifications to the baseline airframe. These included a rearward shift of the main wing and landing gear to meet static stability requirements. In addition, the component weight breakdown and the overall aircraft weights were significantly affected due to the installation of the CRP propulsion system.

The weight changes relative to the datum turbofan aircraft are summarized in Table 3.6. Propfan blades, gearbox, and larger pylons resulted in a propulsion system weight increase compared to the datum turbofan engine. The assumptions for the propulsion system weight are based on findings presented in an investigation by Goldsmith [45], which concerns the feasibility of a propfan propulsion system relative to a turbofan based propulsion system for the Douglas DC-9 Super 80. The study presents detailed component weight and aerodynamic and acoustic performance comparisons with the baseline turbofan aircraft for three propfan arrangements (the propfans are single-rotating, 13.8 ft in diameter). The results were used estimate the weights of the baseline CRP rotors (12.5 ft in diameter, see Section 3.2.2) and nacelle as well as the fuselage weight penalty due structural reinforcements to support the CRP engine

Table 3.6: Weight changes for the baseline CRP powered aircraft relative to the datum turbofan aircraft configuration

Component	**Weight Change**
Propulsion system (per engine)	
Gearbox	+500 lb
Pylon and nacelle	+1,500 lb
CRP core and propfan relative to primary turbofan engine	+550 lb
Fuselage	
Noise insulation	+800 lb
Structural reinforcements	+1,500 lb
Landing gear	+300 lb
Vertical tail	+200 lb
Mission fuel	−2,900 lb
MTOW	+5,000 lb

mounting structure.

For an aft fuselage pylon mounted propfan configuration, the study by Goldsmith suggests an increase of 1,000 lb in primary engine weight per engine (engine core, propfan blades, gearbox) relative to the baseline turbofan arrangement. In this thesis, it was assumed that some weight benefit can be reached due to the advances in materials since the 1981 single-rotating propfan study by Goldsmith. It was determined in discussions with the industry partner that an increase of 1,050 lb in primary engine weight is adequate even though the current study concerns counter-rotating propfans instead of single-rotating configurations. Furthermore, for the aft fuselage pylon mounted propfan aircraft arrangement, the study by Goldsmith indicates a 4,600 lb increase in the total weight of nacelle, mounting structure, and fuselage structural reinforcements relative to the baseline turbofan configuration. In the present work, a similar increase of 4,500 lb was assumed, of which 3,000 lb are attributed to the pylon and nacelle weight, and 1,500 lb are attributed to the reinforcements required in the fuselage structure.

In addition to propulsion system weight changes, fuselage weight penalties due to cabin noise insulation needed to be accounted for. Two approaches were investigated: 1) Insulating the entire fuselage with a trim insulation material in use in current

aircraft [46], or 2) insulating only the aft fuselage structure near the CRP engines with trim panels of 1980 vintage used in the study by Goldsmith [45]. The resulting weight penalties were approximately 800 lb in both cases. Consequently, this value was assumed for the fuselage weight increase due to cabin insulation.

The mission fuel requirement was significantly reduced due to the propulsive efficiency and fuel burn benefit of the baseline CRP aircraft compared to the datum turbofan. As a result of the tabulated weight changes, the maximum takeoff weight for the baseline CRP aircraft increased by $5,000$ lb.

3.2.2 Baseline CRP Aerodynamic Design

The baseline CRP design was guided by data available in the literature [2] regarding an experimental performance study of a model scale CRP $D = 0.56$ m in diameter. Selected configuration characteristics and cruise and takeoff operating condition details are provided in [2] and are summarized in Table 3.7. Advance ratio and thrust coefficient are defined as $J = V_0/(ND)$ and $C_T = T/(\rho_0 N^2 D^4)$, respectively, where V_0 is the flight speed, T is the thrust, and ρ_0 is the free stream density[1].

Table 3.7: Model scale baseline CRP characteristics and operating conditions (extracted from [2])

Model Characteristics	Front	Rear
Diameter D (m)	0.56	0.56
Blade count B (-)	10	8
Hub-to-tip ratio r_{hub}/r_{tip} (-)	0.4	0.4
Sweep φ ($^\circ$)	40	40
rotor-rotor axial spacing x/D_1 (-)	0.224	
Operating Conditions	Cruise	Takeoff
Mach number M_0 (-)	0.78	0.26
Altitude h (m)	$10,670$	Sea level
Rotational speed (rpm)	$6,665$	$6,665$
Advance ratio J (-)	3.90	1.43
Thrust coefficient C_T (-)	1.10	1.17

[1]Throughout this thesis, advance ratio and thrust coefficient are defined using the average shaft speed $N = (N_1 + N_2)$ and average rotor diameter $D = (D_1 + D_2)/2$, where subscripts 1 and 2 denote the front and rear rotor, respectively.

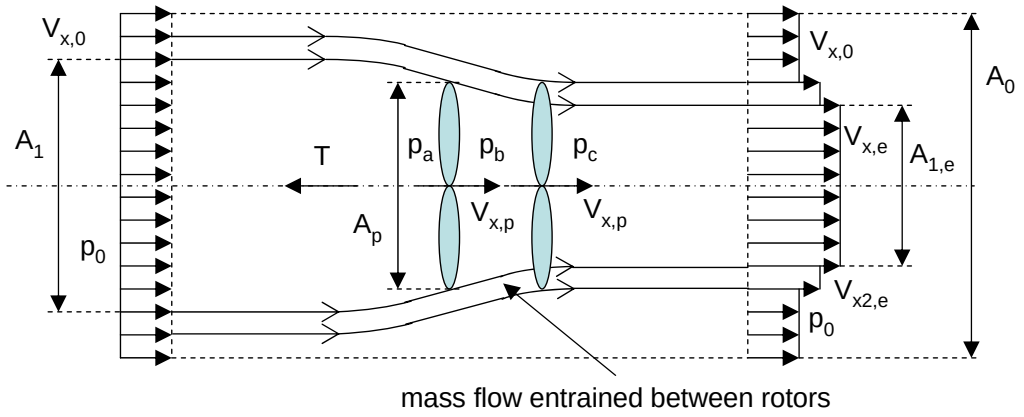

Figure 3-4: Actuator disk and control volume analysis approach

In addition to the tabulated data, the radial distribution of the stagnation pressure ratio $\pi(r) = p_t(r)/p_{t,0}$ across the CRP is presented in [2] for the cruise operating condition. The given stagnation pressure radial distribution served as the starting point of the baseline CRP design. The main objective was to establish a credible CRP geometry while minimizing the exit swirl and matching the given performance data. The design approach steps and main assumptions are described below:

1. Based on the given stagnation pressure ratio $\pi(r)$ and an assumed adiabatic efficiency η_{ad}, the stagnation temperature ratio across the CRP, $\tau(r) = T_t(r)/T_{t,0}$, is computed using the definition of adiabatic efficiency,

$$\eta_{ad} = \frac{\pi^{\frac{\gamma-1}{\gamma}}}{\tau - 1}, \tag{3.1}$$

   where $\gamma = 1.4$ is the ratio of specific heats.

2. The remaining analysis required a control volume approach which is sketched in Figure 3-4. In the approach, the CRP rotors are modeled as simple actuator disks[2]. Assuming that additional mass flow is entrained through the rear rotor,

[2]The actuator disk approach was used to compute the flow velocity across the rotors. Incompressible flow is assumed in this approach. The remaining control volume analysis, however, was carried out assuming compressible flow. Upon completing the model scale baseline CRP design, a steady CFD simulation was carried out. The density change across the two rotors was determined as approximately 3.0 %. Thus, assuming incompressible flow and constant axial velocity across the rotors was appropriate in the current analysis.

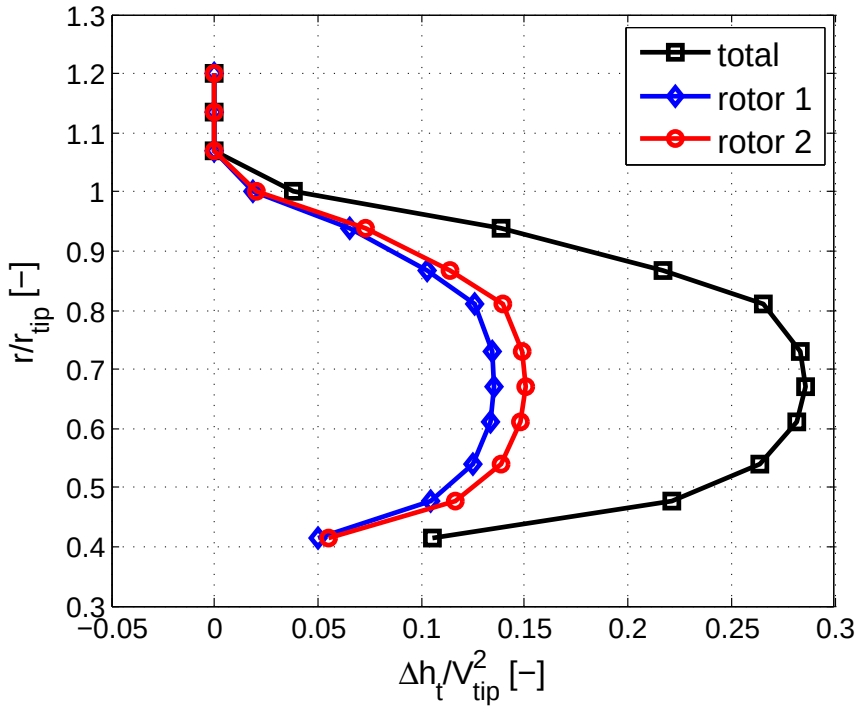

Figure 3-5: Specific work done by each rotor and entire CRP for $\eta_{ad} = 82.5$ % and $\dot{m}_2/\dot{m}_1 = 1.1$

the shaft work split between front and rear rotor, $\Delta h_{t,1}/\Delta h_{t,2}$, was determined based on the known torque split $\Theta = Q_1/Q_2 = 45/55$ and an assumed value for the mass flow ratio $\dot{m}_2/\dot{m}_1$:

$$\frac{\Delta h_{t,1}}{\Delta h_{t,2}} = \frac{c_p\left(T_{t,b} - T_{t,a}\right)}{c_p\left(T_{t,c} - T_{t,b}\right)} = \frac{\dot{m}_2}{\dot{m}_1}\frac{Q_1\left|\omega_1\right|}{Q_2\left|\omega_2\right|} = \frac{\dot{m}_2}{\dot{m}_1}\Theta. \tag{3.2}$$

The specific heat is denoted by c_p, Q is the torque exerted by the rotor, and ω is the angular velocity. The stagnation temperatures upstream of the front rotor, between the rotors, and downstream of the rear rotor are denoted $T_{t,a}$, $T_{t,b}$, and $T_{t,c}$, respectively. The radial distributions of the work done by the front and rear rotor are depicted in Figure 3-5 for an adiabatic efficiency of $\eta_{ad} = 82.5$ % and a mass flow ratio of $\dot{m}_2/\dot{m}_1 = 1.1$. The results reflect the torque split of 45/55 with the loading higher for the rear than for the front rotor.

3. Applying Equations 3.1 and 3.2 to front and rear rotor, the stagnation temper-

ature ratios $\tau_1 =$ and τ_2 and stagnation pressure ratios π_1 and π_2 were obtained.

4. The radial distributions of the tangential velocity V_θ downstream of the front and rear rotor were calculated by applying the Euler turbine equation to each rotor:

$$c_p T_{t,a} (\tau_1 - 1) = \omega_1 \left[(rV_\theta)_b - (rV_\theta)_a \right] \tag{3.3}$$

$$c_p T_{t,a} \tau_1 (\tau_2 - 1) = \omega_2 \left[(rV_\theta)_c - (rV_\theta)_b \right] \tag{3.4}$$

   The radial distribution of the tangential velocity is shown in Figure 3-6 for increasing mass flow ratios $\dot{m}_2/\dot{m}_1$ and an adiabatic efficiency of $\eta_{ad} = 82.5$ %. The residual exit swirl (at station c) was found to be minimized for a mass flow ratio around 1.1.

   Further increasing the assumed value for mass flow ratio leads to increased exit swirl near the tip since free stream mass flow is entrained between the rotors (see Figure 3-4) and leaves the rear rotor with excess swirl as indicated at station c in Figure 3-6.

5. The control volume sketched in Figure 3-4 was used to determine the front- and rear-rotor thrust rotor, T_1 and T_2, assuming inviscid, steady flow with uniform axial inflow. First, the exit Mach number M_e was computed by applying the definition of stagnation pressure,

$$\frac{p_t}{p} = \left(1 + \frac{\gamma - 1}{2} M^2 \right)^{\frac{\gamma}{\gamma - 1}}, \tag{3.5}$$

   up- and downstream of the CRP such that

$$\frac{M_e^2}{M_0^2} = \frac{2}{\gamma - 1} \left[\pi^{\frac{\gamma - 1}{\gamma}} \left(\frac{1}{M_0^2} + \frac{\gamma + 1}{2} \right) - \frac{1}{M_0^2} \right], \tag{3.6}$$

   where the mass-averaged stagnation pressure across the CRP, $\pi = p_{t,e}/p_{t,0} = 1.098$, is known from [2]. Next, the exit static temperature T_e was determined

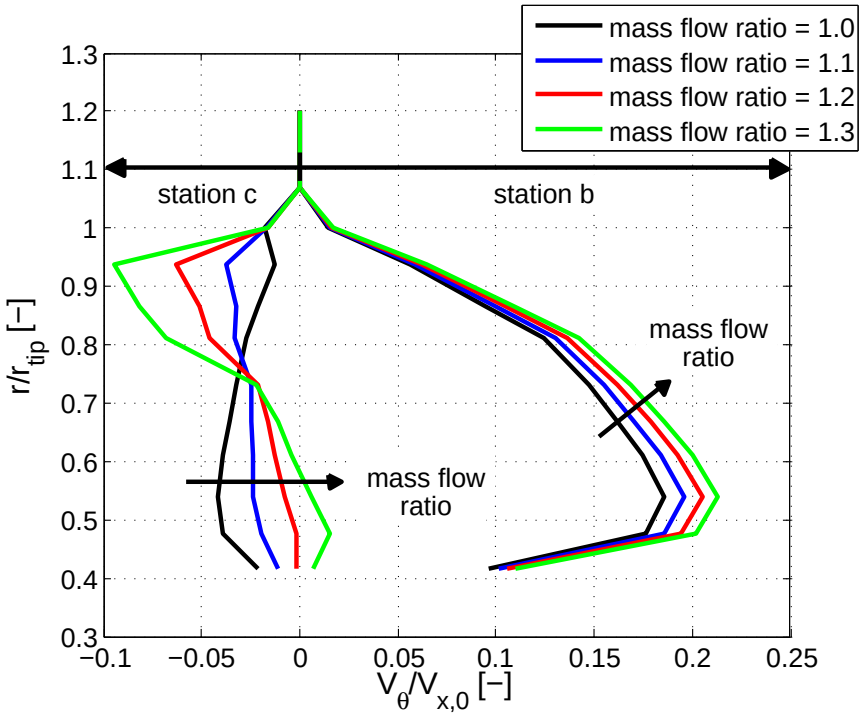

Figure 3-6: Influence of mass flow ratio $\dot{m}_2/\dot{m}_1$ on tangential velocity downstream of front and rear rotor for $\eta_{ad} = 82.5$ %

based on the exit Mach number and the mass-averaged stagnation temperature ratio $\tau = T_{t,e}/T_{t,0}$. With the exit static temperature determined, the exit axial velocity $V_{x,e}$ was computed. From actuator disk theory, the axial velocity at the propfan rotors can be assumed as

$$V_{x,a} = V_{x,b} = V_{x,c} = \frac{V_{x,e} - V_{x,0}}{2}. \tag{3.7}$$

Finally, imposing radial equilibrium,

$$\frac{\partial p\,(r)}{\partial r} = \rho \frac{V_\theta^2\,(r)}{r}, \tag{3.8}$$

the radial distributions of static pressure downstream of the front and rear rotor were determined by integration. With this, the front- and rear-rotor thrust coefficients can be computed.

6. The assumed values for adiabatic efficiency and entrained mass flow were iter-

atively varied until the exit swirl was minimized and the front- and rear-rotor performance agreed with the data in [2]. The combination of an adiabatic efficiency of $\eta_{ad} = 82.5$ % and a mass flow ratio of $\dot{m}_2/\dot{m}_1 = 1.1$ yielded the best agreement and lowest residual exit swirl.

The computed front- and rear-rotor performance is summarized and compared to measured data in Table 3.8. The front- and rear-rotor power coefficients $C_{P,1}$ and $C_{P,2}$ are computed from the measured shaft power and the torque split. For the operating condition analyzed, the calculated thrust results compare well with the measured performance.

Table 3.8: Model scale baseline CRP cruise performance for $\eta_{ad} = 82.5$ % and $\dot{m}_2/\dot{m}_1 = 1.1$

	Calculated	Measured (from [2])	Rel. Error
Front rotor thrust coefficient at $C_{P,1} = 2.32$	0.47	0.48	-2.1 %
Rear rotor thrust coefficient at $C_{P,2} = 2.61$	0.63	0.62	1.6 %

7. The blade coordinates were defined based on a velocity triangle analysis and the axial chord distribution and the stacking line location extracted from [2]. Circular arc camber lines and a NACA 65A008 thickness distribution were assumed for the blade profiles. Finally, the detailed aerodynamic design and performance investigation was carried out using the single and dual rotor vortex-lattice methods in RVL/RAXAN. However, the vortex-lattice approach does not include compressibility effects. Therefore, the analysis was performed at the takeoff condition defined in Table 3.7. The detailed aerodynamic design was finalized by varying the blade angle settings and comparing the global performance with the measurements as summarized in Table 3.9.

   For a blade setting angle of $\beta_{1,TO} = \beta_{2,TO} = 46.5°$, the power coefficient is $C_{P,TO} = 2.75$, in good agreement with the data reported in [2]. The detailed blade geometry of the final CRP design differs from the model CRP given in [2] and the takeoff performance is improved by $\Delta\eta_{prop,TO} = 6$ %. The designed

Table 3.9: Computed model scale takeoff performance compared to data from literature [2]

	Calculated	Measured (from [2])
$C_{P,TO}$	2.79	2.78
$C_{T,TO}$	1.31	1.19
$\eta_{prop,TO}$	67.1	61.1

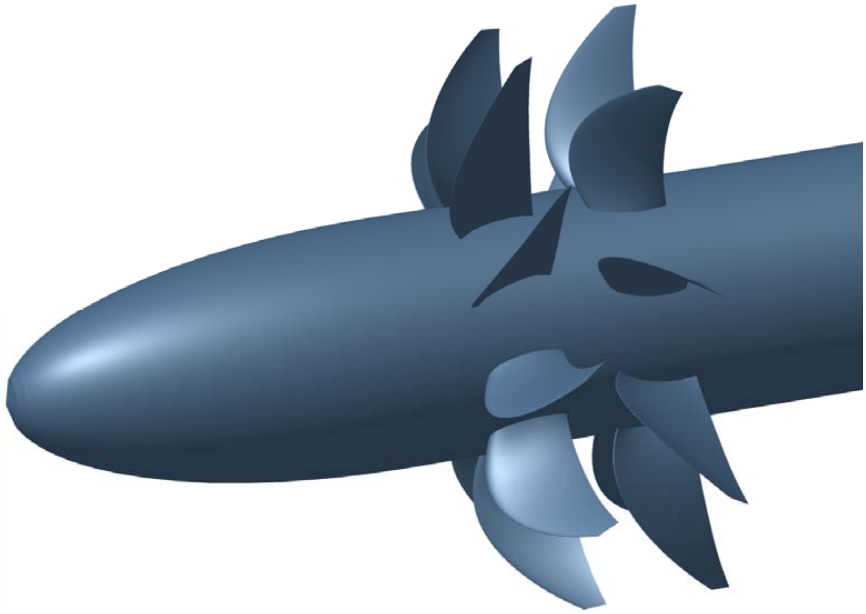

Figure 3-7: Baseline CRP design

baseline CRP is illustrated in Figure 3-7. The hub geometry is extracted from the literature [2].

The model scale CRP design was sized to full scale at the takeoff condition. It was also ensured that the thrust requirement at top-of-climb can be met. From the FLOPS mission analysis for the baseline CRP aircraft (including the weight adjustments described in the previous section), the takeoff thrust requirement was determined as $T_{TO} = 20,500$ lb. The full scale baseline CRP tip diameter was obtained by maintaining tip Mach number and thrust coefficient:

$$M_{tip,TO} = \left(\frac{V_{tip}}{c}\right)_{TO} = 0.574 = const. \tag{3.9}$$

$$C_{T,TO} = \left(\frac{T}{\rho N^2 D^4} \right)_{TO} = 1.31 = const. \tag{3.10}$$

In Equation 3.9, c denotes the speed of sound. Equations 3.9 and 3.10 were solved for the rotational speed and rotor diameter while constraining the full scale CRP to equal tip speeds and diameters as in the model scale design. The resulting full scale baseline CRP characteristics and operating conditions at takeoff are summarized in Table 3.10.

Table 3.10: Full scale baseline CRP characteristics and takeoff operating condition details

Model Characteristics	Front	Rear
Diameter D (m)	3.81	3.81
Blade count B (-)	10	8
Hub-to-tip ratio r_{hub}/r_{tip} (-)	0.4	0.4
Sweep φ (°)	40	40
rotor-rotor axial spacing x/D_1 (-)	0.224	
Operating Conditions	**Takeoff**	
Mach number M_0 (-)	0.26	
Altitude h (m)	Sea level	
Rotational speed (rpm)	934	
Advance ratio J (-)	1.43	
Thrust coefficient C_T (-)	1.31	

3.2.3 Baseline CRP Engine

The baseline CRP gas turbine cycle is based on the datum turbofan. The low-pressure turbine drives the propfan rotors through a gearbox a with gear ratio of $8:1$, similar to the gearbox featured in the 1989 PW/HS/Allison 578-DX propfan propulsion system (gear ratio $8.3:1$) [47].

The selected gear ratio resulted in a high speed low-pressure spool with $N_{LP,CRP} = 7,872$ rpm. The datum turbofan low-pressure spool operates at $N_{LP,fan} = 3,800$ rpm, therefore the size of the engine core needed to be reduced for the baseline CRP configuration.

The full scale CRP power requirement was computed in RVL/RAXAN as $P_{CRP} =$

12.1 MW. The datum turbofan power requirement determined in GasTurb was slightly higher at $P_{fan} = 13.0$ MW. For the CRP engine layout, a two-spool turboshaft engine with LPC was selected. The required CRP core mass flow was determined from the low-pressure spool power balance.

Assuming an LPT stage loading of $\Psi_{LPT,CRP} = 2.0$ and adding an additional stage compared to the turbofan engine core layout to alleviate the relatively high turbine blade loading, the mean LPT radius for the CRP engine core was re-sized to $r_{m,LPT,CRP} = 0.204$ m, a 55 % reduction compared to the datum turbofan LPT radius. Similarly, the mean LPC radius for the CRP engine was determined assuming an LPC stage loading of $\Psi_{LPC,CRP} = 0.3$ as $r_{m,LPC,CRP} = 0.268$ m, a 45 % reduction relative to the datum turbofan LPC radius.

The high-pressure component design and the engine cycle parameters such as component efficiencies, pressure ratios, and stagnation temperatures were not changed compared to the datum turbofan engine core. The CRP engine cycle was closed for the cruise design point condition using GasTurb. At the cutback and approach off-design conditions, a reduction of the low-pressure spool speed was required to match the reduced CRP shaft power requirements.

To summarize, based on the airframe of the datum turbofan powered aircraft, a baseline CRP aircraft in aft fuselage pylon mounted pusher configuration was developed. The new aircraft arrangement includes modifications to the baseline airframe due to the integration of the CRP engines. The CRP rotors were designed based on model data given in the literature and the CRP engine core was re-sized based on the datum turbofan core characteristics.

Chapter 4

CRP Noise Estimation Methodology

In order to assess the acoustic performance of CRP powered aircraft arrangements, a CRP noise estimation method is developed in this chapter. The method is integrated in the noise module of the overall performance assessment framework shown in Figure 2-1.

The main focus of this work is on the estimation of CRP interaction tone noise. In order to accurately determine CRP interaction noise, the aerodynamic interference between the CRP rotors needs to be determined using a high-fidelity approach because inaccuracies in capturing the underlying source mechanisms directly influence the fidelity of the computed noise levels. The underlying mechanisms, which are hypothesized to be responsible for CRP interaction noise, are outlined first.

A frequency domain approach is chosen based on Hanson's single rotor noise method. The approach allows the quantitative dissection of the CRP noise mechanisms and the implementation of advanced source mitigation concepts. 3-D unsteady RANS computations are demonstrated to successfully capture the underlying mechanisms and determine the time-varying blade surface pressures necessary for the definition of the acoustic source terms. The CRP noise estimation approach and the derivation of the working equations are presented in the second and third parts of this Chapter, respectively.

Finally, the established CRP noise method is executed for the model scale baseline CRP defined in the previous chapter. The computed noise results are compared to acoustic measurement data available for the baseline CRP configurations. The exact blade profile details of the baseline CRP differ from the model CRP used in the experiments. However, the geometric details are not thought to significantly influence the noise generation and the comparison between computed and measured noise shows good agreement, thereby validating the developed CRP noise estimation method.

4.1 Interaction Tone Noise Source Mechanisms

It is assumed here, that the aerodynamic mechanisms producing CRP interaction noise can be attributed to the following effects:

1. Pressure fields due to rear-rotor upstream influence interacting with the front rotor.

2. Tip-vortices shed from the front rotor affecting the rear-rotor blade loading.

3. Front-rotor wakes interfering with the rear rotor.

4. Front-rotor hub wakes and hub boundary layer influencing the rear-rotor hub loading.

Each of the above mechanisms introduces unsteadiness in the rotor blade loading which in turn affects CRP interaction noise. To illustrate the aerodynamic features responsible for the CRP noise mechanisms, results from a full-wheel 3-D RANS calculation for the baseline CRP configuration at the takeoff condition ($M = 0.25$) are briefly outlined first. The takeoff operating point is simulated because it is the condition relevant for FAR 36 noise measurements. A detailed discussion of the noise assessment at the FAR 36 certification locations is found in Chapter 6.

The rear-rotor potential field directly influences the front-rotor loading. The flow field around the CRP blades for a radial cut at mid-span is shown in Figure 4-1. The

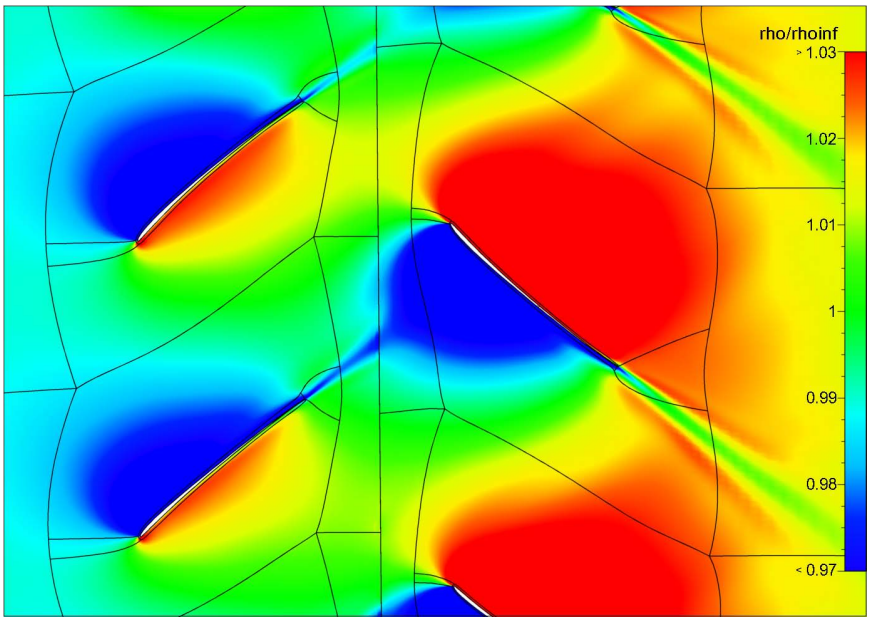

Figure 4-1: Baseline CRP density distribution at mid-span

baseline CRP is operated at equal tip speeds such that a front-rotor blade interacts $2B_2 = 16$ times with the potential field of a rear-rotor blade during one revolution.

The second noise source mechanism investigated is the interaction of the front-rotor tip-vortices, represented as low density regions in Figure 4-2. The vortex system is shown in Figure 4-3 highlighting the helical motion and convection of the tip-vortices through the interface between the front- and rear-rotor reference frames and interacting with the rear rotor.

The interaction of the front-rotor wakes and the hub wake and endwall boundary layer with the rear rotor represent the third and fourth noise source mechanisms, respectively. The viscous wakes are depicted in Figure 4-4 near the hub at 10 % span. Similar to the tip-vortex noise source mechanism, a rear-rotor blade interferes $2B_1 = 20$ times with the front-rotor tip-vortices and viscous wakes during one rotor revolution. The thin secondary wake preceding the blade wake observed in Figure 4-4 is due the flow separation and reattachment on the blade suction surface near the leading edge of the highly-cambered hub profile.

In order to accurately estimate CRP interaction noise, a careful numerical study is required to ensure that all of the above aerodynamic source mechanisms are ade-

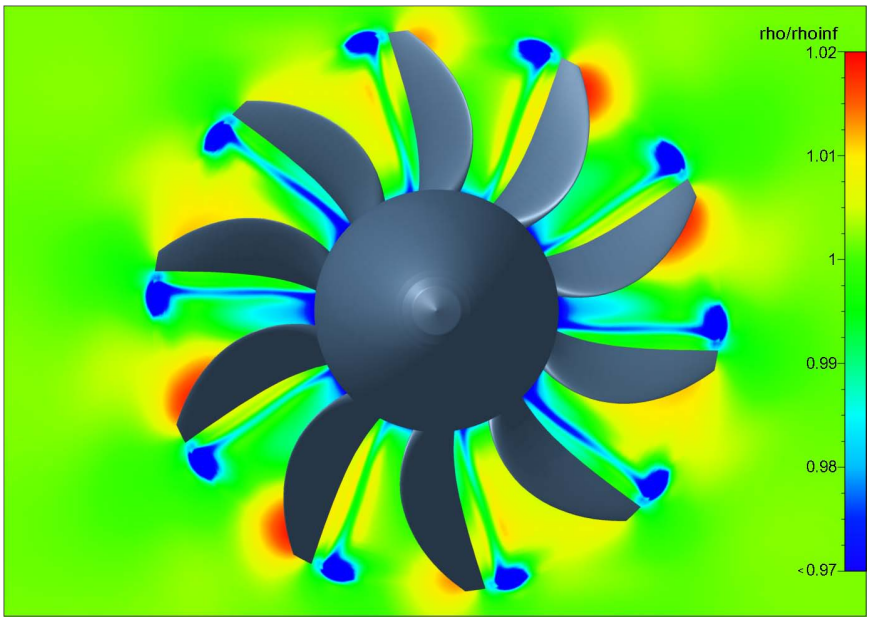

Figure 4-2: Baseline CRP density distribution at $x/D_1 = 0.12$

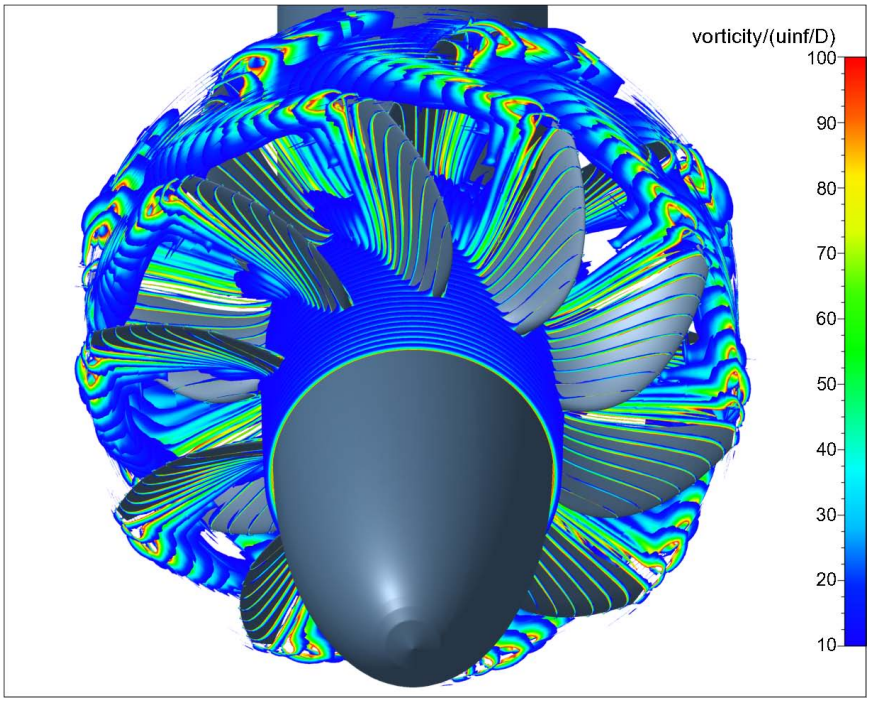

Figure 4-3: Baseline CRP blade-tip vortex system: front-rotor tip-vortices interact with rear rotor

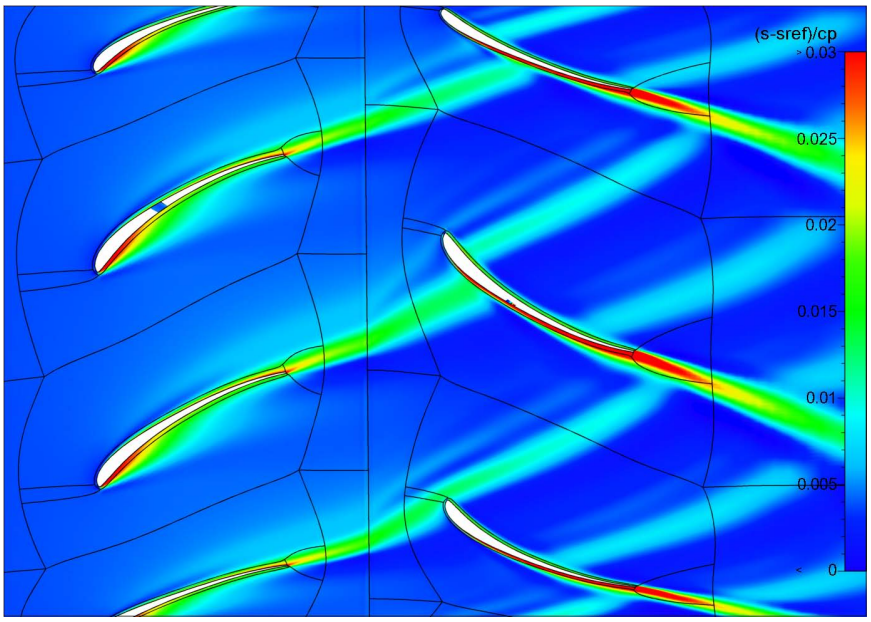

Figure 4-4: Baseline CRP entropy distribution near hub (10 % span)

quately captured. To this end, detailed grid and time step convergence studies are conducted and the results are presented in Chapter 4.4.

4.2 CRP Noise Estimation Method

In addition to the requirement of accurately capturing the CRP noise source mechanisms, the following criteria constitute the basis for the selection of the CRP noise estimation approach pursued in this work.

The first objective of this research is to investigate the relative importance of the underlying mechanisms on CRP interaction tone noise. The CRP noise method is thus required to be capable of dissecting the source mechanisms and the computed CRP noise levels need to be subdivided into contributions from separate sources.

The second objective of this work is to explore necessary design features and CRP noise reduction technologies. Therefore, reasonable computation times are required such that parametric studies of CRP configuration characteristics (e.g. rotor diameter, axial rotor-rotor spacing, blade count) and operating conditions (e.g. rotor tip speed, blade angle setting) are feasible.

The third objective is to quantify CRP noise and noise variations between different CRP configurations on a consistent aircraft mission basis. To this end, CRP noise computations at the FAR 36 observer locations are needed which requires noise results along the aircraft takeoff and approach trajectories. Thus, the CRP noise method needs to be capable of dealing with varying observer positions and flight and operating conditions at low computation times.

Finally, in order to compute CRP noise on the CRP engine/aircraft system level, the noise method needs to be capable of accounting for non-uniform inflow due to non-zero angle-of-attack and/or the presence of an upstream pylon.

4.2.1 Outline of Approach

Propfan noise estimation methods developed in the past include approaches in the time [48] and frequency domain [6]. Recent advances in computational aerodynamics and aeroacoustics have led to hybrid methods based on coupling CFD and CAA [10] [11] [12]. However, in general, CAA approaches are expensive in computational time and memory requirements due to the high grid densities needed to adequately resolve the acoustic pressure disturbances. Therefore, CAA methods are generally not yet viable for parametric studies in the propfan design phase.

In the light of the requirements for the CRP noise method described above and the high computational costs of CAA methods, a frequency domain approach for CRP noise was pursued in the present work based on extending Hanson's single rotor noise method [6] to counter-rotating configurations. The foundation of this approach is Goldstein's formulation of the acoustic analogy for moving media [49]. The acoustic interference between the rotors is captured as long as the aerodynamic interaction is captured accurately. One of the main advantages of this approach is the low computation time requirement allowing the method to be used for detailed parametric studies.

Compliant with the specifications above, the method can be used to dissect and quantify the effects of the different mechanisms responsible for CRP interaction noise and is capable of dealing with CRP noise reduction technologies. In addition, non-

uniform inflow effects due to angle-of-attack or an upstream pylon can be accounted for.

The theory requires the a priori determination of the unsteady blade surface pressures to compute the acoustic source terms. A high-fidelity full-wheel 3-D RANS approach capable of accurately capturing the noise source mechanisms is therefore developed and used to generate the required surface pressure data.

4.3 Development Method

The CRP noise estimation method developed in this chapter is based on Goldstein's formulation of the acoustic analogy [49] and Hanson's frequency domain method for single rotor noise [6].

Thickness and loading noise sources are implemented in the CRP noise estimation method. For thin blades, significant quadrupole noise radiation is a strictly transonic phenomenon as for example reported by Hanson et al. [50]. The CRP blade designs investigated in this work are highly swept and relative tip Mach numbers are below the critical value of 0.85 at the low speed conditions considered here for noise assessment. Therefore, quadrupole sources are currently not accounted for but can be included in the methodology for future cruise noise calculations.

A brief description of the equations governing single-rotating propfan noise is presented first. The derivation of the working equations is given next. Finally, the modifications required to extend the SRP noise equations to CRP configurations are discussed in detail.

4.3.1 Governing Equations for Single Rotor Noise

The Ffowcs-Williams and Hawkings acoustic analogy formulation generalized for a moving medium can be written as

$$p'(\mathbf{x},t) = -\int_{-T}^{T}\int_{A(\tau)} \rho_0 V_N \frac{DG}{D\tau} dA(\mathbf{y})\, d\tau + \int_{-T}^{T}\int_{A(\tau)} F_i \frac{\partial G}{\partial \tau} dA(\mathbf{y})\, d\tau, \qquad (4.1)$$

where $p'(\mathbf{x}, t)$ is the acoustic pressure at observer location $\mathbf{x} = (x, y, z)^T$ and time t.

The thickness noise source is described by the first term in Equation 4.1. V_N denotes the normal surface velocity and $V_N dA d\tau$ is the volume displaced by the surface element dA in the time increment $d\tau$. G is a Green's function and $D/D\tau$ is the convective derivative. The loading noise source is given by the second term in Equation 4.1 where $F = (F_r, F_\Phi, F_x)^T$ and $F_i dA$ denotes the force on the blade surface element dA in direction i.

As described in [50], thickness and loading noise can be calculated independently such that

$$p'(\mathbf{x}, t) = p'_T(\mathbf{x}, t) + p'_L(\mathbf{x}, t), \tag{4.2}$$

where $p'_T(\mathbf{x}, t)$ and $p'_L(\mathbf{x}, t)$ denote the acoustic pressure disturbances at observer location $\mathbf{x}$ and time t due to thickness and loading noise sources, respectively. From Equation 4.1, the thickness noise is therefore given by

$$p'_T(\mathbf{x}, t) = -\int_{-T}^{T} \int_{A(\tau)} \rho_0 V_N \frac{DG}{D\tau} dA(\mathbf{y})\, d\tau. \tag{4.3}$$

Representing the time signal $p'_T(\mathbf{x}, t)$ as a Fourier series, the single rotor thickness noise harmonic P_{Tm} for blade passing frequency harmonic m at observer location $\mathbf{x}$ can be expressed as

$$P_{Tm}(\mathbf{x}) = \gamma B \int_A e^{-imB\phi_S} \frac{1}{2\pi} \int_0^{2\pi} M_N \left(M \frac{\partial G}{\partial x_0} - ik_m G_m \right) e^{-imB\phi_0} d\phi_0 dA, \tag{4.4}$$

where $M_N = V_N/c_0$ is the Mach number normal to the blade surface, $k_m = mBM_{tip}$ is the wavenumber, and $M_{tip} = \omega r_{tip}/c_0$ is the tip Mach number. B denotes the number of blades. The axial and tangential source coordinates are given by x_0 and ϕ_S, respectively and the Green's function is

$$G_m = \frac{e^{ik_m\sigma}}{4\pi S}, \tag{4.5}$$

with the phase radius σ given by

$$\sigma = \frac{M\left(x - x_0\right) + S}{1 - M^2}, \tag{4.6}$$

and the amplitude radius S written as

$$S = \sqrt{\left(x - x_0\right)^2 + \left(1 - M^2\right)\left(\left(y - y_0\right)^2 + \left(z - z_0\right)^2\right)}. \tag{4.7}$$

Analogous to the thickness noise calculation, the single rotor loading noise harmonic P_{Lm} can be written as

$$P_{Lm}\left(\mathbf{x}\right) = B\int_A e^{-imB\phi_S}\frac{1}{2\pi}\int_0^{2\pi} F_i\left(\phi_0 - \phi_S\right)\frac{\partial G_m}{\partial y_i}e^{-imB\phi_0}d\phi_0 dA, \tag{4.8}$$

where the elements of the blade loading $F_i dA$ are computed using 3-D unsteady RANS simulations and the Green's function derivatives are calculated analytically.

Equations 4.4 and 4.8 represent thickness and loading noise harmonics as continuous integrals over the blade surface area. To calculate the noise harmonics, blade geometry and surface pressure data are required from a CFD simulation and are thus provided in 3-D grid format. Practical applications of equations 4.4 and 4.8 therefore involve dividing the blade surface area into discrete elements in the radial and chordwise directions.

The radial and chordwise indices are denoted here by μ and ν, respectively. The discretization of the area integrals is therefore represented by $\int_A dA \rightarrow \sum_{\mu,\nu}$. The fundamental thickness noise source element is $M_N dA$. In discrete form, this thickness source element is defined as

$$V_{\mu,\nu} = \left(M_N \Delta A\right)_{\mu,\nu}. \tag{4.9}$$

The discretized form of the thickness noise harmonic can now be written as

$$P_{Tm}\left(\mathbf{x}\right) = \gamma B\sum_{\mu,\nu} e^{-imB\phi_S}\frac{1}{2\pi}\int_0^{2\pi} V_{\mu,\nu}\left(M\frac{\partial G}{\partial x_0} - ik_m G_m\right)e^{-imB\phi_0}d\phi_0. \tag{4.10}$$

Similarly, the fundamental loading source element in Equation 4.8 is $F_i dA$. The discretized form of $F_i dA$ is defined as

$$F_{i,\mu,\nu} = \left(F_i \Delta A\right)_{\mu,\nu}. \tag{4.11}$$

The discretized form of the loading noise harmonic can thus be represented as

$$P_{Lm}\left(\mathbf{x}\right) = B \sum_{\mu,\nu} e^{-imB\phi_S} \frac{1}{2\pi} \int_0^{2\pi} F_{i,\mu,\nu}\left(\phi_0 - \phi_S\right) \frac{\partial G_m}{\partial y_i} e^{-imB\phi_0} d\phi_0. \tag{4.12}$$

The formulations in Equations 4.10 and 4.12 are the working forms for SRP noise estimation that were coded in Matlab along with the thickness and loading source term calculations from the CFD data. This version of the noise code did not include any modifications to Hanson's theory. The code was verified using a test case of a 6-bladed SRP 13 ft in diameter at cruise which is provided by Hanson [6]. The working equations 4.10 and 4.12 are the basis from which the theory is extended for CRP configurations. The necessary modifications are described next.

4.3.2 Extension to Counter-Rotating Configurations

As outlined in Section 1.1, it is assumed in this work that the mechanisms responsible for CRP interaction noise can be categorized into rear-rotor upstream influence interacting with the front rotor, front-rotor tip-vortices affecting the rear-rotor loading, front-rotor viscous wakes interfering with the rear rotor, and front-rotor hub wake and hub boundary layer influencing the rear-rotor hub loading. The unsteady interaction of the two rotors due to wake, tip-vortex and potential field effects is captured in the aerodynamic calculations and reflected in the unsteady characteristics of the blade surface pressures. Therefore, since the acoustic analogy requires the coupled aerodynamic data, the acoustic interaction is inherently accounted for by carefully superposing the noise fields from the two rotors as proposed by Hanson [9].

Thickness noise is produced at multiples of the blade passing frequency only such

that the harmonic order m takes on all integer values from 1 to $+\infty$. In order to account for the interaction tones caused by unsteady blade loading, the formulation for single rotor loading noise in Equation 4.8 needs to be modified. For the general case of unequal tip speeds and blade counts, the observer will perceive frequencies

$$f = nBPF_1 + k\left(BPF_2 - BPF_1\right), \tag{4.13}$$

where $n = 1, 2, \ldots, \infty, k = 0, 1, \ldots, n$, and $BPF_{1,2} = B_{1,2}N_{1,2}$ denotes the blade passing frequency of the respective rotor. The value of the sound harmonic m in Equation 4.8 is changed to $m' = f/BPF$, where $BPF = BPF_1$ or $BPF = BPF_2$, depending on which rotor loading noise is computed. Additionally, in contrast to the single rotor case, in which each blade experiences identical loading changes and thus generates identical noise signals, it is important to note that in the general case of unequal tip speeds and blade counts, or in the presence of an upstream pylon or angle-of-attack effects, the individual rotor blades do not necessarily emit identical noise signals. Thus, instead of simply multiplying the source term by the blade number B in Equation 4.8, the noise signals from each blade b have to be added up while taking into account the phase lags due to the blade position. Implementing these modifications, Equation 4.8 becomes

$$P_{Lm,CRP}\left(\mathbf{x}\right) = \sum_{b=1}^{B} e^{-im'B\phi_{ref}(b)} \int_A e^{-im'B\phi_S} \frac{1}{2\pi} \int_0^{2\pi} F_{b,i} \frac{\partial G_{m'}}{\partial y_i} e^{-im'B\phi_0} d\phi_0 dA, \tag{4.14}$$

where the reference angle accounting for the blade position is given by

$$\phi_{ref}\left(b\right) = \left(b-1\right)\frac{2\pi}{B}. \tag{4.15}$$

In Equation 4.14, $F_{b,i}$ denotes the force per unit area on the surface of blade b in direction i (radial, tangential, axial). The discretized loading source term $F_{b,i,\mu,\nu}$ is determined from the a priori external aerodynamic analysis for every radial and chordwise blade surface area element μ, ν. The discretized formulation of the har-

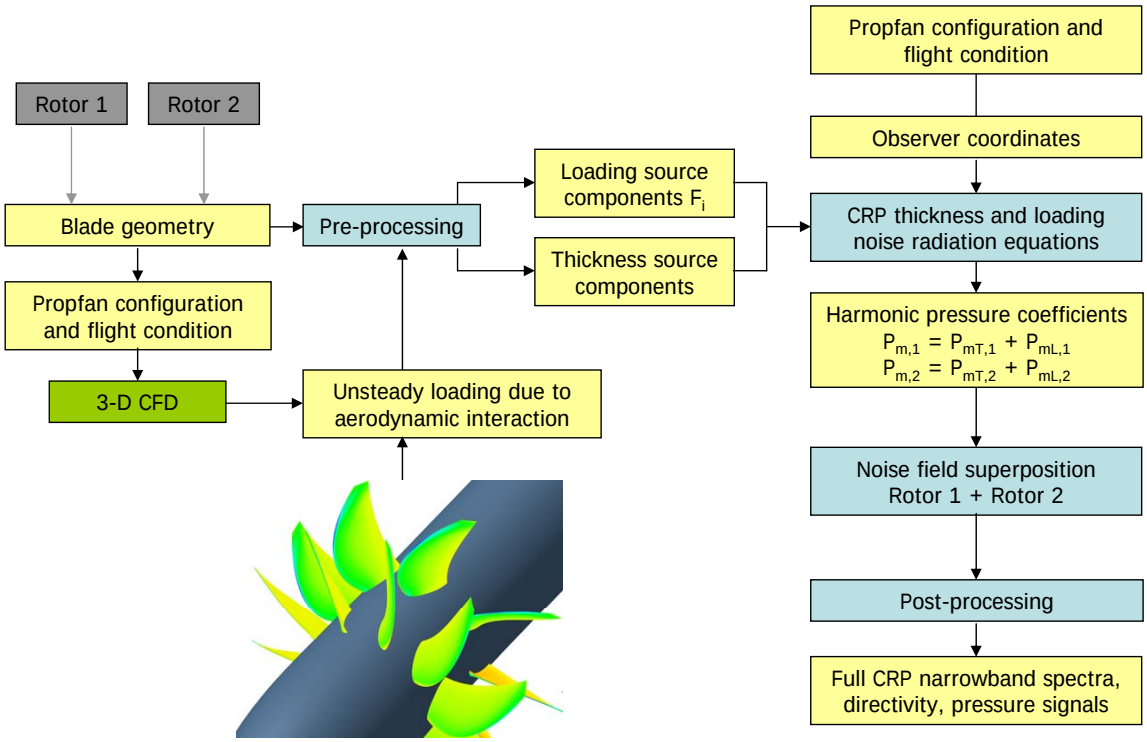

Figure 4-5: CRP noise estimation methodology

monic loading noise estimation for counter-rotating propfans becomes

$$P_{Lm,CRP}(\mathbf{x}) = \sum_{b=1}^{B} e^{-im'B\phi_{ref}(b)} \sum_{\mu,\nu} e^{-im'B\phi_S} \frac{1}{2\pi} \int_0^{2\pi} F_{b,i,\mu,\nu} \frac{\partial G_{m'}}{\partial y_i} e^{-im'B\phi_0} d\phi_0. \quad (4.16)$$

To summarize, a conceptual outline of the established CRP noise estimation method is depicted in Figure 4-5. Required inputs are the blade geometries of the two rotors, the CRP configuration details (such as for example rotor-rotor axial spacing), the operating conditions, and the observer coordinates relative to the CRP. Using the unsteady blade loading data calculated externally (for example 3-D CFD), the thickness and loading source components are computed. In order to obtain the full CRP noise spectrum, the working formulations for thickness and loading noise in Equations 4.10 and 4.16 are evaluated separately for each rotor. The noise fields are then superposed to determine the CRP narrowband spectrum or acoustic pressure signals.

The working formulation for the CRP harmonic loading noise was implemented in Matlab to extend the SRP noise code based on Hanson's theory to CRP configurations. The resulting CRP noise method is modular such that thickness and loading noise results can easily be separated to assess the relative importance of monopole and dipole sources. In addition, the approach derived above allows to compute the source terms in predefined radial or chordwise ranges. For example, in order to quantify the CRP interaction noise impact of front-rotor tip-vortices interfering with the rear-rotor blade tips, the loading noise can be computed by integrating over the dipole sources in a limited radial range near the rear-rotor tip region only. This approach is pursued in dissecting the CRP noise mechanisms and the results are discussed in Chapter 5. A user manual providing detailed explanations of the Matlab code developed for the CRP noise estimation is given in Appendix B.

4.4 Aerodynamic Analysis

In order to capture the aerodynamic interaction between the two rotors and to obtain the time varying blade pressures, a high-fidelity approach involving 3-D RANS simulations in Numeca FINE/Turbo was developed.

As the acoustic equations derived above are exact, the level of accuracy of the computed noise results is governed by the fidelity of the aerodynamic analysis providing the unsteady blade loading. It is therefore important to ensure that the mechanisms responsible for CRP noise are accurately captured and resolved in the aerodynamic computations.

The meshing strategy and challenges encountered in the grid generation are described first. Next, the computational setup is outlined including the discussion of steady results used to initialize the unsteady computations. In the case of the unsteady calculations, careful grid and time step sensitivity studies were carried out and in the final part of this section a set of general guidelines for the numerical setup is given.

The blade surface pressure data obtained from the CFD calculations is Fourier

transformed to determine the loading harmonics required as inputs to the CRP noise estimation method. In the absence of angular inflow or upstream pylon effects, the rear-rotor upstream influence causes the loading on the front rotor to vary at frequencies

$$f_{load,1} = kBPF_1 \left(1 + \frac{N_2}{N_1}\right), \tag{4.17}$$

where the loading harmonic $k = 0, 1, 2, \ldots, \infty$. Similarly, the front-rotor viscous wakes and tip-vortices lead to rear-rotor unsteady loading effects at frequencies

$$f_{load,2} = kBPF_2 \left(1 + \frac{N_1}{N_2}\right). \tag{4.18}$$

With the above, the loading waveform is reconstructed as part of the pre-processing in the CRP noise method to determine the loading source components $F_{b,i}$ in the CRP loading noise calculation described in Equation 4.14.

4.4.1 CFD Tool Description

All 3-D RANS simulations were carried out using the commercially available software package Numeca FINE/Turbo. FINE/Turbo includes tools for grid generation, flow solving, and post-processing and is tailored originally tailored for internal flow turbomachinery applications. During the course of this work, a meshing strategy for open rotor designs including counter-rotating configurations was developed based on FINE/Turbo's approach for internal flow simulations.

The grid generation Autogrid and IGG enable the automated generation of CRP grids. Meshes required for parametric studies including variations in blade count, blade angle setting, or rotor-rotor axial spacing can be generated with little user input. The flow solver Euranus is controlled in the graphical user interace FINE. Euranus supports parallel computation on multiple processors and takes advantage of the multigrid technique. Multiple sweeps between a fine mesh and coarsened grid levels are performed within each iteration to reduce low frequency errors on coarse grid levels and to accelerate convergence [51]. The flow solutions are processed in the

post-processing tool, CFView, using a graphical user interface or automated Python scripts, or in the external post-processing tool Tecplot 360. A more detailed description of FINE/Turbo can be found in [26].

To the author's knowledge, FINE/Turbo was applied to CRP configurations for the first time during this research project which led to several challenges in the grid generation and computational setup. Different grid topologies were investigated to evaluate the resolution of the underlying CRP flow features. The two main grid strategies are discussed next.

4.4.2 CRP Grid Generation

Multi-block structured hexahedral grids were used for the CRPs analyzed in this work. To accurately resolve the front-rotor viscous wakes and tip-vortices, the meshes between the two rotors and around the blade tips were generated with particular care.

Two meshing strategies were investigated. The first topology, denoted in the following as grid 1, is depicted in Figure 4-6. The overall mesh consists of three regions. The flow in the inlet and rotor 1 domains (regions I and II) is computed in the front-rotor frame of reference. The flow in the rotor 2 domain (region III) is computed in the rear-rotor reference frame. In radial direction, the overall domain is subdivided into three layers: (1) the rotor passage including the grid around the rotor blades, (2) the far field region with reduced grid density, and (3) a sub-domain connecting the rotor passage and far field regions which are of distinct topologies. Non-matching patch boundaries were applied at the radial sub-domains. These boundaries require interpolation routines which are defined prior to a simulation.

As described in Section 4.4.5, it was found that non-matching boundaries can lead to discontinuous flow solutions resulting in inadequate tip-vortex resolution. In the light of these findings, the mesh was improved by extending the blade grid topology all the way to the far field boundary to assure a continuous grid structure and to eliminate all non-matching block patches at the interface between the rotor passage and far field sub-domains. The topology of the improved grid, denoted in the following as grid 2, is presented in Figure 4-7.

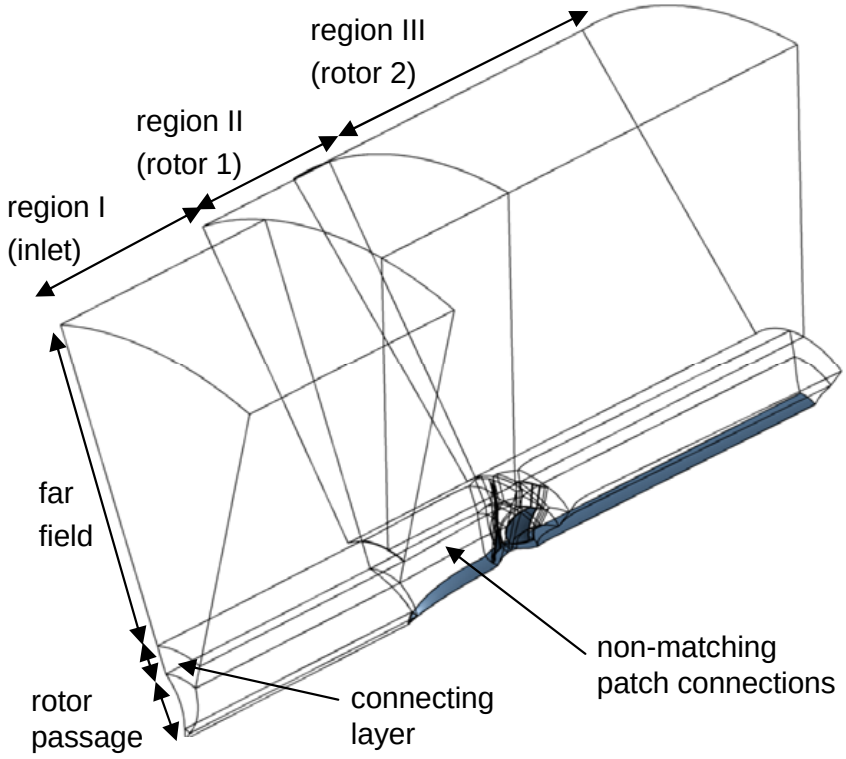

Figure 4-6: Grid 1: Original baseline CRP grid-block topology

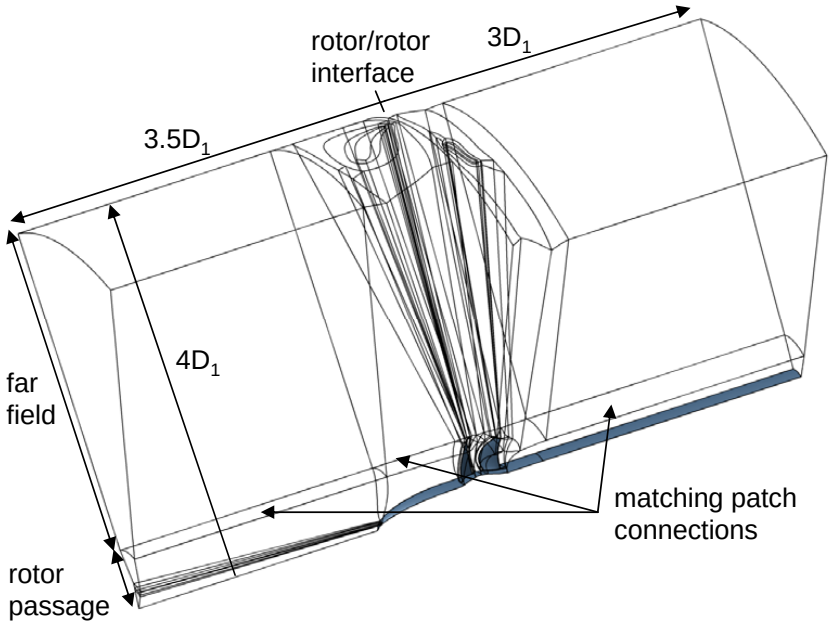

Figure 4-7: Grid 2: Improved baseline CRP grid-block topology

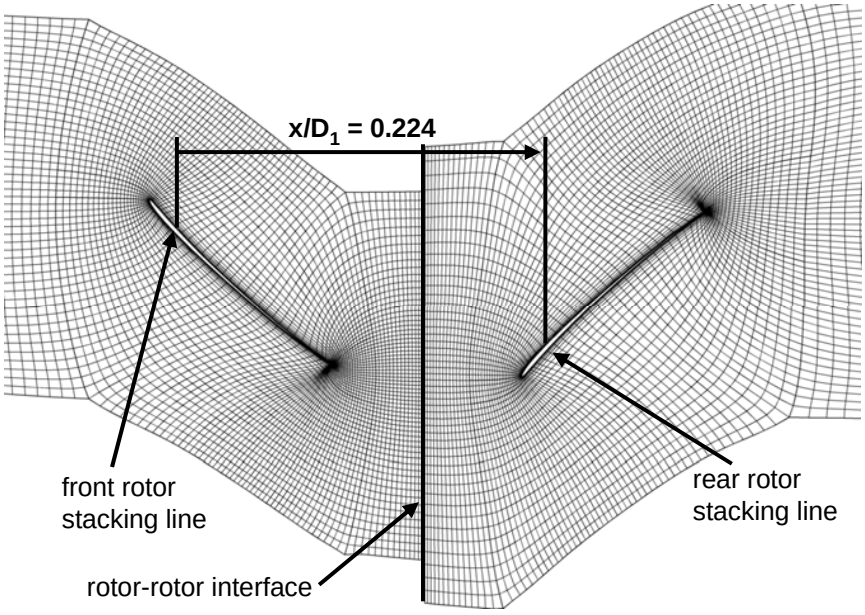

Figure 4-8: Grid 2: Close-up of rotor meshes at mid-span

At the interface between the two rotor relative frames, the radial node distribution is continuous for both grid 1 and grid 2. The governing equations are solved in the relative frame leading to high relative Mach numbers near the far field radial boundary. This in turn can induce excessive artificial dissipation leading to non-physical rotational flow in the far field regions. To avoid this, the far field radial boundary was located at $4D_1$, far enough from the CRP domain to avoid interference with the capture streamtubes.

The rotor meshes at mid-span are shown for the improved grid topology in Figure 4-8. The characteristics of grids 1 and 2 are summarized in Table 4.1. Based on the grid 2 topology, all of the unsteady simulations used to obtain the time-dependent blade loading for the CRP noise calculations were carried out in full-wheel configuration featuring 16.5 million cells for the baseline CRP.

4.4.3 Computational Procedure

The first step towards determining the time-dependent pressure data involves setting up and carrying out steady computations in order to initialize the unsteady simulations and obtain aerodynamic performance results. The second step is to compute

Table 4.1: Characteristics of meshes used in grid convergence study

	Grid 1	**Grid 2**
Topology (see Figures 4-6 and 4-7)	original topology	improved topology
Grid structure in patches between radial sub-domains	non matching	continuous
Radial grid points per rotor passage	34	71
Grid points in pitchwise direction across passage	90	85
Grid points on blade suction and pressure surface	121	121
Full-wheel cell count	10.5 million	16.5 million

the surface pressures using full-wheel unsteady simulations.

Steady single-passage RANS simulations solving the viscous Reynolds Averaged Navier-Stokes equations were performed first to determine grid convergence based on stagnation pressure and blade surface pressure results.

The governing equations include an apparent stress term due to the fluctuating velocity field, generally referred to as Reynolds stress. The Spalart-Allmaras turbulence model was applied in all simulations to approximate the Reynolds stress terms.

In the case of the steady simulations used to initialize the unsteady computations, a full non matching mixing plane was defined to transmit information at the interface between the front- and rear-rotor reference frames. The mixing plane formulation is a standard approach utilized in the computational analysis of turbomachinery applications. The details of the mixing plane approach are described in [26].

External boundary conditions were defined at the far field boundaries for all simulations. This type of boundary condition determines whether the flow is locally entering or leaving the flow domain and is based on the Riemann invariants [26]. The free stream values of pressure, temperature, velocity vector, and turbulent viscosity are required inputs at external boundaries.

Low-speed operating conditions are required in the FAR 36 noise assessment. Therefore, the results presented in the following are for the Mach 0.25 takeoff condition summarized in Table 3.7. Both the front- and rear-rotor blade angle setting is

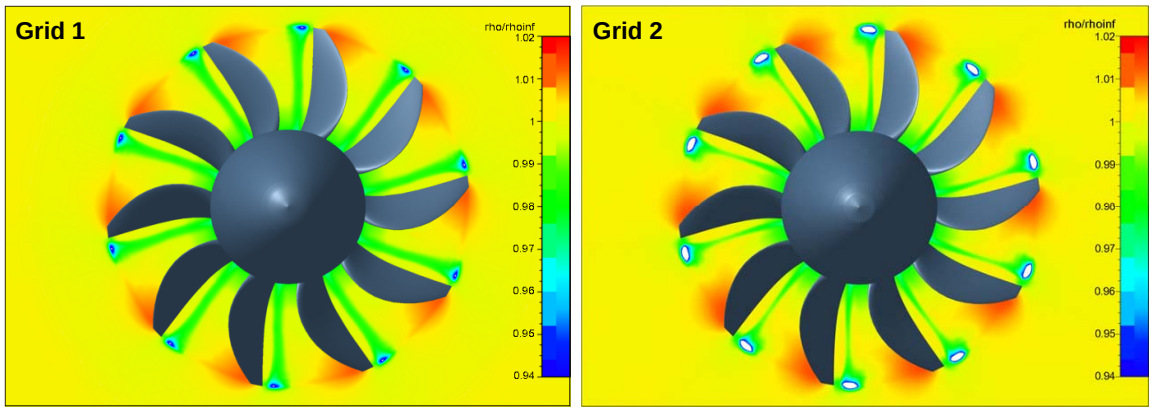

Figure 4-9: Baseline CRP density distribution at $x/D_1 = 0.12$ for grid 1 (left) and grid 2 (right)

46.5° at 75 % span measured from the tangential direction.

4.4.4 Steady Computations to Initialize Unsteady Simulations and Grid Convergence

First, the resolution of tip-vortices and viscous wakes was compared for the two meshing strategies illustrated in Figures 4-6 and 4-7. On a plane with constant axial location just downstream of the front-rotor tip trailing edge (at $x/D_1 = 0.12$, see Figure 4-8), the density distribution is presented for grids 1 and 2 on the left and right in Figure 4-9, respectively. A significant improvement was observed for the tip-vortex resolution achieved using grid 2. This improvement is mainly due to the continuous grid topology at the blade tip implemented in grid 2 and the elimination of non matching patches in the radial direction. In addition, the radial grid density was more than doubled between grids 1 and 2 which led to a significantly increased resolution of the viscous wake. In the light of these observations, it was decided to proceed with the grid 2 topology.

Steady single-passage computations performed on different grid levels were conducted next to further investigate grid convergence. Two flow quantities were analyzed to assess whether grid convergence was achieved: (1) the stagnation pressure downstream of the CRP, a measure for global performance such as thrust, and (2) the

static pressure on the blade surfaces as the determination of the surface pressure is ultimately the main objective of the aerodynamic analyses conducted in this research.

The grid depicted in Figures 4-7 and 4-8 corresponds here to a medium density mesh. Based in this mesh, a fine grid was obtained using FINE/Turbo's multigrid approach by doubling the cell count in every spatial direction. The single-passage medium grid featured 1.25 million cells. Consequently, the fine mesh consisted of 10 million grid cells.

Mass-averaged stagnation pressure results are presented in Figure 4-10 for both the medium and fine grids. The radial distribution of the stagnation pressure ratio did not change significantly when increasing the mesh density beyond the medium level. The measured stagnation pressure radial distribution at cruise is given for reference since measured takeoff data was not available in [2]. It should be noted that the details of the experimental CRP geometric design may be different from the baseline CRP design used in the CFD simulations (see Section 3.2.2). However, the level of the maximum stagnation pressure rise is similar as expected. For the takeoff condition there is an inward shift of the location of the maximum stagnation pressure ratio due to increased streamtube contraction compared to the cruise condition.

The front-rotor surface pressure distribution is illustrated for the medium and fine grid levels in Figure 4-11. The surface pressure coefficient c_p at two radial locations is depicted in Figure 4-12 (x/c denotes the axial distance from leading to trailing edge normalized by the blade chord c). Additional front- and rear-rotor radial stations were investigated as well. It was observed that there is no significant change in the surface pressure distribution when the mesh density is increased beyond the medium grid level. Based on the stagnation and surface pressure results presented above, it was determined that adequate flow resolution is achieved using the medium grid.

4.4.5 Unsteady Computations

Using the grid 2 topology, full-wheel unsteady simulations were carried out to study the flow mechanisms responsible for CRP interaction noise and to determine the time-varying blade pressures. Different computational setups were investigated and

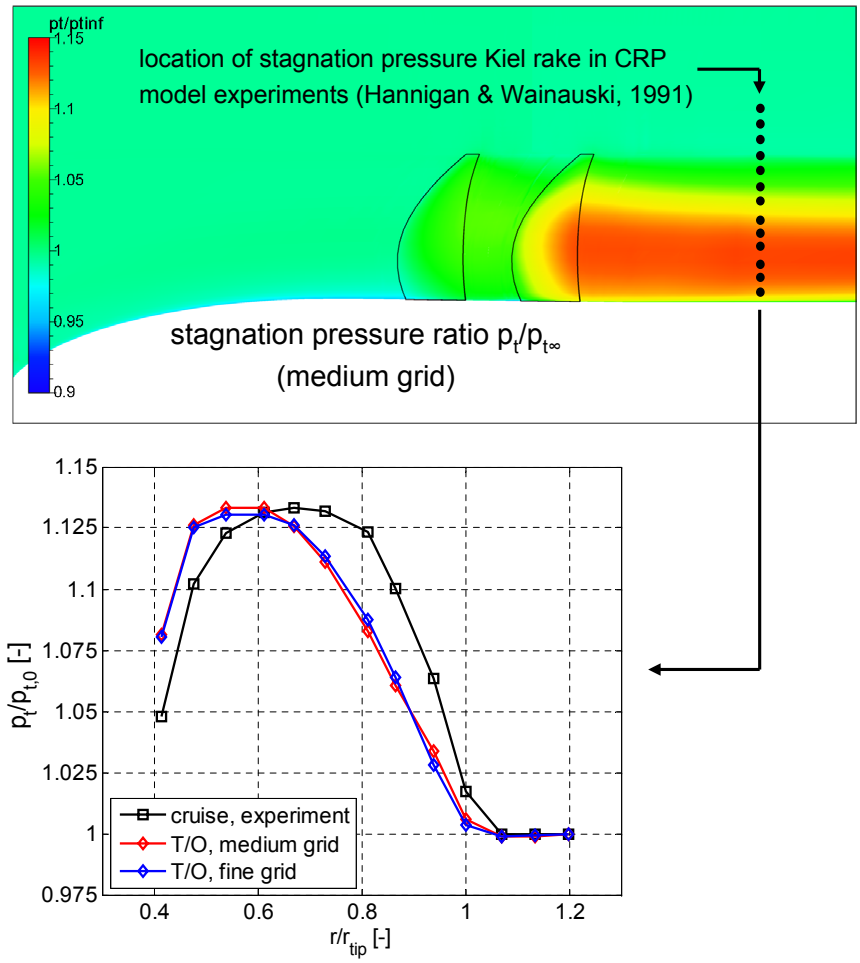

Figure 4-10: Baseline CRP radial distribution of mass-averaged stagnation pressure for medium and fine grid levels

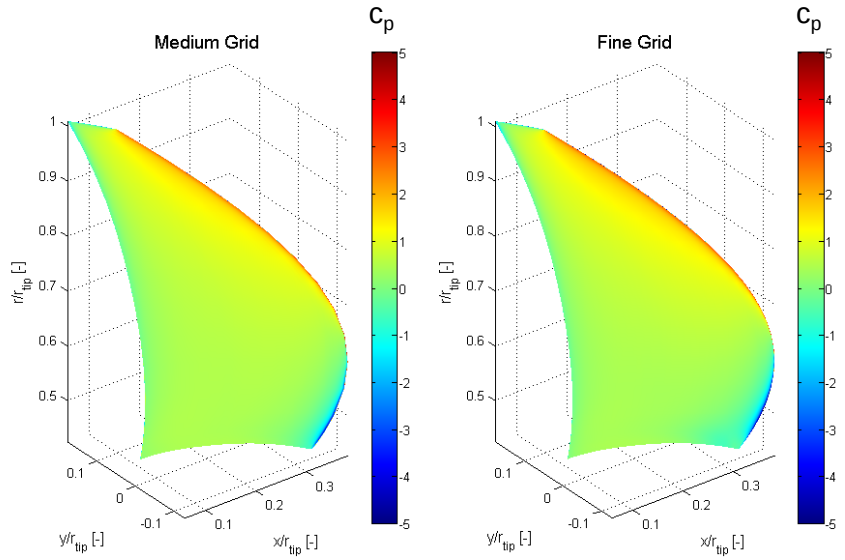

Figure 4-11: Surface pressure distribution on the baseline CRP front-rotor blades for medium and fine grid levels

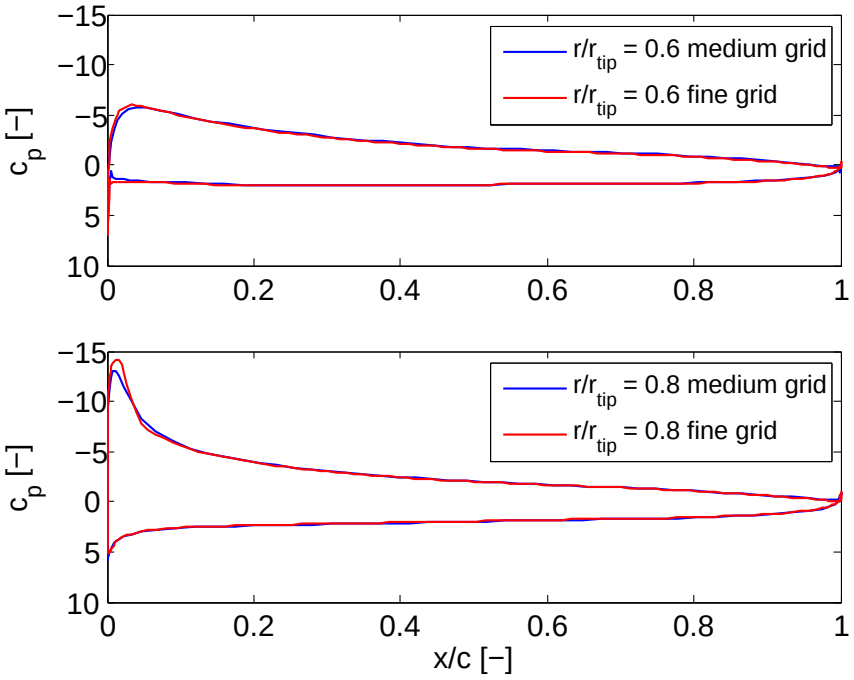

Figure 4-12: Front-rotor baseline CRP pressure coefficient at two radial stations for medium and fine grid levels

the approaches are summarized in Table 4.2.

Table 4.2: Characteristics of grid and time step sensitivity study

CFD Case	**Mesh**	**Computational Setup**
1	grid 1	simulate 2 full revolutions 800 time steps per revolution $BPF_1 \Delta t_{output} = 0.025$
2	grid 2	simulate 4 full revolutions 400 time steps per revolution $BPF_1 \Delta t_{output} = 0.05$
3	grid 2	simulate 5 full revolutions 1200 time steps per revolution $BPF_1 \Delta t_{output} = 0.0167$

In order to validate the CRP noise estimation approach it was decided to investigate the tonal content up to the fifth harmonic of the blade passing frequency. The required frequency range for the calculations of the baseline CRP interaction tone noise is therefore given as

$$f_{min} = BPF_2 =< f < f_{max} = 5 \cdot BPF_1. \tag{4.19}$$

In all three computational setups, the unsteady pressure information was recorded at every second time step, such that the physical time step is given by

$$\Delta t_{output} = \frac{2}{NA}, \tag{4.20}$$

where $N = N_1 = N_2$ is the rotational speed for the baseline CRP configuration and A denotes the number of angular positions per revolution. From the Nyquist criterion follows the maximum frequency that can be captured in the noise calculations as

$$f_{max,CFD} = \frac{BPF_1}{2\left(BPF_1 \Delta t_{output}\right)}. \tag{4.21}$$

The maximum frequency varies from $10 \cdot BPF_1$ in case 2 to $30 \cdot BPF_1$ in case 3 ensuring that the frequency range required for the noise calculations is covered at the upper end. At the lower end, the minimum required length of the recorded time

signal is given by

$$t_{min,CFD} = \frac{1}{f_{min}} = \frac{1}{BPF_2} = \frac{T}{8}, \tag{4.22}$$

where $T = 1/N$ denotes the time period. By recording the unsteady blade surface pressures for one full revolution, it is therefore assured that the lower end of the frequency range required for the noise estimation is captured as well.

However, it was found that achieving accurate wake and tip-vortex resolution downstream of the interface between the front-and rear-rotor domains is particularly challenging. Both the level of mesh density in the sub-domains between the rotors and the selection of the time step are critical in order to accurately capture wakes and tip-vortices. The wake transfer across the rotor-rotor interface is shown in Figure 4-13 for the three computational setups tabulated in Table 4.2. The case 1 simulation used grid 1 including the original meshing strategy with non-matching domain patches in the radial direction. The case 2 and 3 computations used grid 2, shown in Figure 4-7.

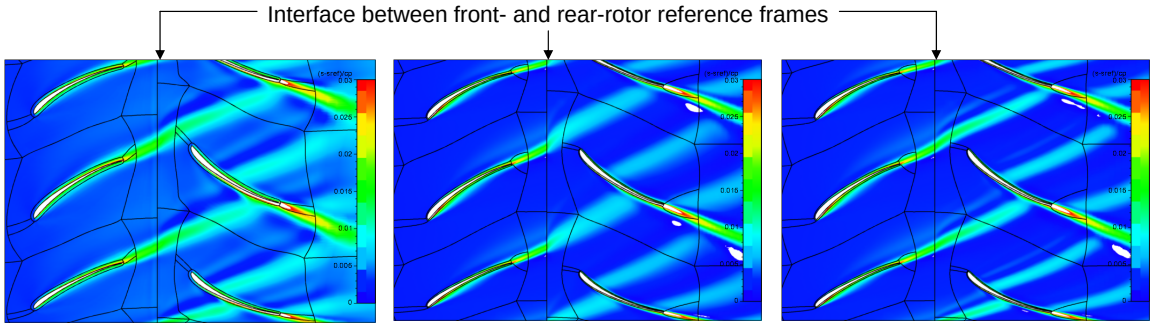

Figure 4-13: Baseline CRP entropy distribution near hub (10 % span) for CFD computational setup case 1 (left), case 2 (center), and case 3 (right)

Compared to case 1, the wake resolution downstream of the interface is reduced in case 2. This reduction is attributed to the selection of the time step. Compared to case 1, the radial grid density is doubled in case 2. However, the non-dimensional time step $BPF_1\Delta t = BPF_1\,(NA)$ was reduced from 0.025 to 0.0125. Even though the mesh density is increased and 4 full revolutions (up from 2 revolutions in case 1) are simulated, there is increased diffusion of the wake downstream of the interface. In

addition, the wake structure is discontinuous at the interface. In the third computational setup, the non-dimensional time step was further reduced to $BPF_1\Delta t = 0.0083$ and the results showed significant improvement in the wake resolution compared to both cases 1 and 2. Similar observations were made at mid-span and close to the blade tips.

In general, about $50,000$ iterations were required to reach a settled unsteady flow solution. This usually meant simulating 2 full revolutions. No improvement in the resolution of wakes and tip-vortices was observed when continuing the simulation at constant time step beyond 2 revolutions.

The CFD method presented in this chapter can be extended to include non-uniform inflow due to angle-of-attack effects or the influence of an upstream pylon. One approach to account for an upstream pylon is to apply a user-defined velocity profile at the inlet of the domain. A second computationally more expensive approach is to extend the grid domain to include the pylon surface.

4.4.6 General Guidelines for CFD Approach

The meshing strategy and the results of the grid and time step sensitivity studies presented above are summarized in the following set of general guidelines for the numerical setup:

1. The grid generation requires special care in the sub-domains between the front and rear rotor and near the blade tips such that high front-rotor viscous wake and tip-vortex resolution is assured. Single-passage steady computations can be used to investigate the tip-vortex and wake resolution upstream of the rotor-rotor interface.

2. It is observed that radially extending the mesh topology around the blade up to the far field boundary significantly improves tip-vortex resolution as discontinuous grid structures near the blade tips are avoided.

3. In the full-wheel unsteady simulations, a high resolution of the wake across the

interface between the front- and rear-rotor domains is particularly challenging. Both grid density and time step significantly affect the wake resolution.

In the pitchwise direction, approximately 90 grid points were found to give sufficient wake resolution. In the radial direction, 71 grid points were included in the rotor passage grid. However, the results of the grid sensitivity study suggest that the wake transfer across the interface is particularly affected the the radial cell density and the results can be improved by further increasing the radial grid density, especially near mid-span. The axial mesh density is observed to play a smaller role in resolving the CRP flow features. Approximately 120 grid cells are sufficient.

The choice of the physical time step and the required length of the recorded pressure signal is controlled by the frequency range relevant for the noise calculations. In order to capture the unsteadiness at the minimum required frequency, usually the smaller of the two blade passing frequencies, a minimum signal length of $t_{min} = 1/f_{min}$ needs to be recorded. In general, it was found that choosing a time step of $BPF\Delta t = 0.008$ yields the highest wake resolution across the interface.

4. The far field mesh may be relatively coarse. However, if the mesh density is not sufficient, high relative Mach numbers near the far field radial boundary can induce excessive artificial dissipation leading to non-physical flow phenomena in the far field regions. This can only be avoided by increasing the cell count. Implementing far-field stationary sub-domains requiring a sliding interface between the rotating rotor passage and the far field regions is not possible in FINE/Turbo.

   In axial and pitchwise direction, the far field mesh is constrained by the rotor passage topology. Defining the far field outer boundary at $4D_1$, 60 radial grid points were found to sufficiently prevent artificial dissipation. The location of the far field boundary itself is controlled by the streamtube capture area at the inlet to the domain. At the $M = 0.25$ takeoff condition, the steady simulations

suggest a streamtube capture area diameter of $1.2D_{tip}$ at the domain inlet. However, at lower speeds, the capture area will significantly increase and the far field boundary needs to be adjusted accordingly.

5. Simulating multiple revolutions at constant temporal resolution does not improve the flow resolution. In general, completing two full revolutions was required to reach a settled unsteady flow solution. In addition, recording the unsteady surface pressures for one full revolution is sufficient to capture the minimum frequency to be captured in the noise calculations, which is the lower of the first blade passing frequency harmonic of the two rotors. However, for full-scale configurations with significantly lower blade passing frequencies, it should be noted that multiple revolutions may be required to capture the interaction tones with low frequency content.

4.5 CRP Noise Method Validation

In order to validate the CRP noise estimation method, acoustic measurements for a CRP similar to a scale-model version of the baseline CRP were available. The operating conditions and overall geometry such as hub-to-tip ratio, rotor-rotor axial spacing, and sweep were identical. However, it is important to note that the details of the blade geometry (camber, thickness, or stacking line distribution) were not available from the literature and were not necessarily the same. In addition, the measurements included a pylon upstream of the CRP whereas uniform inflow was assumed in the computed baseline CRP noise results.

For axial microphone positions with polar angles $\theta = 85°$ and $\theta = 113°$, the narrowband spectra are given in Figure 4-14 and 4-15, respectively. In general, the first six interaction tones at frequencies $BPF_1 + BPF_2$, $BPF_1 + 2 \cdot BPF_2$, $2 \cdot BPF_1 + BPF_2$, $BPF_1 + 3 \cdot BPF_2$, $3 \cdot BPF_1 + BPF_2$, and $2 \cdot BPF_1 + 2 \cdot BPF_2$ are in good agreement with the measured data marked by the green circles.

The predicted rotor-alone tones decrease with BPF harmonic order due to the exponential decay in the Green's function in Equation 4.5. A similar decrease of rotor-

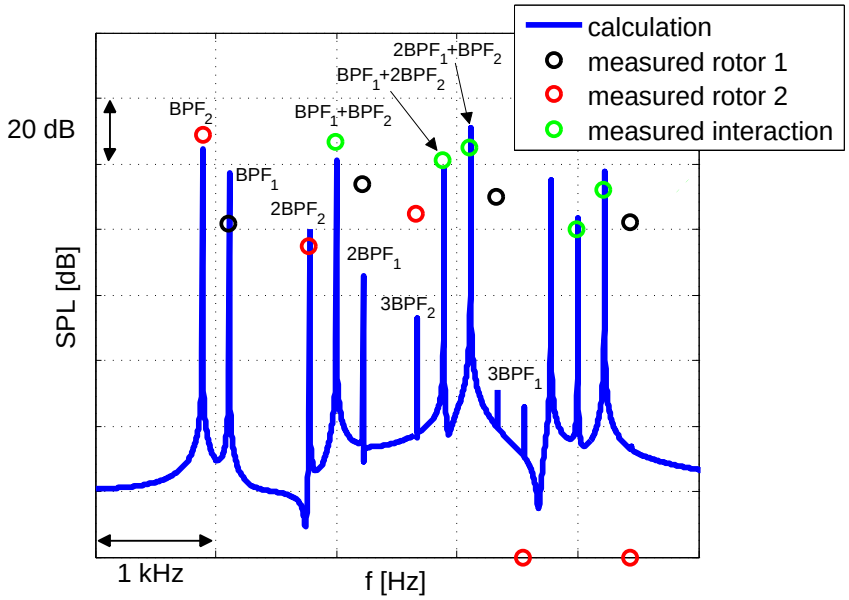

Figure 4-14: Baseline CRP spectrum at 85° polar angle from the inlet centerline

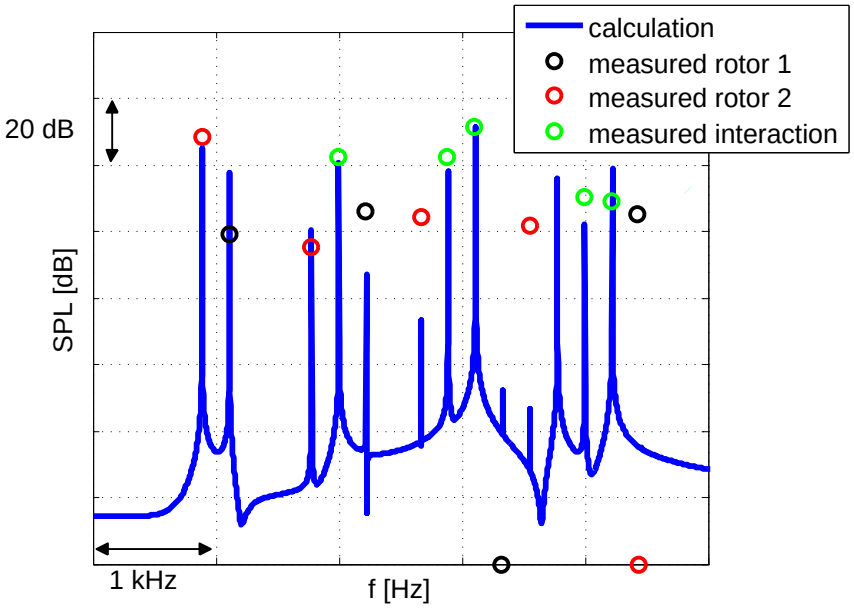

Figure 4-15: Baseline CRP spectrum at 113° polar angle from the inlet centerline

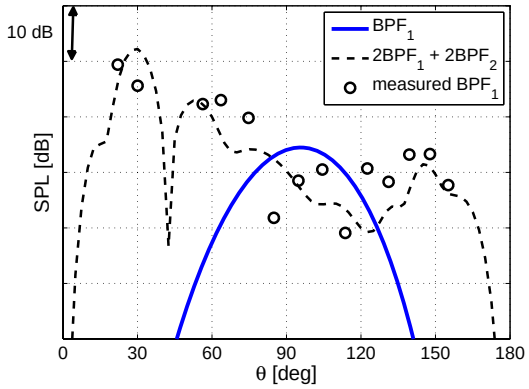

Figure 4-16: Baseline CRP front-rotor harmonic at frequency BPF_1

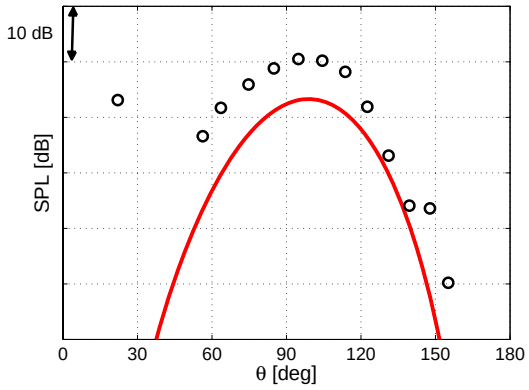

Figure 4-17: Baseline CRP rear-rotor harmonic at frequency BPF_2

alone tones with harmonic order is observed in [6], [52], and [53]. It is hypothesized that the discrepancies between the measured (black and red circles) and calculated rotor-alone tones are due to the strong influence of the upstream pylon present in the experiments.

Polar directivity results for the first rotor-alone tone of front- and rear-rotor are shown in Figures 4-16 and 4-17, respectively. In Figure 4-16, a typical calculated interaction tone directivity is displayed additionally. The measured BPF_1 results resemble the interaction tone directivity and there are significant differences to the computed results. These differences were thought to be primarily due to the interaction with the upstream pylon. The rear-rotor first BPF harmonic is less affected by the pylon effects and the computed results are in better agreement with the measured data as shown in Figure 4-17. Similar conclusions were reached in investigations of

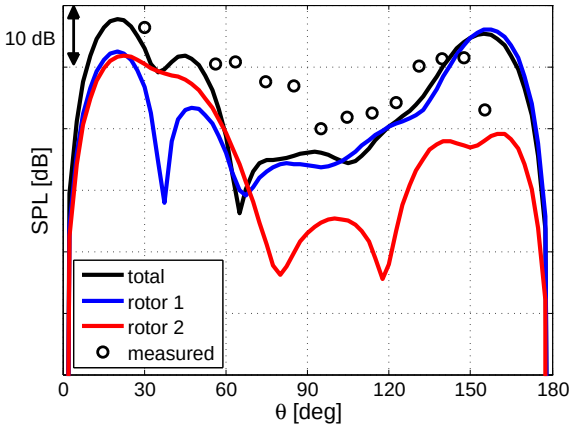

Figure 4-18: Baseline CRP interaction tone level at frequency $BPF_1 + BPF_2$

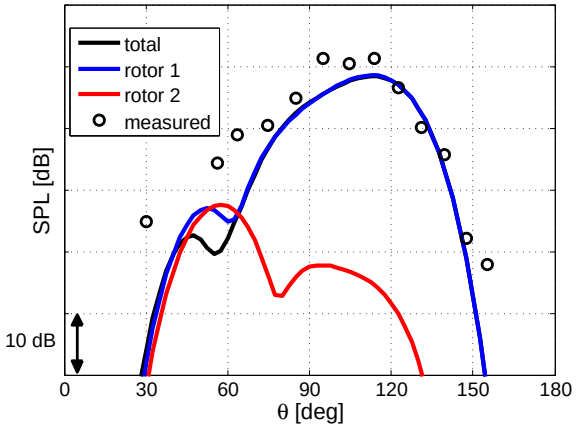

Figure 4-19: Baseline CRP interaction tone level at frequency $2 \cdot BPF_1 + BPF_2$

upstream pylon effects conducted by Janardan et al. [15] and Woodward et al. [16].

Polar directivity results are depicted in Figure 4-18 for the first interaction tone at frequency $BPF_1 + BPF_2$. The front-rotor contribution to the interaction tone level is marked in blue and the contribution from the rear rotor is marked in red. The acoustic measurement data is indicated by the circles and the total computed noise is marked by the black line.

The interaction tone noise levels at frequencies $2 \cdot BPF_1 + BPF_2$ and $BPF_1 + 2 \cdot BPF_2$ are shown in Figures 4-19 and 4-20, respectively. Overall, there is good agreement between the calculated and measured data. The larger discrepancies at around $\theta = 75°$ of the $BPF_1 + BPF_2$ interaction tone and at the low polar angle range of the $2 \cdot BPF_1 + BPF_2$ interaction tone are most likely due to (1) the significant

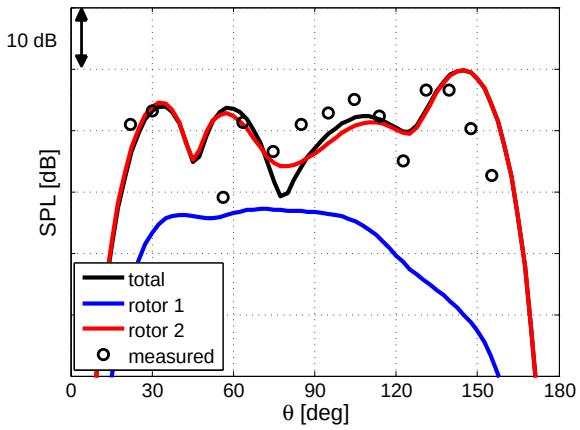

Figure 4-20: Baseline CRP interaction tone level at frequency $BPF_1 + 2 \cdot BPF_2$

influence of non-uniform inflow generated by the upstream pylon as investigated in detail for example by Janardan et al. [15] and Woodward [54] and (2) the differences in the blade geometric design between the baseline CRP and the experimental model CRP. In particular, in contrast to the model scale CRP used for the acoustic measurements, the formation of a leading edge vortex was not observed for the baseline CRP due to its relatively high camber. Thus, in addition to the influence of an upstream pylon, the interaction of a leading edge vortex is thought to also contribute to the discrepancies between the calculated and measured noise levels.

In addition to the results displayed in Figures 4-18 and 4-20, interaction tone noise levels were compared at frequencies $2 \cdot BPF_1 + BPF_2$, $2 \cdot BPF_1 + 2 \cdot BPF_2$ and $BPF_1 + 3 \cdot BPF_2$. The trends are similar to the observations described above; in general, there is good agreement between the predicted and measured data validating the developed CRP noise estimation approach.

Moreover, it is observed that for the interaction tone at frequency $BPF_1 + BPF_2$ both the front- and rear-rotor noise significantly contribute to the overall CRP noise. The rear-rotor contribution is dominant in much of the forward arc whereas the front-rotor contribution is dominant in the rear polar arc. The noise source mechanisms generating front-rotor interaction tone noise is the upstream influence of the rear rotor. On the other hand, front-rotor tip-vortices, wakes, and hub wake/boundary layer interfere with the rear rotor and produce rear-rotor interaction noise. It can be

seen in Figures 4-18 and 4-20 that the interaction tone at frequency $2 \cdot BPF_1 + BPF_2$ is governed by the front-rotor contribution while the interaction tone at frequency $BPF_1 + 2 \cdot BPF_2$ is governed by the rear-rotor contribution. These trends are further investigated in the next chapter where the four noise mechanisms assumed responsible for CRP interaction noise are dissected and their impact is quantified.

In summary, a CRP noise estimation method based on Goldstein's formulation of the acoustic analogy for moving media and Hanson's single rotor noise approach extended to counter-rotating configurations was established and validated with experimental data. The method requires the a priori determination of the time-varying blade surface pressures. Thus, a high-fidelity CFD approach was demonstrated to successfully capture the underlying aerodynamic mechanisms and to compute the blade loading data required for the definition of the acoustic source terms. The acoustic performance assessment for advanced CRP configurations using the developed noise method is discussed next.

Chapter 5

CRP Acoustic Assessment

The acoustic performance of the baseline CRP is assessed using the established CRP noise estimation method. The underlying noise mechanisms are dissected and quantified first. Based on the insight gained, the CRP is then re-designed for reduced noise. It is hypothesized that carefully incorporating advanced source mitigation concepts in a re-designed CRP can result in substantial noise reductions. Finally, the acoustic performance of the re-designed CRP is discussed and the noise reduction relative to the baseline CRP is quantified.

5.1 Dissection of Baseline CRP Noise Mechanisms

The approach to the dissection and quantification of the CRP noise mechanisms is described below. In order to quantify the relative effect of tip-vortex interaction at the interaction tone frequency under consideration, the loading source is computed between 75 % and 100 % on the rear rotor only. In this spanwise range, which was determined by investigating the tip-vortex trajectory, it is hypothesized that the tip-vortex interaction mechanism is the dominant contributor to the interaction tone noise.

Similarly, the hub wake/endwall boundary layer noise source mechanism is assumed to control the interaction noise generation between 0 % and 12.5 % span, and the viscous wake related mechanism is conjectured to be the dominant contributor

in the remaining spanwise range. The influence of the rear-rotor potential field is calculated by accounting for the loading sources on the front rotor only. The noise source dissection is summarized in Table 5.1.

Table 5.1: Radial extent of contributing source mechanisms

Noise Source Mechanism	**Contributing Rotor**	**Spanwise Range**
Upstream influence	Front	$0 - 100$ %
Tip-vortex	Rear	$75 - 100$ %
Viscous wake	Rear	$12.5 - 75$ %
Hub wake/endwall BL	Rear	$0 - 12.5$ %

The sectional loading distribution on the front rotor measured by the time-varying lift coefficient c_l is depicted in Figure 5-1. The lift coefficient is non-dimensionalized by the steady sectional lift coefficient $c_{l,steady}$. At mid-span, the front-rotor loading variation is 14 % of the steady loading level due to the influence of the rear-rotor potential field, which is illustrated in Figure 4-1. Near the tip at 95 % span, the variation relative to the steady loading decreases to 8.5 % in amplitude due to the reduced strength of the potential field on the rear-rotor. Additional spanwise sections were investigated and it was found that rear-rotor upstream influence significantly impacts the front-rotor loading over the entire spanwise range. Loading variations of up to 15 % in amplitude relative to the steady loading level were observed.

The front-rotor tip-vortices and viscous wakes are depicted in Figures 4-3 and 4-4, respectvely. Near the tip, the rear-rotor loading is significantly affected by the front-rotor tip-vortex, as illustrated in Figure 5-2. The variation reaches 12 % of the steady loading level. At mid-span, the front-rotor viscous wakes cause the rear-rotor loading to vary with an amplitude of approximately 4 %. In general, tip-vortex effects were found to cause larger variations in loading than wake effects.

The relative contributions of each of the underlying mechanisms are depicted in Figures 5-3, 5-4, and 5-5 by means of interaction tone directivities at frequencies $BPF_1 + BPF_2$, $2 \cdot BPF_1 + BPF_2$, and $BPF_1 + 2 \cdot BPF_2$, respectively.

For the first interaction tone, the noise level is dominated by a combination of

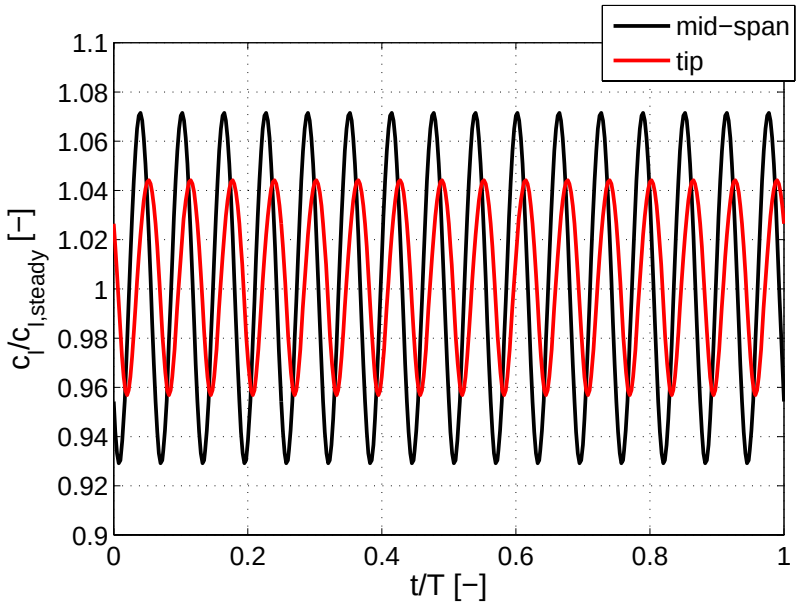

Figure 5-1: Distribution of section lift coefficient on front rotor, $M = 0.25$

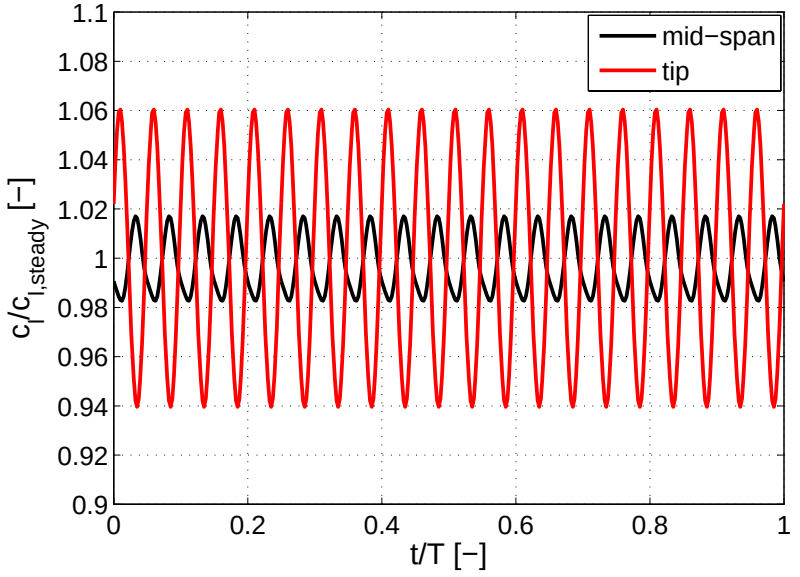

Figure 5-2: Distribution of sectional lift coefficient on rear rotor, $M = 0.25$

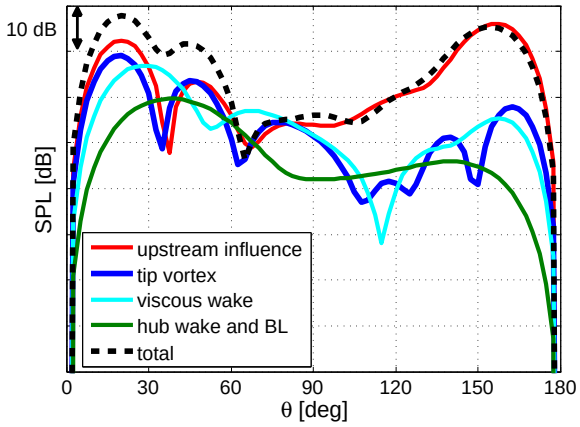

Figure 5-3: Dissection of baseline CRP noise mechanisms for interaction tone $BPF_1 + BPF_2$, $M = 0.25$

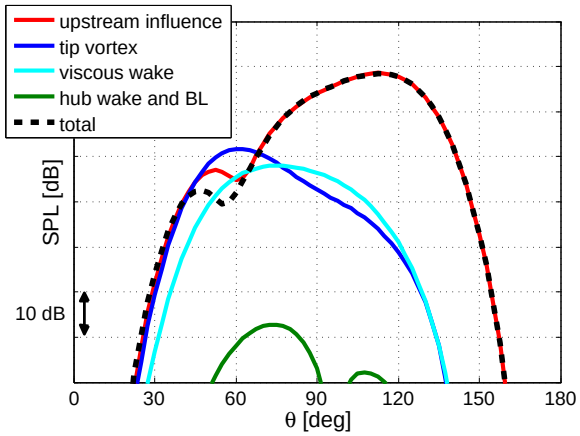

Figure 5-4: Dissection of baseline CRP noise mechanisms for interaction tone $2 \cdot BPF_1 + BPF_2$, $M = 0.25$

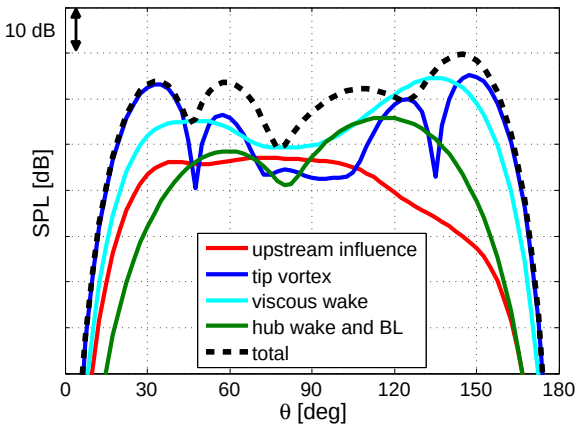

Figure 5-5: Dissection of baseline CRP noise mechanisms for interaction tone $BPF_1 + 2 \cdot BPF_2$, $M = 0.25$

upstream influence, tip-vortex and viscous wakes in the forward arc, whereas the upstream influence dominates the noise level in the aft arc. It should be noted that destructive and constructive interference effects can lead to the total CRP noise level falling below the contributions from either the front or the rear rotor as observed for example for the polar angle range between 60° and 80° for the first interaction tone in Figure 5-3. On the rear-rotor, tip-vortex effects therefore generate larger loading variations than the front-rotor viscous wakes as illustrated in Figure 5-2. However, tip-vortex effects are limited to 25 % of the span while viscous wake effects are conjectured to influence the rear rotor on 62.5 % of the span. Tip-vortex and wake effects thus generate similar contributions to the CRP noise at the first interaction tone frequency.

Tip-vortex interaction is suggested to control the interaction tone $2 \cdot BPF_1 + BPF_2$ up to a polar angle of 70°. In the aft arc, the potential field interaction dominates as shown in Figure 5-4. Over a wide range of polar angles the interaction tone $BPF_1 + 2 \cdot BPF_2$ is again governed by all noise source mechanisms as shown in Figure 5-5.

The noise source dissection analysis for the first six interaction tones is summarized in Figure 5-6. The mean sound pressure levels were computed for the forward and aft arcs respectively and the noise source mechanisms were quantified based on their acoustic pressure contributions to the mean sound pressure levels. In conjunction with the detailed directivity results, this approach allows to directly assess and to prioritize the impacts of the different noise source mechanisms.

The following observations can be made. (1) As expected, the interaction of rear-rotor upstream influence with the front rotor dominates the interaction tones at multiple frequencies of the front rotor, $2 \cdot BPF_1 + BPF_2$, and $3 \cdot BPF_1 + BPF_2$. (2) Similarly, noise from tip-vortex interaction with the rear rotor is more pronounced in interaction tones at multiple frequencies of the rear rotor, $BPF_1 + 2 \cdot BPF_2$, and $BPF_1 + 3 \cdot BPF_2$. (3) Interaction tones at equal multiples of rotor frequency, $BPF_1 + BPF_2$ and $2 \cdot BPF_1 + 2 \cdot BPF_2$, are suggested to be governed by all noise source mechanisms.

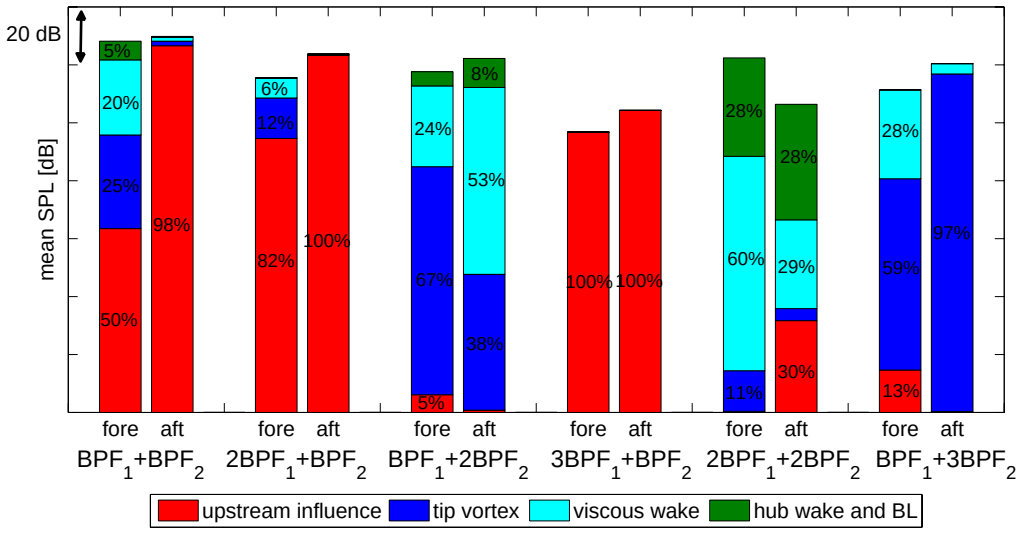

Figure 5-6: Baseline CRP noise mechanism contributors to first six interaction tones (percentages based on p'^2 averaged over forward and aft polar arcs), $M = 0.25$

It is important to note the following implication relative to potential noise reduction strategies: although certain interaction tones are dominated by one or another mechanism with possible preferences either in the front or rear arcs, to achieve significant interaction tone noise reductions, ***all noise mechanisms*** need to be addressed. This is the key objective of the advanced design CRP discussed next.

5.2 Advanced CRP Design for Reduced Noise

Based on the above baseline CRP acoustic investigation, the CRP was re-designed with the focus on reducing interaction tone noise while maintaining or possibly improving the aerodynamic performance. The development of the advanced design CRP for reduced noise is presented first. Next, the results of the noise mechanism dissection are described followed by the discussion of the acoustic performance benefit relative to the baseline CRP.

5.2.1 Design Approach

The following four noise reduction technologies were implemented: (1) increased rotor-rotor axial spacing, (2) reduction of the rear-rotor diameter, (3) differential

tip speeds, and (4) blade count variations.

Increasing the axial spacing between the rotor results in an increased decay of the front-rotor viscous wakes and tip-vortices reducing the interaction with the rear rotor. In addition, the strength of the rear-rotor potential field near the front rotor is significantly reduced. Therefore, it is hypothesized that increased rotor-rotor spacing will mitigate several interaction tone mechanisms, in agreement with noise reductions previously reported by for example Janardan et al. [15] and by Woodward et al. [17].

The rear-rotor diameter was also reduced to potentially eliminate the interaction of the front-rotor tip-vortices [14]. For the baseline CRP, the core of the front-rotor vortex interacts with the rear rotor at approximately 90 % span. Between 90 % and 75 % span, the strength of the interaction of front-rotor tip-vortex with rear rotor gradually decreases with increasing radial distance from the vortex core. At 75 % span, the interaction of the front-rotor viscous wakes outweighs the tip-vortex influence. Thus, the rear rotor was clipped at 75 % span. To maintain the thrust level, the loading on the remaining part of the blades needs to be increased for a clipped rotor. This can be achieved either by increasing the blade angle setting or the tip speed, or a combination thereof. In return, however, a higher rear-rotor blade loading leads to an increased upstream influence, which can impair the acoustic benefits of increased rotor-rotor axial spacing. Compared to the baseline CRP design, the thrust and propulsive efficiency were maintained at the takeoff condition, which is relevant for the noise assessment. In order to limit the loading increase on the rear rotor while maintaining thrust, the number of blades was increased from 8 to 11. A model scale version of the advanced CRP configuration is used for the acoustic assessment and dissection of noise mechanisms such that the results can be compared to the model scale baseline CRP data on a consistent basis. The model scale advanced CRP configuration and the details of the takeoff operating conditions are given in Table 5.2.

Since the CRP configuration significantly changed compared to the baseline CRP, the CFD simulations necessary for further aerodynamic and acoustic analysis of the advanced CRP design required the generation of a modified full-wheel numerical grid.

Table 5.2: Model scale advanced CRP configuration and takeoff operating parameters

Configuration Characteristics		**Takeoff Operating Condition**	
D_1 (m)	0.56	M (-)	0.25
D_2 (m)	0.475	h (m)	Sea level
B_1 (m)	10	J (-)	1.72
B_2 (m)	11	N_1 (rpm)	$6,665$
x/D_1 (-)	0.35	N_2 (rpm)	$5,332$
r_{hub}/r_{tip} (-)	0.4	β_1 (°)	50.3
		β_2 (°)	50.5

The baseline CRP meshing strategy outlined in Section 4.4.2 was also applied to the advanced design CRP. However, compared to the baseline CRP grid, additional cells were needed in the blocks between the two rotors as the rotor-rotor axial spacing increased by 56 %. The axial cell count between the two rotors was consequently raised by 50 %.

Moreover, clipping the rear rotor required an increase in grid density between the rear-rotor blade tip and the far field sub-domain to accurately resolve the front-rotor tip-vortex in this region. In total, the radial grid point count was increased to 133 from 71 for the baseline CRP grid. The meridional view of the radial grid structure is depicted in Figure 5-7. The grid generation approach used in Autogrid is as follows:

1. The unclipped front- and rear-rotor geometries are imported including the increased rotor-rotor spacing.

2. In order to implement the reduced rear-rotor diameter, an increased tip gap is defined and the solid blade geometry is clipped at 75 % span.

3. The radial grid point count is adjusted manually such that high grid density is maintained in the path of the front-rotor tip-vortex convection.

4. The radial cell size is ensured to be continuous at the interface between the rotor reference frames.

Due to the addition of axial and radial cells, the advanced design CRP full-wheel mesh size increased to 26 million cells. The geometry of the advanced design CRP

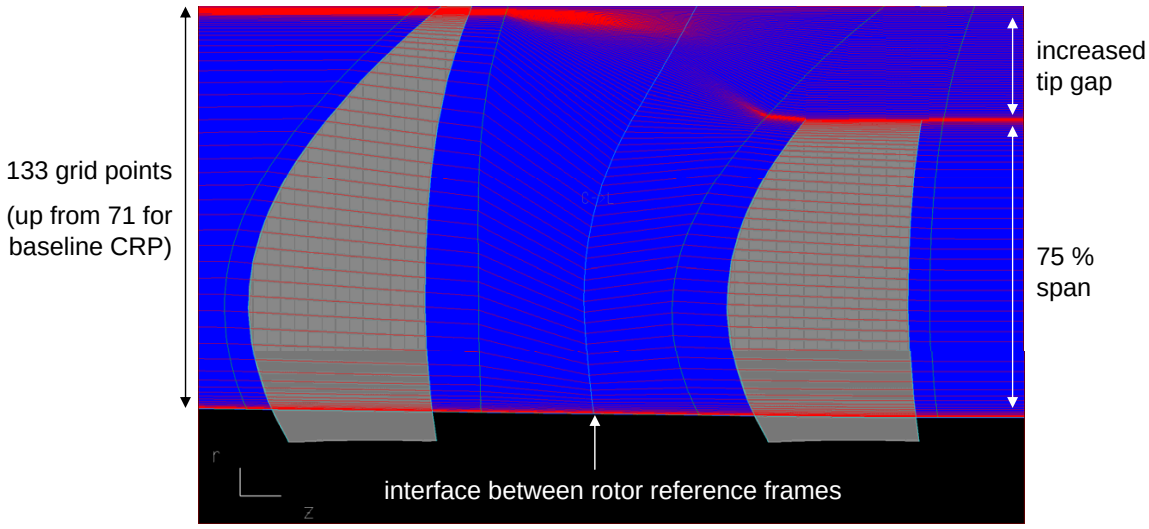

Figure 5-7: Advanced design CRP radial grid topology

is presented in Figure 5-8 along with the near-field density distribution showing the front- and rear-rotor tip-vortices as well as the rear-rotor viscous wake.

5.2.2 Acoustic Performance for Advanced Design CRP

For the advanced design CRP, the periodicity is $4T_2 = 5T_1$, as the tip speed ratio is $N_1/N_2 = 1.25$. Therefore, in order to capture all of the loading frequencies, it is necessary to record the surface pressure for every blade over four rear-rotor revolutions (equivalent to five front-rotor revolutions). Due to data processing and CPU time limitations the remaining analysis is based on surface pressures recorded for 1.5 rear-rotor revolutions after reaching quasi-periodic flow conditions.

The first three interaction tone directivities are compared for the baseline and advanced design CRPs in Figures 5-9, 5-10, and 5-11. For all three interaction tone frequencies, the noise levels are significantly reduced over a wide range of polar directivity angles. The advanced design CRP interaction tone levels do not approach zero at low and high polar angles which is conjectured to be due to the influence of unequal tip speeds. For equal tip speeds, there are substantial destructive interference effects reducing the noise levels close to the axis of rotation.

At the first interaction tone frequency, $BPF_1 + BPF_2$, the maximum noise level

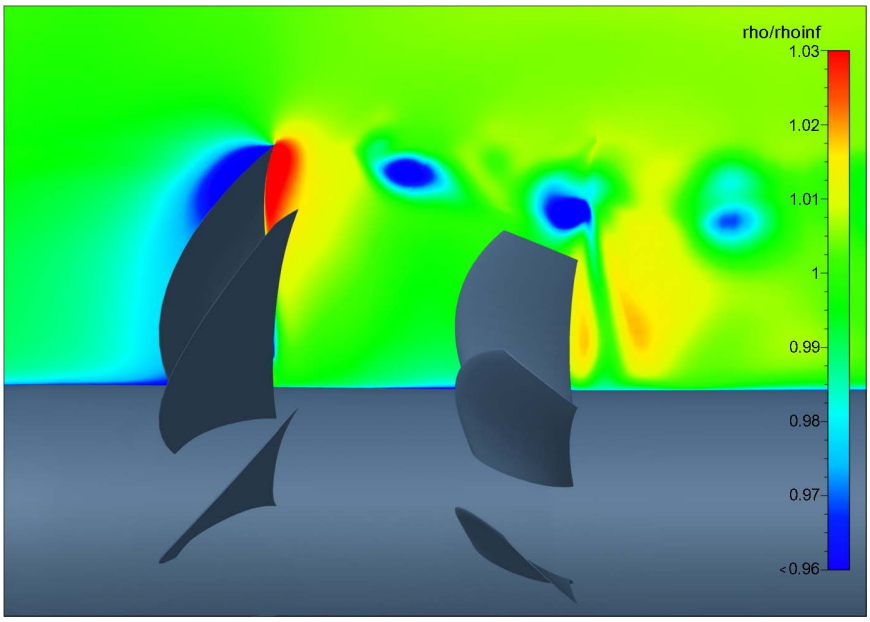

Figure 5-8: Advanced design CRP geometry and near-field density distribution

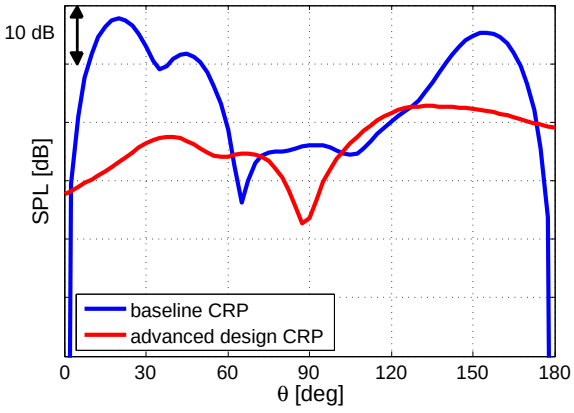

Figure 5-9: Comparison of baseline and advanced design CRP directivity at interaction tone frequency $BPF_1 + BPF_2$, $M = 0.25$

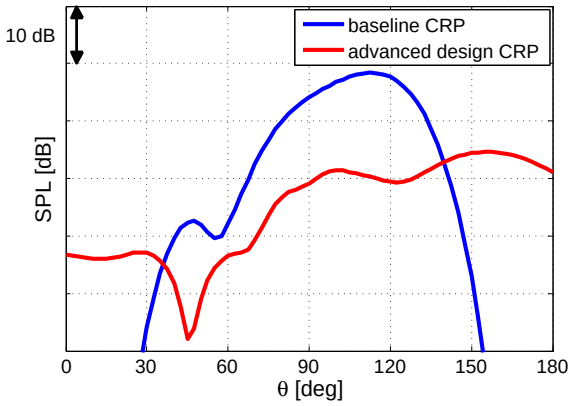

Figure 5-10: Comparison of baseline and advanced design CRP directivity at interaction tone frequency $2 \cdot BPF_1 + BPF_2$, $M = 0.25$

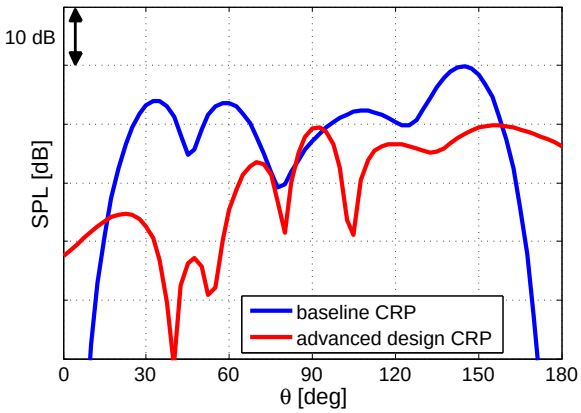

Figure 5-11: Comparison of baseline and advanced design CRP directivity at interaction tone frequency $BPF_1 + 2 \cdot BPF_2$, $M = 0.25$

is reduced by 21 dB in the forward arc as illustrated in Figure 5-9. This reduction is attributed to the decreased interaction of front-rotor tip-vortices and wakes with the rear rotor, and the decreased interaction of the rear-rotor potential field with the front rotor, as these mechanisms dominated the forward arc for the baseline CRP. In the aft arc, the maximum noise level is reduced by 13 dB due to the decreased strength of the rear-rotor upstream influence.

The maximum noise level at the second interaction tone frequency, $2 \cdot BPF_1 + BPF_2$, shown in Figure 5-10, is reduced by 15 dB. For the baseline CRP, the second interaction tone is governed by rear-rotor upstream influence over the entire polar angle range. The reduction in potential field strength near the front rotor due to increasing the rotor-rotor spacing by 56 % results in significant noise reductions at interaction tone frequencies previously dominated by rear-rotor upstream influence.

At the third interaction tone frequency, $BPF_1 + 2 \cdot BPF_2$, the maximum noise level is reduced by approximately 10 dB in both the forward and aft arc as illustrated in Figure 5-11. This reduction is attributed to the decreased interaction of front-rotor tip-vortices and wakes with the rear rotor.

In general, the acoustic power is more evenly spread over the polar arc due to unequal tip speed effects and the maximum noise levels in the forward and aft arcs are reduced by up to 20 dB at the first three interaction tone frequencies.

The dissected CRP noise mechanisms are presented in Figure 5-12. Similar to the baseline CRP case, the effects of the noise mechanisms are quantified by computing the loading source terms for a spanwise section only. Based on analyzing the tip-vortex trajectory it is assumed that the acoustic interaction of the front-rotor tip-vortex with the rear-rotor blade tip is limited to $90\ \% - 100\ \%$ of rear-rotor span. The front-rotor viscous wakes affect the rear rotor over the $17\ \% - 90\ \%$ rear-rotor span range, while the front-rotor hub wake influences the rear-rotor loading between 0 % and 17 % span.

As expected, clipping the rear-rotor blade results in a significant reduction in tip-vortex interaction as depicted in Figure 5-12. Viscous wake and upstream influence effects now become the dominant noise source mechanisms as both the wake strength

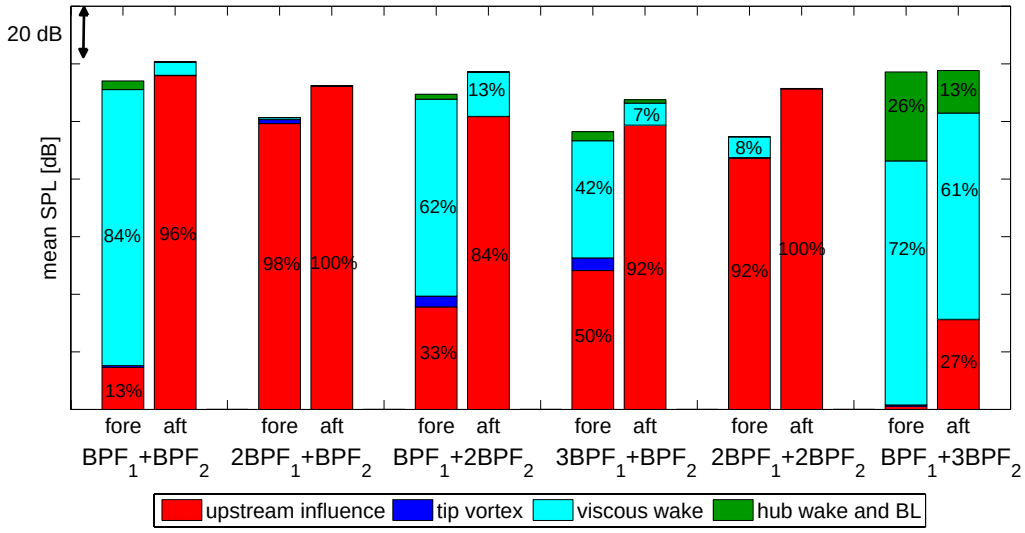

Figure 5-12: Advanced design CRP noise mechanism contributors to first six interaction tones (percentages based on p'^2 averaged over forward and aft polar arcs), $M = 0.25$

and the strength of the potential field interactions are substantially increased due to a higher front-rotor loading.

Overall, the noise levels are greatly reduced, in particular for the first three interaction tones, as summarized in Figure 5-13. Averaged over all interaction tones investigated, the mean SPL is reduced by 7.25 dB. For the first three interaction tones, the average noise reduction is 11 dB. Since the interaction tone levels are spread over a larger range of polar angles, the mean SPL actually increases for some of the higher interaction tone frequencies, such as for example in the forward arc of the interaction tone at $BPF_1 + 3 \cdot BPF_2$.

5.2.3 Summary of Results

The acoustic performance investigations of the baseline and advanced design indicate that, in order to achieve significant noise reductions, it is important to implement noise reduction technologies that address ***all*** noise source mechanisms at play as the

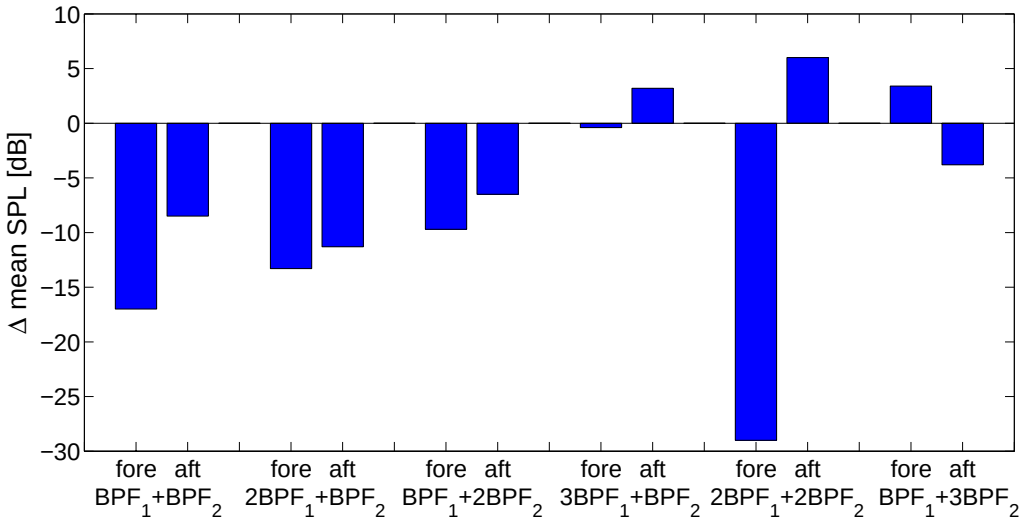

Figure 5-13: Relative change in mean SPL for advanced design CRP compared to baseline CRP

overall noise is governed by a multiple sources of similar strength.

By clipping the rear rotor at 75 % and increasing the rotor-rotor axial spacing by 56 %, the relative importance of the front-rotor tip-vortices interfering with the rear rotor was nearly eliminated (smaller than 5 % at all interaction tone frequencies) and reductions of up to 20 dB in maximum noise levels in the front and aft arcs were achieved at interaction tones previously dominated by tip-vortex effects. Similarly, maximum noise levels at interaction tone frequencies previously governed by upstream influence effects were reduced by up to 15 dB.

Generally, the acoustic power was spread over a larger range of polar angles for the advanced design CRP which is conjectured to be due the influence of operating the rotors at unequal tip speeds. This led to reductions of 7.25 dB in mean SPL averaged over the front and aft arcs for the six three interaction tones. At the higher interaction tone frequencies, spreading the acoustic power actually resulted in increased mean sound pressure levels.

Clipping the rear rotor, increasing the axial spacing and operating at differential tip speeds are effective approaches to reduce CRP interaction noise. Further increasing the axial spacing is assumed to result in additional acoustic benefits. However, the trade-offs between acoustic and aerodynamic performance need to be carefully

investigated as the propulsion system weight and the amount of swirl recovered by the rear rotor are negatively impacted by increasing the rotor-rotor spacing.

Chapter 6

System Level Noise Assessment

The previous chapter demonstrated that significant noise reductions can be achieved by implementing source mitigation concepts targeting all of the underlying noise source mechanisms. Using the overall integrated performance and noise assessment methodology depicted in Figure 2-1, the acoustic performance of the baseline and advanced design CRP aircraft arrangements is investigated on the system level next. The noise levels from the CRP aircraft configurations are compared to the datum turbofan powered aircraft in order to assess whether it is possible to achieve CRP noise levels similar to those of an advanced turbofan powered aircraft.

6.1 Low-Speed Aerodynamic Performance

The low-speed performance computed in FLOPS up to an altitude of $3,400$ ft is presented in 6-1. In general, Mach number and altitude distribution along the trajectory show similar trends. The thrust levels of the CRP configurations are increased along the trajectory compared to the datum turbofan aircraft mainly due to the increased takeoff weight.

Similar to the baseline CRP, the advanced design CRP was also sized to full scale at the takeoff condition. Both designs feature the same front-rotor diameter and tip speed but the rear-rotor characteristics differ as summarized in Table 6.1. Simulating the advanced design CRP in RVL/RAXAN, it is ensured that the propulsive efficiency

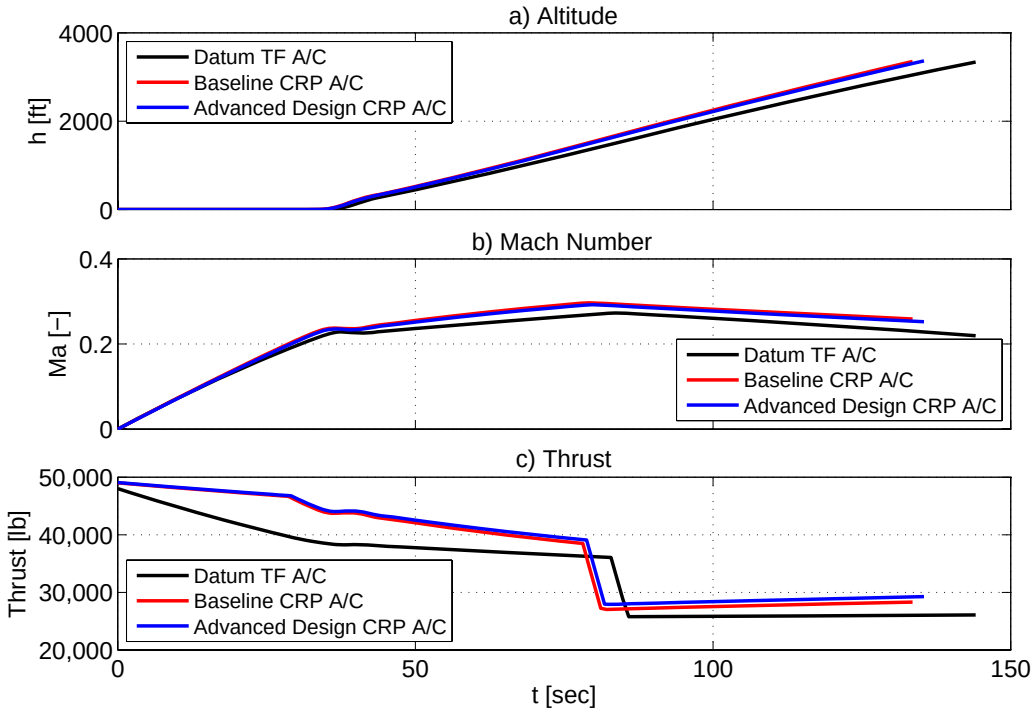

Figure 6-1: Takeoff performance of investigated aircraft configurations: a) altitude, b) Mach number, and c) thrust lapse

is maintained.

Since the rear-rotor tip speed was reduced for the advanced design CRP, the required planetary gearbox ratio between the low-pressure spool and the rear-rotor shaft increased from 8 : 1 to 10.1 : 1. Compared to the baseline CRP, the loading on the front-rotor blades is larger than the rear-rotor loading, which is reflected in a reversal of the torque split. The larger torque is transferred through the planetary gearbox carrier. As the carrier driven rotor must be located farthest away from the engine core, the advanced CRP design is suggested to be more suitable for a tractor configuration. Based on discussions with the industry partner, a 5 % increase in the propulsion system weight was assumed in the mission and overall performance analysis to account for the increased rotor-rotor spacing and the additional blades of the rear rotor. Thus, the required thrust levels for the advanced design CRP are slightly increased compared to the baseline CRP aircraft as illustrated in Figure 6-1.

In general, the takeoff trajectories are similar for all three aircraft configurations

Table 6.1: Full scale baseline and advanced design CRP configuration and takeoff operating point characteristics

	Baseline CRP	Advanced Design CRP
D_1 (m)	3.81	3.81
D_2 (m)	3.81	3.24
B_1 (m)	10	10
B_2 (m)	8	11
x/D_1 (-)	0.35	0.35
r_{hub}/r_{tip} (-)	0.4	0.4
β_1 (°)	46.5	50.3
β_1 (°)	46.5	50.5
N_1 (rpm)	934	934
N_2 (rpm)	934	747.2
Θ (-)	45/55	53/47
T_{TO} (kN)	91.2	91.5
η_{prop} (%)	67.7	67.7

and significant differences in the propagation effects on the noise results are not expected. It has to be mentioned that approach noise results for the CRP aircraft arrangements could not be obtained in this research project due to computational limitations and related time constraints. Therefore, the performance results at approach are omitted here.

6.2 Acoustic Performance of CRP Powered Aircraft

The acoustic performance of the baseline and advanced design CRP aircraft configurations was investigated by separating engine and airframe noise sources in terms of the FAR 36 measures tone-corrected perceived noise levels (PNLT) and effective perceived noise levels (EPNL). The assumptions made in the analysis are outlined below.

Due to data processing limitations, the cycle parameters required for the engine core noise sources (LPC, combustor, LPT, and fan and jet in the case of the turbofan)

are computed for three operating conditions along the takeoff trajectory (at Mach 0.1, when the aircraft begins rotation, and at cutback) and one operating condition on the approach trajectory (at 6,560 ft ahead of the runway) only. The cycle parameters are assumed constant between the calculated operating conditions at takeoff and for the entire approach trajectory.

From the engine cycle analysis for the takeoff condition, the maximum change of the parameters influencing engine noise between the first and second computed conditions (between $M = 0.1$ and the start of the aircraft rotation) is 5.5 % (for the turbine inlet temperature). Similarly, the maximum change between the second and third calculated conditions (between the start of the aircraft rotating and just before cutback) is 6 % (for the core mass flow). Thus, assuming constant cycle parameters will not considerably impact the engine noise levels at takeoff. At approach, the thrust requirement and flight velocity are nearly constant until the aircraft touches down and decelerates. The engine cycle parameter change by less than 2 % and assuming constant cycle inputs is not believed to affect the engine noise levels at approach.

The unsteady blade loading was computed for the $M = 0.25$ takeoff condition only. CFD simulations at cutback and approach operating conditions were not carried out and the noise estimation at the FAR 36 observer location is omitted here but can be performed in the future. In order to account for the noise benefit due to cutback, a reduction of 2 PNdB was applied to the flyover and sideline PNLT results at the location of cutback. This assumption is based on a preliminary noise analysis for the baseline CRP using FINE/Turbo's single passage non-linear harmonic (NLH) method to determine the unsteady blade surface pressures. In this analysis, only the first two loading harmonics could be captured leading to underestimated interaction tones at the higher frequencies. A 2 PNdB reduction in CRP noise was observed at cutback. Since the lower interaction tones generally govern the spectra at the low-speed operating conditions, this reduction was considered to adequately represent the cutback effect in the current full-wheel unsteady CFD based investigation.

In addition, compared to the $M = 0.25$ condition, the capture streamtube contraction is increased at lower takeoff speeds. Increased streamtube contraction affects

the path along which the front-rotor tip-vortices are convected. The surface pressure results are thereby changed compared to the $M = 0.25$ condition which in turn influences the noise levels. This effect at lower takeoff speeds is not taken into account in the current analysis.

Pylon and angle-of-attack effects are not included in the CFD analysis and any aerodynamic interaction of non-uniform inflow with the CRP rotors is not captured. The presence of an upstream pylon or angle-of-attack effects lead to unsteady blade loading at the BPF harmonics which in turn influences the rotor-alone tone noise as described in Chapter 4.5. As a result, the rotor-alone tones are underestimated in the present analysis. However, the interaction tones generally dominate the CRP noise spectra at the low-speed conditions [13]. Thus underestimating rotor-alone noise is not believed to significantly affect overall CRP noise levels.

CFD simulations and CRP noise calculations were performed for the model scale baseline and advanced design CRPs. The full-scale noise results are obtained by acoustically scaling the model scale noise spectra. The sound pressure level is obtained from

$$SPL_{FS} = SPL_{MS} + 20log(SF), \tag{6.1}$$

where the subscripts FS and MS denote full and model scale data, respectively. The scaling factor is given by $SF = D_{MS}/D_{FS} = 6.82$. The frequencies of the full scale noise spectrum are shifted according to

$$f_{FS} = f_{MS}/SF. \tag{6.2}$$

Due to CPU time and memory capacity limitations, the model scale CRP tones were determined up to the 22th harmonic order only, i.e. up to a maximum frequency of $f_{max,MS} = 22 \cdot BPF_1 = 24.44$ kHz such that the maximum full scale frequency included in the CRP noise estimation is $f_{max,FS} = 3.58$ kHz. Consequently, the frequency range most strongly weighted in the conversion to perceived noisiness is captured in the calculations.

The above assumptions and related limitations should be kept in mind in the

discussion of the noise results. However, the noise estimation is performed on a consistent basis and the trends observed in the results can be used to assess the potential noise reduction of CRP designs and related source noise mitigation concepts. The noise results at the FAR 36 flyover and sideline observer locations are discussed next.

6.3 Flyover Noise Assessment

Tone-corrected perceived noise levels are plotted over time at the flyover receiver from the start of the takeoff roll in Figure 6-2. The PNLT source breakdown of the datum turbofan powered aircraft presented on the top shows that the total noise is largely governed by fan noise. In addition, airframe noise contributes significantly to the overall noise in a short period after the thrust setting is cut back to 70 % of the maximum thrust at 610 m.

In addition to operating at lower tip Mach numbers after cutback, the fan noise is decreased further and subsequently increased sharply at about 95 s which corresponds to the aircraft being located directly above the flyover observer location. This effect is attributed to the shape of the fan noise directivity since fan noise is somewhat shielded by the nacelle when the aircraft is directly above the observer location.

The flyover noise levels of the baseline CRP powered aircraft configuration are displayed in Figure 6-2b. The overall noise level is dominated by the CRP sources. The takeoff trajectory and the flap and slat settings are similar compared to the datum turbofan aircraft configuration (see Figure 6-1) such that the airframe noise is not significantly changed. The CRP engine core is smaller than the datum turbofan core, thus LPC, combustor, and LPT noise are reduced. Since the jet noise method is not applicable to the CRP engine as described in Section 2.4, the jet noise source is not included in the CRP noise assessment. However, jet noise is not believed to significantly increase the total noise level due to the low nozzle exit velocities (around $M = 0.1$).

After the maximum noise levels are reached near the location at which the aircraft

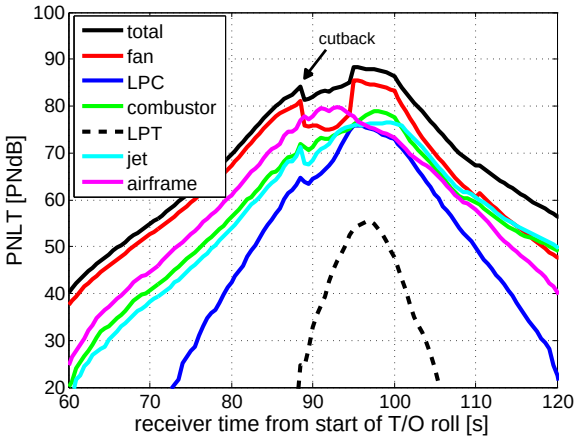

(a) Datum Turbofan

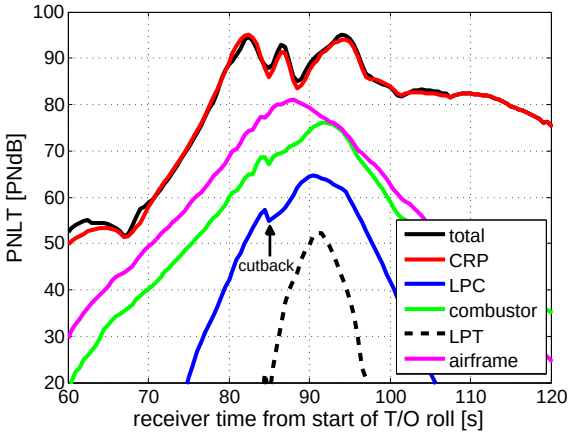

(b) Baseline CRP

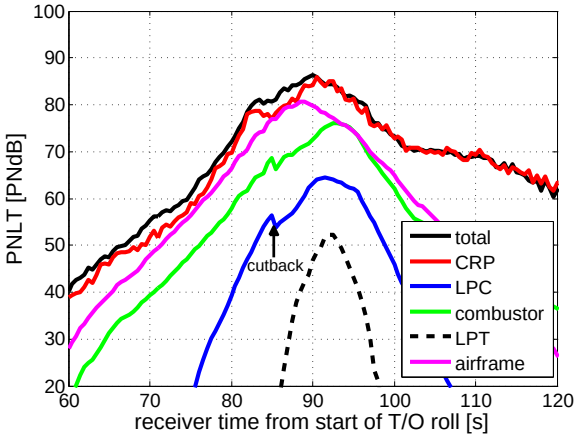

(c) Advanced Design CRP

Figure 6-2: Tone-Corrected Perceived Noise Level at FAR 36 flyover receiver location

passes the flyover axial position (at 95 s and $h = 1,850$ ft), the rate of the decrease in CRP noise (0.7 PNdB/s on average) is significantly lower than the fan noise decrease (1.2 PNdB/s on average). In contrast to a turbofan powered aircraft, the noise from a CRP aircraft configuration will thus be perceived over longer time periods. This effect is attributed to the differences in fan and CRP directivities. The shroud around the fan causes the generated noise to decrease more rapidly once the aircraft has passed the observer location.

As illustrated in Figure 6-2c, implementing source mitigation concepts resulted in a substantial reduction in CRP noise along the entire trajectory relative to the baseline CRP. The maximum perceived noise level was reduced by approximately 9 PNdB by minimizing the influence of the front-rotor tip-vortex interaction with the rear rotor and reducing the strength of the wake and upstream influence interference effects. The small local variations in CRP noise are attributed to the interference effects caused by operating the rotors at unequal tip speeds. The engine core is the same as in the baseline CRP case and the distributions of LPC, combustor, and LPT noise do not change.

The CRP is still the dominating noise source but the overall noise signature is now similar to the datum turbofan powered noise levels. This indicates that CRPs can achieve acoustic performance levels of advanced turbofan powered aircraft by addressing the strength of CRP tip-vortex, wake, and upstream influence interaction effects.

The above observations are summarized in the effective perceived noise levels provided in Figure 6-3. CRP noise is clearly the dominant noise source in the baseline CRP configuration but by implementing noise reduction technologies, the CRP noise was reduced by 10.2 EPNdB. Since the noise from the remaining engine sources is significantly decreased due to the reduction in core size, the total noise generated by the advanced design CRP was reduced relative the the datum turbofan configuration.

The total EPNL values are tabulated in Table 6.2. Relative to the datum turbofan aircraft configuration, the total noise of the baseline CRP aircraft arrangement was 6.6 EPNdB higher. In the case of the advanced design CRP, implementing noise

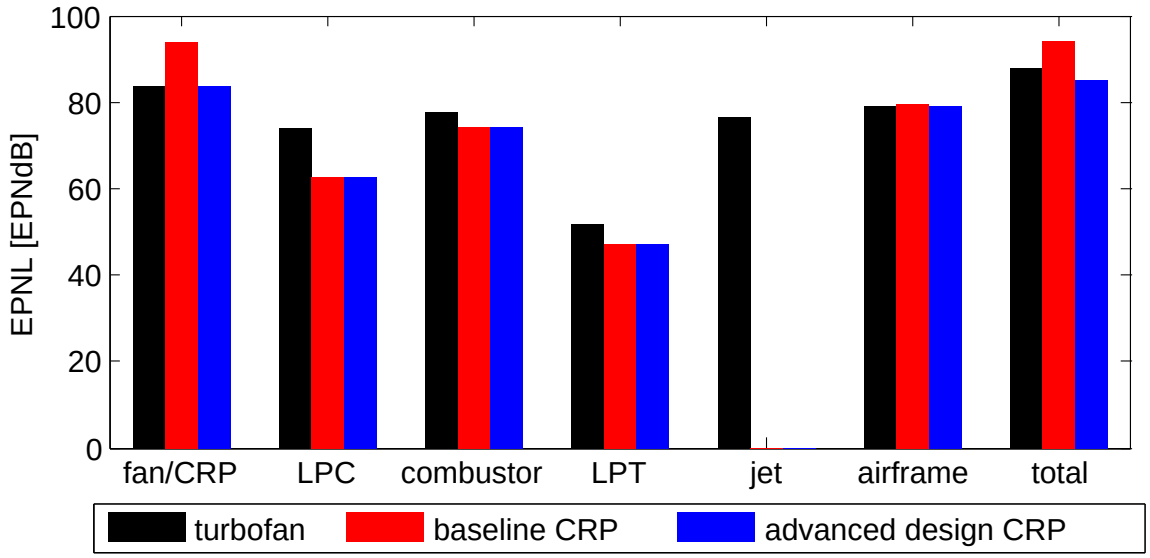

Figure 6-3: EPNL breakdown at FAR 36 flyover receiver location

reduction technologies led to a significant reduction in total noise (−9.2 EPNdB).

Table 6.2: Total EPNL in EPNdB at FAR 36 flyover location

	Datum Turbofan Aircraft	Baseline CRP Aircraft	Advanced Design CRP Aircraft
Estimated	87.6	94.2	85.0
Stage 4	91.2	91.5	91.5

In addition to the computed noise levels, the stage 4 noise limits are provided in Table 6.2. The limits are slightly higher for the CRP aircraft arrangements due to their increased takeoff weights. Overall, the results suggest that the baseline CRP powered aircraft does not reach the stage 4 noise limits by a considerable margin (2.7 EPNdB). On the other hand, the advanced design CRP was found to meet the stage 4 noise restriction with a margin of 6.5 EPNdB at the flyover observer location.

6.4 Sideline Noise Assessment

Fan and jet noise govern the noise signature of the datum turbofan powered aircraft as illustrated in Figure 6-4a. The aircraft passes the axial location of the sideline

Table 6.3: Total EPNL in EPNdB at FAR 36 sideline location

	Datum Turbofan Aircraft	Baseline CRP Aircraft	Advanced Design CRP Aircraft
Estimated	89.7	94.1	85.5
Stage 4	96.6	96.8	96.8

observer at about 69 s and the fan noise increases significantly as the shielding by the nacelle is reduced.

With a relatively small rotor-rotor spacing and unclipped rear rotor, the maximum total noise level of the baseline CRP aircraft configuration increased by 6.5 PNdB relative to the turbofan powered aircraft as displayed in Figure 6-4b. Regarding acoustic performance, the baseline CRP powered aircraft is not competitive compared with advanced turbofan aircraft arrangements.

As illustrated in Figure 6-4c, increasing the rotor-rotor spacing and clipping the rear rotor led to noise reductions of up to 15 PNdB along the entire trajectory. The results indicate that the combination of reducing the strength of the potential field and viscous wake interactions and minimizing the tip-vortex interactions is a suitable and effective approach to achieve significant noise reductions in CRP noise.

The above observations are again summarized in the EPNL breakdown provided in Figure 6-5. The observed trends are similar to those at the flyover observer location. Effectively implementing source mitigation technologies led to a reduction of 10.2 EPNdB and indicated the acoustic competitiveness of advanced CRP configurations relative to high bypass ratio, low fan pressure ratio turbofans.

The acoustics benefits of the advanced CRP design are combined with a smaller engine compared to the datum turbofan engine. At the sideline observer location, this led to total noise level reduction of 4.2 EPNdB as tabulated in Table 6.3. The results suggest that Stage 4 noise limits are met by all three configurations investigated. The margin is smallest for the baseline CRP aircraft (2.7 EPNdB) and largest for the advanced design CRP (11.3 EPNdB).

It is important to note the following assumptions used in the above analysis: the

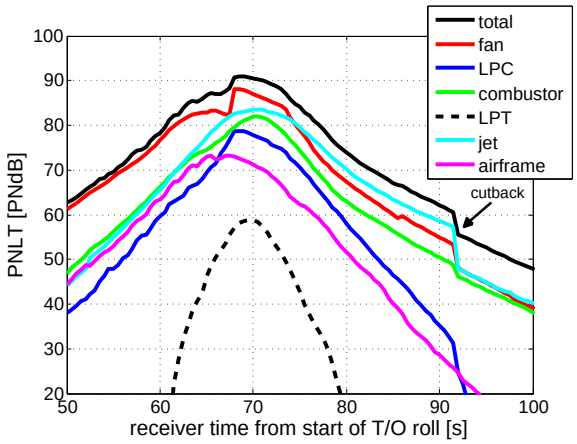

(a) Datum Turbofan

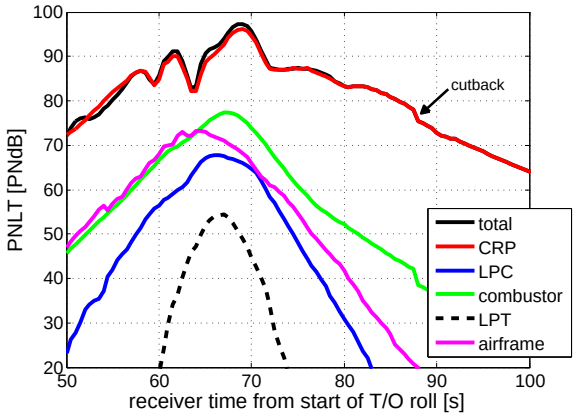

(b) Baseline CRP

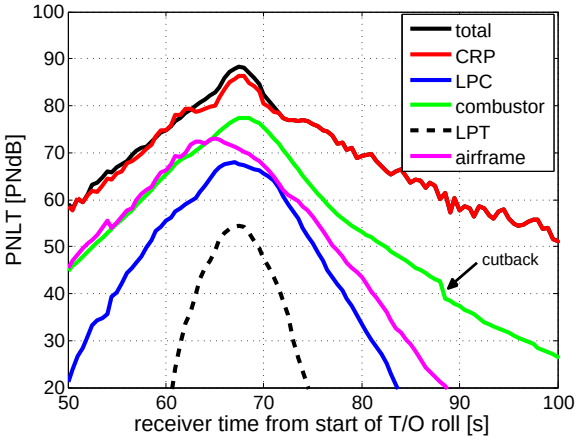

(c) Advanced Design CRP

Figure 6-4: Tone-Corrected Perceived Noise Level at FAR 36 sideline receiver location

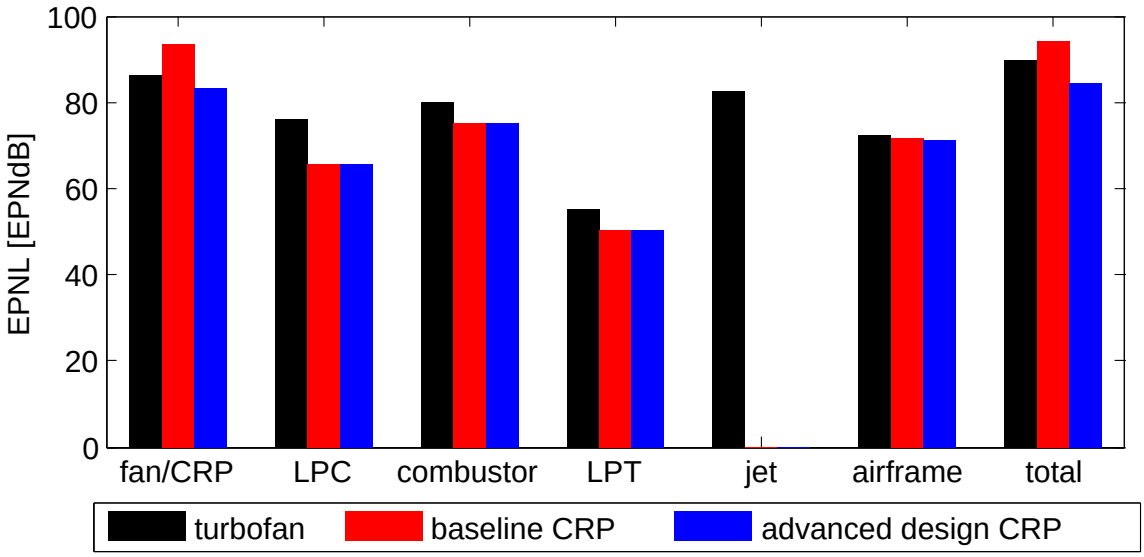

Figure 6-5: EPNL breakdown at FAR 36 sideline receiver location

fan noise estimation method might not be applicable to advanced fan designs thereby overestimating the generated noise levels. Pylon and angle-of-attack effects are not included in the CRP noise estimation which leads to an underestimation of the rotor-alone tones.

In summary, minimizing the tip-vortex interaction and decreasing the strength of potential field and viscous wake interactions by reducing the rear-rotor diameter, increasing the rotor-rotor spacing demonstrated noise reductions of up to 15 PNdB, resulting in an acoustic benefit of around 10 EPNdB at both flyover and sideline observer locations. Given the above assumptions, these benefits indicate that the advanced design CRP can meet Stage 4 noise restrictions. The advanced CRP is the result of a first design iteration with the objective to reduce noise. A second design iteration is needed to assess cruise performance and fuel burn levels.

Chapter 7

Summary and Conclusions

The noise assessment of counter-rotating propfan (CRP) configurations was presented in this thesis to evaluate what levels of acoustic performance can be achieved with advanced CRP designs. The main results of the work are summarized below.

7.1 Summary

Given a $3,500$ nm mission at cruise Mach number 0.78, a baseline aircraft seating 150 passengers was developed featuring an advanced turbofan design with a bypass ratio of 8.9 and a fan pressure ratio of 1.49. Guided by data available in the literature, a baseline CRP configuration was defined next. The CRP noise mechanisms were dissected and quantified and it was determined that substantial noise reductions could only be achieved by implementing source mitigation concepts targeting all of the noise source mechanisms.

The baseline CRP was subsequently re-designed for reduced noise. The rotor-rotor axial spacing was increased by 56 % and the rear rotor was clipped at 75 % span. The front-rotor tip-vortex interaction with the rear rotor was consequently minized and the strength of rear-rotor upstream influence and front-rotor viscous wake interaction effects was decreased. Based on a vortex-lattice analysis, the thrust level was maintained by increasing the rear rotor blade count and allowing differential tip speeds. Relative to the baseline CRP, the acoustic assessment of the advanced

design CRP demonstrated reductions of 20 dB in maximum noise levels in the front and aft polar arcs at interaction tone frequencies previously governed by tip-vortex effects. Maximum noise levels at interaction tone frequencies previously dominated by upstream influence were reduced by up to 15 dB. Reductions of 11 dB in mean SPL over the front and aft arcs were determined for the first three interaction tones.

For equal tip speeds, the interaction tone levels approach zero at low and high polar angles which is believed to be due to substantial destructive interference effects, which reduce the noise levels close to the axis of rotation. For unequal tip speeds, the acoustic power is spread over the entire polar angle range and at the higher interaction tone frequencies, this effect actually resulted in increased mean sound pressure levels. For the first six interaction tones, the acoustic assessment of the advanced design CRP demonstrated an average noise reduction of 7.25 dB in mean SPL.

Based on the datum turbofan powered airframe and the same mission, baseline and advanced design CRP aircraft arrangements were defined in aft fuselage pylon mounted pusher configuration. Modifications to the fuselage structure and the mounting structure resulted in a $5,000$ lb increase in the MTOW relative to the turbofan aircraft configuration. On the aircraft/engine system level, the acoustic performance of the three aircraft configurations was investigated in detail. The changes relative to the datum turbofan powered aircraft are quantified in Table 7.1 for the FAR 36 flyover and sideline observer locations. The baseline CRP was not found to be a suitable alternative to the datum turbofan aircraft as the total noise was increased by 5.5 EPNdB averaged over the two noise certification conditions investigated.

Table 7.1: Change in total EPNL in EPNdB relative to datum turbofan powered aircraft

	Baseline CRP Aircraft	Advanced Design CRP Aircraft
Flyover	+6.6	−2.6
Sideline	+4.4	−4.2

The noise assessment for the advanced design CRP indicated an average reduc-

tion of 3.4 EPNdB relative to the datum turbofan aircraft. Increasing the rotor-rotor spacing and reducing the rear-rotor diameter are demonstrated to be promising approaches towards the design of advanced CRPs for reduced noise. A detailed cruise performance analysis of the advanced CRP is required in the future in order to ensure the fuel burn competitiveness relative to advanced turbofans. In general, the results suggest that Stage 4 noise limits can be met with advanced CRP designs provided that tip-vortex, upstream influence, and viscous wake noise source mechanisms are targeted by effectively implementing CRP noise reduction technologies.

7.2 Key Contributions

A multidisciplinary integrated acoustic and aerodynamic assessment capability was established in order to investigate the fuel burn performance and noise challenges associated with advanced propfan propulsion configurations on an aircraft/engine system level. A key piece in the development of the methodology was to implement a method to estimate CRP noise. To this end, a frequency domain approach based on on the acoustic analogy and the extension of Hanson's single rotor noise method [6] to counter-rotating propfans was introduced and carefully validated. The CRP noise estimation approach was coupled with high-fidelity full-wheel 3-D unsteady RANS simulations to capture the underlying aerodynamic mechanisms responsible for CRP interaction noise and to determine the time-varying blade surface pressures necessary to define the acoustic source terms. The established method allows for parametric studies and is capable of exploring noise reduction technologies.

Quantifying the relative importance of the CRP noise source mechanisms for the baseline CRP demonstrated that all noise source mechanisms need to targeted in order to achieve significant noise reductions. Minimizing the tip-vortex interaction and reducing wake and upstream influence effects by increasing the axial spacing between the rotors and decreasing the rear-rotor diameter yielded noise reductions of 9.2 EPNdB and 8.6 EPNdB relative to the baseline CRP aircraft configuration at the flyover and sideline observer locations, respectively. The acoustic assessment of

the advanced design CRP indicates that Stage 4 noise limits are met with a margin of 8.9 EPNdB averaged over the flyover and sideline noise certification conditions.

7.3 Future Work

Further validation of the CRP noise estimation method should be conducted including unequal tip speed conditions and simulations accounting for the presence of an upstream pylon. In addition, the following recommendations for future work can be made:

- Noise results for the CRP powered aircraft configurations should be obtained at the approach condition using the CRP noise method in order to evaluate whether the approach noise results agree with the trends observed at the FAR 36 flyover and sideline conditions.

- The unsteady blade surface pressures should be determined at additional operating conditions along the takeoff trajectory to quantify the influence of increased streamtube contraction on CRP interaction tone noise at speeds lower than $M = 0.25$.

- The impact of non-uniform inflow on the CRP noise levels should be assessed. The magnitude of the influence of angle-of-attack or upstream pylon effects on CRP noise at the low-speed conditions during takeoff and approach should be quantified.

- In the light of higher relative tip Mach numbers at cruise conditions, the influence of quadrupole noise source could be assessed and the competitiveness of CRP designs regarding in-flight cabin noise should be evaluated.

- The aerodynamic performance of the CRP configurations should be assessed at the cruise condition. The trade-offs between fuel burn and acoustic performance should be further investigated and quantified.

Appendix A

Baseline Airframe Definition

Table A.1: Baseline airframe definition - wing and fuselage (in ft)

Wing		Fuselage	
Planform area	1350.17	Length (overall)	127.10
Exposed area	1072.28	Width (maximum)	13.00
Trapezoid area	1169.67	Height (maximum)	14.00
Wimpress area	1270.08		
Exp. trap. root chord	14.58	Nose length	16.49
Sweep (outbd. qtr. chord)	24.00	Upsweep length	39.82
Thickness/chord (avg.)	0.095	Upsweep height	14.63
Taper ratio (exp. trap)	0.337	Tail length	31.33
Taper ratio (exposed)	0.247	Tail closure width	1.429
Taper ratio (planform)	0.214	Tail closure height	1.429
Dist. from nose...		Tail-bulkhd. length	23.01
L.E./body junction	49.23	Main cabin length	90.00
wing/body aero. ctr.	59.83	Tot. cab. floor area	1086.86
Approx. overall C.G.	61.82	Tot. cab. lining area	2135.55
		Unavail. belly length	79.71
Geometric span	112.70	Belly x-sect. area	36.18
Exposed span	99.70	Avail. belly volume	1714.20
Structural span	121.13	Belly vol. efficiency	0.788
Aspect ratio	10.00		
Outbd. fuel vol. (gallons)	4260.5		
Total. fuel vol. (gallons)	6144.0		

Table A.2: Baseline airframe definition - horizontal and vertical tail (in ft)

Horizontal Tail		Vertical Tail	
Horiz. tail area	350.00	Vert. tail area	275.00
Aspect ratio	4.50	Aspect ratio	1.80
Sweep (qtr. chord)	30.00	Sweep (qtr. chord)	35.00
Span	39.69	Height	21.78
Taper ratio	0.250	Taper ratio	0.300
Centerline chord	14.11	Root chord (CXV)	19.02
Dist. from nose...		Dist. from nose...	
L.E. root junct.	105.47	L.E. root junct.	97.80
T.E. root junct.	119.58	T.E. root junct.	117.33
T.E. tip	123.10	T.E. tip	122.81
Aero. center	113.58	Aero. center	112.14

Appendix B

CRP Noise Code User Manual

The CRP noise estimation method described in Chapter 4 was implemented in a Matlab code denoted CRPNEC. This appendix outlines the Matlab code to calculate the noise spectrum of a CRP configuration at specified frequencies and observer locations.

B.1 File Structure

The CRP noise estimation code consists of of five run scripts calling three functions. An overview of the code structure is displayed in Figure B-1. The tasks performed in each of the run scripts and functions are described in detail next.

`CRPNEC_main.m` is the run script calling the functions to compute the acoustic source terms from the geometry and and unsteady blade surface pressure data. In the first part of the script, the input parameters for the CRP configuration (blade count, diameter, rotor-rotor axial spacing), the flight and operating conditions (ambient pressure and temperature, flight Mach number, and tip speeds) are defined. In order to compute the acoustic source terms, the radial and chordwise grid point counts of the mesh used in the CFD calculations are required. Finally, the observer location needs to be specified in spherical coordinates relative to the CRP position.

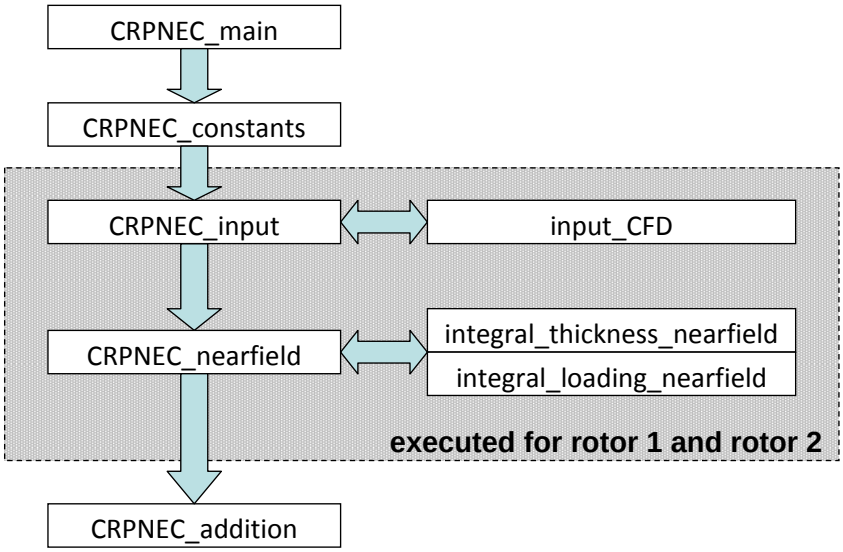

Figure B-1: Overview of CRP noise code structure

In the output control, the number of BPF harmonics to be computed is defined. Based on the user input, the contributions of thickness and loading noise can be calculated separately. In addition to providing noise results for the total CRP, options are available to plot narrowband spectra and acoustic pressure time signals for the contributions of either front or rear rotor only.

In order to dissect the mechanisms responsible for CRP interaction noise, the loading noise is computed based on the source terms on a limited spanwise range. For example, in order to quantify the relative importance of the front-rotor wake interaction at the interaction tone frequency under consideration, the loading source is computed between 12.5 % and 75 % on the rear rotor only. The spanwise range to be accounted for in the loading noise computation is defined in the output control.

`CRPNEC_constants.m` is a run file used to non-dimensionalize the specified input parameters. In addition, the frequencies of the CRP rotor-alone and interaction tones are determined based on the inputs for blade count and tip speed.

`CRPNEC_input.m` is a function called by `CRPNEC_main.m` sequentially for the front and rear rotor. It accepts as inputs the information on flight and operating

condition, and the data of CFD grid used to determine the time-dependent blade surface pressures. Based on the rotor geometry and unsteady loading data, it determines the source coordinates and the thickness and loading source terms.

`input_CFD.m` is a run file used to load the unsteady blade surface pressures. First, the blade geometry and steady surface pressure information is read from external data files in the subfolder `full-wheel-loading` for the pressure and suction sides, respectively. The data files contain the coordinates (in m) and the steady pressures as $(p - p_0) \,/\, (p_{t,0} - p_0)$ for every grid point at constant radial sections in chordwise direction from trailing edge to leading edge for the pressure side and from leading edge to trailing edge for the suction side.

Similarly, the loading harmonics are read next from external data files listing the coordinates and complex pressure harmonics for every grid point at constant radial sections in chordwise direction. It should be noted that the loading harmonics are required for each blade since they may differ from blade to blade due to unequal tip speed or non-uniform inflow effects. The number of loading harmonics considered in the determination of the acoustic source terms is defined in `CRPNEC_main.m`.

`CRPNEC_nearfield.m` is a run file used to compute the thickness and loading noise sound pressure levels at the CRP rotor-alone and interaction tone frequencies for each rotor. The working equations implemented in the code are described in Section 4.2. In addition, the thickness and loading acoustic pressure signals are determined from the sound pressure level results.

`integral_thickness_nearfield.m` is a function called by `CRPNEC_nearfield.m` for the computation of the thickness noise integral from Equation 4.10. It accepts the thickness source terms and the observer coordinates and outputs the solution of the thickness integral for each grid point μ, ν.

`integral_loading_nearfield.m` is a function called by `CRPNEC_nearfield.m` for the

computation of the loading noise integral from Equation 4.12. It accepts the loading source terms and the observer coordinates and outputs the solution of the loading integral for each grid point μ, ν.

`CRPNEC_addition.m` is a run file used to superpose the noise fields from front and rear rotor. It outputs and plots the total CRP noise in terms of narrowband spectra and acoustic pressure signals. In addition, the front- and rear-rotor contributions to the total CRP noise are dissected and quantified and the CRP blade geometries are plotted.

Hanson's notation is used for the variable names and references are made to the equations presented in [6] wherever possible. The modifications required to extend Hanson's single rotor noise method to CRP configurations are clearly labeled in the code.

Bibliography

[1] CFM International, "CFM56-7B Turbofan Engine Overview," http://www.cfm56.com.

[2] T. Hannigan and H. Wainauski, "Wind Tunnel Results of Counter Rotation Prop-Fans Designed With Lifting Line and Euler Code Methods," in *AIAA/SAE/ASME/ASEE 27th Joint Propulsion Conference*. AIAA 1991-2499, June 1991.

[3] R. Hager and D. Vrabel, "Advanced Turboprop Project," NASA SP-495, Tech. Rep., 1988.

[4] W. Strack, G. Knip, A. Weisbrich, J. Godston, and E. Bradley, "Technology and Benefits of Aircraft Counter Rotation Propellers," NASA TM-82983, Tech. Rep., 1982.

[5] J. Groeneweg and L. Bober, "NASA Advanced Propeller Research," NASA TM-101361, Tech. Rep., 1988.

[6] D. B. Hanson and D. J. Parzych, "Theory for Noise of Propellers in Angular Inflow with Parametric Studies and Experimental Verification," NASA CR-4499, Tech. Rep., 1993.

[7] F. Metzger, "A Review of Propeller Noise Prediction Methodology: 1919-1994," NASA CR-198156, Tech. Rep., 1995.

[8] D. Hanson, "Compressible Helicoidal Surface Theory for Propeller Aerodynamics and Noise," *AIAA Journal*, vol. 21, pp. 881–889, 1983.

[9] D. Hanson, "Noise of Counter-Rotation Propellers," *J. Aircraft*, vol. 22, no. 7, pp. 609–617, 1985.

[10] A. Zachariadis and C. Hall, "Application of a Navier-Stokes Solver to the Study of Open Rotor Aerodynamics," in *Proceedings of ASME Turbo Expo 2009*. GT2009-59332, June 2009.

[11] C. Polacsek and R. Barrier, "Numerical Simulation of Counter-Rotating Fan Aeroacoustics," in *13th AIAA/CEAS Aeroacoustics Conference*. AIAA 2007-3680, May 2007.

[12] A. Stuermer and J. Yin, "Low-speed Aerodynamics and Aeroacoustics of CROR Propulsion Systems," in *15th AIAA/CEAS Aeroacoustics Conference*. AIAA 2009-3134, May 2009.

[13] B. Magliozzi, D. Hanson, and R. Amiet, "Propeller and Propfan Noise," in *Aeroacoustics of Flight Vehicles: Theory and Practice. Volume 1: Noise Sources*. NASA, Langley Research Center, 1991, pp. 1–64.

[14] R. Majjigi, K. Uenishi, and P. Gliebe, "An Investigation of Counterrotating Tip Vortex Interaction," NASA CR-185135, Tech. Rep., 1989.

[15] B. Janardan and P. Gliebe, "Acoustic Power Level Comparisons of Model-Scale Counterrotating Unducted Fans," in *29th Aerospace Sciences Meeting*. AIAA 1991-0595, January 1991.

[16] R. Woodward and C. Hughes, "Aeroacoustic Effects of Reduced Aft Tip Speed at Constant Thrust for a Model Counterrotation Turboprop at Takeoff Conditions," in *AlAA 13th Aeroacoustics Conference*. AIAA 1990-3933, October 1990.

[17] R. Woodward and E. Gordon, "Noise of a Model Counterrotation Propeller with Reduced Aft Rotor Diameter at Simulated Takeoff/Approach Conditions (F7/A3)," in *AlAA 26th Aerospace Sciences Meeting*. AIAA 1988-0263, January 1988.

[18] J. Brookfield and I. Waitz, "Trailing-Edge Blowing for Reduction of Turbomachinery Fan Noise," *J. Prop. Power*, vol. 16, no. 1, pp. 57–64, 2000.

[19] R. Woodward, E. Fite, and G. Podboy, "Noise Benefits of Rotor Trailing Edge Blowing for a Model Turbofan," in *45th Aerospace Sciences Meeting and Exhibit*. AIAA 2007-1241, January 2007.

[20] Federal Aviation Administration, "Federal Aviation Regulations Part 36 - Noise Standards: Aircraft Type and Airworthiness Certification," August 2002.

[21] Federal Aviation Administration, "Federal Aviation Regulations Part 25 - Airworthiness Standards: Transport Category Airplanes," August 2002.

[22] L. McCullers, "Aircraft Configuration Optimization Including Optimized Flight Profiles," in *Recent Experiences in Multidisciplinary Analysis and Optimization, Part 1*. NASA, Langley Research Center, 1984.

[23] R. Feagin and W. Morrison, "Delta Method, An Empirical Drag Buildup Technique," NASA CR-151971, Tech. Rep., 1978.

[24] J. Kurzke, *GasTurb 11 User Manual*, 2007.

[25] M. Drela, *RVL (Rotor Vortex Lattice) and RAXAN (Rotor Axisymmetric Analysis) User Manuals*, Massachusetts Institute of Technology, 2007.

[26] Numeca International, *FINE/Turbo User Manual Version 8.2*, Brussels, Belgium, 2009.

[27] A. March, "Influence of Low-Speed Aerodynamic Performance on Airport Community Noise," Master's thesis, Massachusetts Institute of Technology, 2008.

[28] M. Fink, "Airframe Noise Prediction," FAA-RD 77-29, Tech. Rep., 1977.

[29] M. Fink, "Aircraft Noise Prediction Program. Theoretical Manual," NASA TM-83199 Part 2, Tech. Rep., 1982.

[30] ESDU, "Airframe Noise Prediction," Item No. 90023, Tech. Rep., 1990.

[31] ESDU, "Prediction of Noise Generated by Fans and Compressors in Turbojet and Turbofan Engines," Item No. 98008, Tech. Rep., 1998.

[32] M. Heidmann, "Interim Prediction Method for Fan and Compressor Source Noise," NASA TM X-71763, Tech. Rep., 1975.

[33] D. Dunn and N. Peart, "Aircraft Noise Source and Contour Estimation," NASA CR-114649, Tech. Rep., 1973.

[34] ESDU, "Prediction of Combustor Noise From Gas Turbine Engines," Item No. 05001, Tech. Rep., 2005.

[35] Society of Automotive Engineers, "Gas Turbine Jet Exhaust Noise Prediction," ARP 876, Revision D, Tech. Rep., 1994.

[36] E. Krejsa and M. Valerino, "Interim Prediction Method for Turbine Noise," NASA TM X-73566, Tech. Rep., 1976.

[37] K. Kontos, R. Kraft, and P. Gliebe, "Improved NASA-ANOPP Noise Prediction Computer Code for Advanced Subsonic Propulsion Systems. Volume 2: Fan Suppression Model Development," NASA CR-202309, Tech. Rep., 1996.

[38] J. Stone, E. Krejsa, and B. Clark, "Jet Noise Modeling for Coannular Nozzles Including the Effects of Chevrons ," NASA CR-212522, Tech. Rep., 2003.

[39] ESDU, "Evaluation of the Attenuation of Sound by a Uniform Atmosphere," Item No. 78002, Tech. Rep., 1977.

[40] ESDU, "The Correction of Measured Noise Spectra for the Effects of Ground Reflection," Item No. 94035, Tech. Rep., 1994.

[41] ESDU, "Estimation of Lateral Attenuation of Air-to-Ground Jet or Turbofan Aircraft Noise in One-Third Octave Bands," Item No. 82027, Tech. Rep., 1982.

[42] J. Roskam, "Component Weight Estimation," in *Airplane Design*, 1989.

[43] J. Kerrebrock, *Aircraft Engines and Gas Turbines*, 2nd ed. The MIT Press, 1992.

[44] ESDU, "An Introduction to Aircraft Noise," Item No. 02020, Tech. Rep., 2002.

[45] I. Goldsmith, "A Study to Define the Research and Technology Requirements for Advanced Turbo/Propfan Transport Aircraft," NASA CR-166138, Tech. Rep., 1981.

[46] ESDU, "Noise Transmission into Aircraft Cabins," Item No. 07001, Tech. Rep., 2007.

[47] D. Chapman, R. Fleury, and D. Smith, "Testing of the 578-DX Propfan Propulsion System," in *AIAA/SAE/ASME/ASEE 25th Joint Propulsion Conference*. AIAA 1989-2581, July 1989.

[48] F. Farassat, "Acoustic Analysis of Propfan," NASA CR-162312, Tech. Rep., 1979.

[49] M. Goldstein, "Unified Approach to Aerodynamic Sound Generation in the Presence of Solid Boundaries," *J. Acoustic Soc. Am.*, vol. 56, pp. 497–509, 1974.

[50] D. Hanson and M. Fink, "The Importance of Quadrupole Sources in Prediction of Transonic Tip Speed Propeller Noise," *J. Sound Vibrat.*, vol. 62, no. 1, pp. 19–38, 1979.

[51] W. Briggs, V. Henson, and S. McCormick, "A Multigrid Tutorial," SIAM, 2000.

[52] V. Kouznetsov, V. Ganabov, K. L., and S. Makashov, "Acoustic Characteristics of Propfans," in *15th AIAA Aeroacoustics Conference*. AIAA 1993-4444, October 1993.

[53] R. Woodward and I. Loeffler, "Inflight Source Noise of an Advanced Full-Scale Single Rotation Propeller," in *29th Aerospace Sciences Meeting*. AIAA 1991-0594, January 1991.

[54] R. Woodward, "Noise of Simulated Installed Model Counterrotation Propeller at Angle-of-Attack and Takeoff/Approach Conditions," in *AlAA 28th Aerospance Sciences Meeting*. AIAA 1990-0283, January 1990.